

Impact of Intertidal Habitats on Hydrodynamics in Tidally Energetic, Well-Mixed Estuaries

RENJIE ZHU^{a,b,c,d}, WEI ZHANG^{a,b,c}, AND XIAOYAN WEI^d

^a Key Laboratory of Ministry of Education for Coastal Disaster and Protection, Hohai University, Nanjing, China

^b State Key Laboratory of Water Disaster Prevention, Hohai University, Nanjing, China

^c College of Harbour, Coastal and Offshore Engineering, Hohai University, Nanjing, China

^d National Oceanography Centre, Liverpool, United Kingdom

(Manuscript received 23 August 2023, in final form 18 February 2025, accepted 28 April 2025)

ABSTRACT: Estuarine intertidal habitats, which strongly affect the functioning of estuarine ecosystems, have rapidly diminished worldwide due to human activities and climate change. However, the mechanisms by which intertidal habitats modulate estuarine hydrodynamics remain poorly understood. A three-dimensional semianalytical model is developed to systematically investigate the interactions between intertidal and channel waters in tidally dominated, well-mixed estuaries. By considering simplified bathymetry, geometry, and forcing conditions, the model dynamically couples intertidal and channel water motions using a perturbation method that allows for an explicit dissection of different controlling physical processes. Our findings reveal that intertidal habitats amplify semidiurnal tidal motions, causing significantly enhanced residual and quarter-diurnal tidal currents due to advection (AC). The strengthened AC shifts the pattern and magnitude of the total residual circulation. Lateral water exchange between intertidal and channel regions generates a new residual and quarter-diurnal tidal contribution (TF), which dampens quarter-diurnal tidal currents in the deep channel. The TF and enhanced AC due to intertidal habitats increase ebb dominance in the deep channel. Our sensitivity analysis shows that halving the intertidal width halves the water exchange and the abovementioned intertidal effects on the residual and tidal currents, and the upper-estuary habitats induce broader changes in the channel hydrodynamics than the lower-estuary habitats. We also found that increasing estuary length/convergence strongly affects the intertidal effects. These findings highlight the importance of understanding interactions between intertidal and channel waters to evaluate the risks of intertidal habitat loss for estuarine functioning and the potential benefits of intertidal habitat restoration/creation in mitigating estuarine hazards.

KEYWORDS: Estuaries; Barotropic flows; Tides; Idealized models


1. Introduction

Intertidal habitats, such as sandflats, mudflats, salt marshes, and mangroves, are ecosystems commonly located in estuaries. These habitats undergo regular cycles of exposure during low tide and submersion during high tide, providing vital breeding and nursing grounds for economically and ecologically important marine life (Bom et al. 2020). They also play a key role in enhancing water quality through pollutant and excess nutrient filtration (Teuchies et al. 2013), regulating climate change through carbon capture and storage (Lee et al. 2021), and protecting life and properties against flooding and erosion hazards by dissipating wave energy (Möller et al. 2014; Orton et al. 2015).

Due to flood defenses and coastal development in the past few decades, however, intertidal habitats have been lost worldwide at rapid rates. Globally, the areas of intertidal habitats have shrunk by 16% between 1984 and 2016 (Murray et al. 2019). In China, approximately 59% of coastal salt marshes were lost from the 1980s to the 2010s mainly due to intensive land reclamation

in the Yangtze River and Pearl River deltas (Gu et al. 2018; Ma et al. 2019). In southeast England, a ~20% overall loss of salt marshes occurred during 1973–88 as a result of intertidal reclamation and coastal erosion around the Thames Estuary (Doody 2004). In the United States, over 80% of coastal wetlands have been lost due to agricultural use (Zedler 2004).

The intertidal habitat loss poses significant concerns for the long-term ecological, economic, and societal functioning of estuarine ecosystems particularly in the face of climate change (Crooks et al. 2018). For example, sequential reclamations in many estuaries have resulted in the steepening and narrowing of intertidal habitats (Guo et al. 2022; Wang et al. 2012), which can significantly alter estuarine water motion, material transport, and overall estuarine functioning (Koch et al. 1992). On the other hand, the increasing flooding, erosion, and biodiversity risks posed by climate change (e.g., sea level rise, extreme weather) and human activities (e.g., damming, dredging, and reclamation) have prompted worldwide nature-based solutions such as intertidal habitat restoration and creation (Moraes et al. 2022). However, the efficacy of these solutions strongly depends on the responses of estuarine dynamics to intertidal habitat changes, which can vary significantly from estuary to estuary (Talke and Jay 2020). In Darwin Harbor, Xiangshan Bay, and Newport Bay, intertidal habitat losses resulted in dampened semidiurnal tides, enhanced flood dominance, and a significantly increased up-estuary sediment transport (Guo et al. 2018;

 Denotes content that is immediately available upon publication as open access.

Corresponding author: Xiaoyan Wei, xwei@noc.ac.uk

DOI: 10.1175/JPO-D-23-0172.1

© 2025 Author(s). This published article is licensed under the terms of a Creative Commons Attribution 4.0 International (CC BY 4.0) License



Li et al. 2012, 2017). In the Marsdiep–Vlie double-inlet system of the western Wadden Sea, however, momentum dissipation on the intertidal habitats results in weakened tides and enhanced flood dominance (Hepkema et al. 2018). This highlights the importance of understanding the dominant processes that control the intertidal habitat roles in modulating estuarine hydrodynamics (e.g., tidal currents, asymmetry, residual circulation) under various natural forcings (e.g., tides, waves, river discharge, winds), human activities, and climate change (Murray et al. 2019; Nienhuis et al. 2020; Schuerch et al. 2018).

Numerous studies on intertidal habitats have been conducted using field observations (e.g., Mariotti and Fagherazzi 2012), numerical simulations (e.g., Chen et al. 2010; Li et al. 2018a; Yang and Wang 2015), and analytical modeling (e.g., Hepkema et al. 2018). Speer and Aubrey (1985) utilized a basic one-dimensional numerical model to demonstrate that in idealized shallow estuaries, the expansion of intertidal areas results in a dampened semidiurnal tide, amplified quarter-diurnal tide, and a reduction in tidal range. This reduction becomes more noticeable with increased bottom friction or decreased intertidal bed slope. Jay (1991) set up a linearized analytical model for narrow tidal estuaries with intertidal flats, highlighting the significant influence of bed friction and topographic convergence on tidal wave propagation. Friedrichs and Madsen (1992) formulated a nonlinear diffusion model for tidal dynamics in strongly frictional shallow estuaries, considering quadratic bottom friction and water storage over intertidal flats while disregarding acceleration and intertidal water velocities. Their analytical solution suggests that intertidal habitats lead to ebb dominance by intensifying temporal variations in embayment width. Fortunato and Oliveira (2005) examined the celerity difference at high and low tide in a channel–flat system, using an analytical model, and found that tidal flats enhance ebb dominance. Based on numerical simulations, Picado et al. (2010) demonstrated that the expansion of intertidal areas in an extensive lagoon increases the tidal prism and enhances tidal currents. Winterwerp and Wang (2013) employed an analytical approach similar to that of Jay (1991) while omitting flow velocities over intertidal areas. They found that the loss of water storage over intertidal habitats due to embankments and reclamation works enhances flood dominance in small estuaries. Hepkema et al. (2018) extended the model of Speer and Aubrey (1985) and stressed the significance of momentum dissipation over intertidal flats in attenuating the primary tidal wave. Using a depth-integrated numerical model, Finotello et al. (2023) found that the loss of intertidal areas in a macrotidal lagoon increases the mean high-water levels due to the reduced energy dissipation during flood tide.

Despite key findings derived from these prior studies, the specific contributions of various physical processes to intertidal effects on estuarine hydrodynamics and the dominant mechanisms controlling these effects remain underexplored. Due to technical difficulties in field observation, long-term and large-scale data are scarce on the intertidal habitat (Chen et al. 2010; Yang and Wang 2015), leading to challenges in conducting systematic analyses of intertidal effects at a high resolution or under varying forcing conditions. Moreover, numerical models are often too complex to disentangle the

contributions of different processes to the impact of intertidal habitats, making it challenging to identify the dominant mechanisms controlling the interactions between intertidal and channel waters. They also come with high computational cost, hence are limited to a small number of scenarios and insufficient for systematic sensitivity studies (Kumar et al. 2016; Schuttelaars et al. 2013). Another type of models, the so-called (semi)analytical models, are computationally cheap and effective for systematic investigation of physical processes controlling estuarine dynamics (e.g., Kumar et al. 2016) but are limited to one-dimensional models when including intertidal regions (Friedrichs and Madsen 1992; Hepkema et al. 2018; Jay 1991). Therefore, interactions between intertidal and channel tidal dynamics, for example, through lateral circulations that can result in sediment spillover from the channel onto mudflats and trap sediments on the flats (Mariotti and Fagherazzi 2012), remain poorly understood. Also, these analytical models assume longitudinal momentum transfer over the intertidal zone to be zero, i.e., neglecting longitudinal intertidal velocities, hence ignoring the two-way interactions between channel and intertidal water motions. These simplifications can make these models inconsistent for applications in estuaries with extensive intertidal areas or nonnegligible currents over the intertidal area (Jay 1991). This poses great challenges in systematically investigating the impact of intertidal habitat changes on estuarine flooding/erosion risks and the estuarine ecosystem services in the face of accelerating climate change and growing human demands.

Therefore, we have three main goals in this study: 1) to develop a three-dimensional, semianalytical estuarine hydrodynamic model that resolves the interactions between intertidal and channel waters; 2) to systematically investigate various physical processes that control the impact of intertidal habitats on hydrodynamics (i.e., tidal elevation, tidal current, residual circulation, and tidal asymmetry); and 3) to explore the sensitivity of these intertidal impacts to the intertidal (e.g., width, position) and estuarine (e.g., convergence, length) characteristics. To that end, we adopt a three-dimensional (3D), semianalytical modeling approach similar to Kumar et al. (2016, 2017) due to its capability to dissect the contributions of different physical processes controlling estuarine water motion. Extending the model of Kumar et al. (2016) by including intertidal habitats, we first resolve the influence of intertidal habitats on estuarine hydrodynamics in a short, tidally dominated and well-mixed estuary (considered as the default system in this study). Then, we systematically investigate the interactions between the channel and intertidal water motions and their sensitivity to characteristics of intertidal habitats and estuaries. In this study, we focus primarily on the effects of intertidal habitat changes resulting from embankment, reclamation, and habitat creation or restoration. A comprehensive understanding of various mechanisms of intertidal effects on estuarine hydrodynamics derived from this study will serve as a crucial scientific foundation for developing cost-effective and sustainable nature-based solutions, such as intertidal habitat creation and restoration, to manage estuarine climate risks.

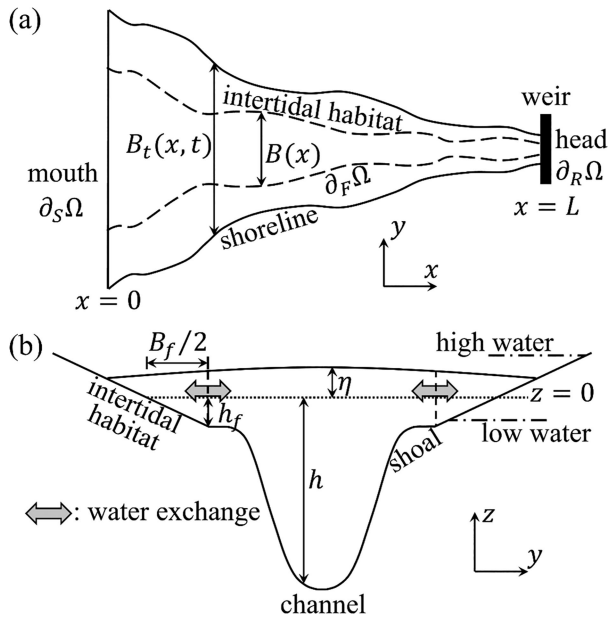


FIG. 1. (a) The top view and (b) cross-sectional view of an idealized estuary, with x , y , and z being the longitudinal, lateral, and vertical coordinates. The landward, seaward, and side boundaries of the permanently submerged model domain are demonstrated by $\partial_R\Omega$, $\partial_S\Omega$, and $\partial_F\Omega$, respectively. The width of the permanently submerged region is denoted by $B = B(x)$, and L is the estuary length. The total estuary width, denoted by $B_t = B_t(x, t)$, and the width of intertidal areas on both sides are functions of time (t). The bottom and free surface are located at $z = -h(x, y)$ and $z = \eta(x, y, t)$, defined with respect to the undisturbed water level at $z = 0$ (dotted line). The gray arrows represent the lateral water exchange across the interface $\partial_F\Omega$ (dashed line). The dashed-dotted lines indicate the high and low water levels.

This paper is structured as follows: The research methodology is introduced in section 2; in section 3, the model performance, impacts of intertidal habitats on estuarine hydrodynamics and their controlling processes, and corresponding sensitivities to various parameters are investigated; section 4 briefly discusses implications of interactions between intertidal and channel waters together with model limitations; and conclusions are drawn in section 5.

2. Methodology

a. Model description

To systematically investigate the impact of intertidal habitats on estuarine hydrodynamics, the semianalytical hydrodynamic model of Kumar et al. (2016, 2017) is extended to resolve the interactions between intertidal and channel waters. Considering the tidal amplitude to be one order of magnitude smaller than the water depth, Kumar et al. (2016, 2017) resolved the 3D estuarine dynamics within the permanently submerged (channel and shoal) area (as depicted between the two dashed boundaries in Fig. 1a). In the present study, we extend their model by resolving the intertidal

water motion using the one-dimensional (1D) shallow-water equations. The intertidal water motion is dynamically coupled with the channel water motion through the lateral water and momentum transport across the interface between the intertidal and channel regions (located at $y = \pm B/2$; see Fig. 1).

The extended 1D intertidal model domain, located on either side of the 3D permanently submerged model domain (referred to as Ω), stretches across intertidal areas from the time-varying shoreline to the side boundary $\partial_F\Omega$. Hereafter, we will term the expanse between the shorelines and $\partial_F\Omega$ as the intertidal region, while the permanently submerged channel and shoals encompassed by $\partial_F\Omega$ will be referred to as the channel region (Fig. 1). The interface between the intertidal and channel regions $\partial_F\Omega$ will be referred to as the intertidal-channel interface hereinafter. Following Friedrichs and Aubrey (1994), the intertidal water depth is assumed to decrease linearly toward the shorelines along the lateral direction (y), with $h_f = h_f(x)$ as the water depth at $\partial_F\Omega$ and $B_f = B_f(x)$ as the total intertidal habitat width at $z = 0$ (Fig. 1b).

1) GOVERNING EQUATIONS AND BOUNDARY CONDITIONS

(i) Water motion in the channel region

The water motion in the channel area is described by the three-dimensional shallow-water equations, utilizing the hydrostatic assumption and Boussinesq approximation (Cushman-Roisin and Beckers 2011):

$$\nabla \cdot \mathbf{U} = 0, \quad (1)$$

$$\frac{\partial u}{\partial t} + \mathbf{U} \cdot (\nabla u) = f v - g \frac{\partial \eta}{\partial x} - \frac{g}{\rho_0} \int_z^\eta \frac{\partial \rho}{\partial x} dz + \frac{\partial}{\partial z} \left(A_v \frac{\partial u}{\partial z} \right), \quad (2)$$

$$\frac{\partial v}{\partial t} + \mathbf{U} \cdot (\nabla v) = -f u - g \frac{\partial \eta}{\partial y} - \frac{g}{\rho_0} \int_z^\eta \frac{\partial \rho}{\partial y} dz + \frac{\partial}{\partial z} \left(A_v \frac{\partial v}{\partial z} \right), \quad (3)$$

where $\mathbf{U} = (u, v, w)$ denotes the velocity vector, with u , v , and w as the velocity components in the along-estuary (x), cross-estuary (y), and vertical (z) directions, respectively. The term g is the acceleration of gravity, f is the Coriolis parameter, and $A_v(x, y)$ is the vertical eddy viscosity assumed to be vertically uniform and time independent. The water density is given by ρ , calculated by $\rho = \rho_0(1 + \beta S)$, with $\rho_0 = 1025 \text{ kg m}^{-3}$ as the reference water density, $\beta = 7.8 \times 10^{-4} \text{ psu}^{-1}$ as the haline contraction coefficient, and $S(x, y)$ as the salinity. In our model, salinity is prescribed to be vertically homogenous and time independent to allow for a diagnostic calculation of gravitational circulation (driven by the baroclinic pressure gradient) under the influence of intertidal habitats.

At the seaward boundary, the sea surface elevation is prescribed with a semidiurnal (M_2), quarter-diurnal (M_4), and residual (M_0 , i.e., tidally averaged) component:

$$\begin{aligned} \eta(x, y, t) = & a_{M_2}(x, y) \cos(\sigma t) + a_{M_4}(x, y) \cos[2\sigma t - \varphi(x, y)] \\ & + a_{M_0}(x, y), \quad \text{at } (x, y) \in \partial_S\Omega. \end{aligned} \quad (4a)$$

Here, a_{M_2} , a_{M_4} , and φ denote the M_2 and M_4 tidal amplitudes and the relative phase between the M_2 and M_4 tidal components at the seaward boundary, with $\sigma \sim 1.4 \times 10^{-4} \text{ s}^{-1}$ as the M_2 tidal frequency, and a_{M_0} is the prescribed residual water level at the seaward boundary. However, numerical instabilities can occur when utilizing an arbitrary prescribed tidal level at the seaward boundary. Therefore, the model domain is extended seaward to reduce numerical uncertainties when resolving estuarine hydrodynamics [see details in Wei et al. (2017)]. At the extended seaward boundary of the computational domain, a laterally uniform barotropic sea surface elevation is considered, ensuring that the width-averaged amplitudes and phase differences of each tidal constituent in the water level η^m at $\partial_S\Omega$,

$$\eta^m = a_{M_2}^m \cos(\sigma t) + a_{M_4}^m \cos(2\sigma t - \varphi^m) + a_{M_0}^m, \quad (4b)$$

match their prescribed values. Here, $a_{M_2}^m$, $a_{M_4}^m$, φ^m , and $a_{M_0}^m$ are the prescribed width averages of $a_{M_2}(x, y)$, $a_{M_4}(x, y)$, $\varphi(x, y)$, and $a_{M_0}(x, y)$ at $\partial_S\Omega$. By combining the laterally uniform water level at the seaward boundary of the computational domain and the abovementioned prescribed parameters, we can derive the spatial and temporal variations of η [i.e., $a_{M_2}(x, y)$, $a_{M_4}(x, y)$, $\varphi(x, y)$, and $a_{M_0}(x, y)$] at $\partial_S\Omega$.

A constant river discharge R_c is imposed at the landward boundary of the channel region, where the tidal discharge vanishes:

$$\int_{-h}^{\eta} \mathbf{u}_h \cdot \mathbf{n}_h dz = R_i, \text{ with } R_i(x, y) = \frac{R_c}{B_r}, \quad \text{at } (x, y) \in \partial_R\Omega, \quad (5)$$

where $\mathbf{u}_h = (u, v)$ is the horizontal velocity vector and \mathbf{n}_h is the horizontal unit normal vector pointing outwards. The depth-integrated river flux per unit width R_i is assumed to be laterally uniform with B_r the width of the landward boundary.

Extending from Kumar et al. (2016), a nonzero normal water transport F_n is allowed across the intertidal-channel interface:

$$\int_{-h}^{\eta} \mathbf{u}_h \cdot \mathbf{n}_h dz = F_n, \quad \text{with } \mathbf{n}_h = \frac{\left[-\frac{1}{2} \frac{dB}{dx}, \text{sign}(y)\right]}{\sqrt{1 + \frac{1}{4} \left(\frac{dB}{dx}\right)^2}} \quad \text{at } (x, y) \in \partial_F\Omega. \quad (6)$$

Here, F_n is dynamically coupled with the intertidal water motion, which is positive when the normal transport is directed toward the intertidal habitats and negative when directed toward the deep channel. This lateral water exchange is associated with lateral dynamics in the channel region, which can come from various sources such as lateral density gradients and Coriolis deflection [see Eq. (3)] or lateral bathymetric variations and estuary width convergence [as shown by Wei et al. (2017)]. Discontinuous intertidal habitats along the estuary are allowed to account for local losses of intertidal habitats due to construction of flood defenses and/or land reclamation. In regions without intertidal habitats, the water

exchange is zero ($F_n = 0$), as considered by Kumar et al. (2016).

At the free surface, the kinematic and shear-free (i.e., zero shear stress) boundary conditions are imposed:

$$w = \frac{\partial \eta}{\partial t} + \mathbf{u}_h \cdot (\nabla \eta), \quad \text{and } A_v \frac{\partial \mathbf{u}_h}{\partial z} = (0, 0), \quad \text{at } z = \eta. \quad (7)$$

The bottom is impermeable, and a partial-slip boundary condition is applied, following the linearization of the bed shear stress (Lorentz 1926):

$$w = -\mathbf{u}_h \cdot (\nabla h), \quad \text{and } A_v \frac{\partial \mathbf{u}_h}{\partial z} = s\mathbf{u}_h, \quad \text{at } z = -h. \quad (8)$$

Here, $s(x, y)$ is the slip parameter, which varies from 0 in frictionless scenarios (free slip) to a large value in strongly frictional scenarios (no slip).

(ii) Water motion in the intertidal region

Like the water motion in the channel region, the intertidal water motion can also be described by the 3D shallow-water equations [Eqs. (1)–(3)]. Then, the 1D intertidal model equations are derived by averaging these equations over the intertidal cross section and applying the vertical and horizontal boundary conditions. Vertically, the corresponding kinematic and dynamic boundary conditions [Eqs. (7) and (8)] are imposed at the free surface and the bottom. Horizontally, the water and momentum transport at the time-varying shoreline vanishes (due to zero total water depth), while the water and momentum transport at the intertidal-channel interface is dynamically resolved by coupling intertidal and channel water motions. In this study, the bathymetry is assumed to be smooth at the interface between intertidal and channel regions; hence, the velocities are continuous at $\partial_F\Omega$.

To link intertidal waters to channel waters consistently, two matching conditions should be obtained at the side boundary $\partial_F\Omega$, ensuring the continuity of water level and water mass, respectively. The latter condition is achieved by deriving the lateral water exchange between the intertidal and channel regions, i.e., ensuring that the lateral water transport F_n remains the same at the side boundary of both regions [see Eqs. (6) and (10)]. Regarding the first matching condition, inspired by the numerical results of Le Hir et al. (2000), the sea surface elevation in the intertidal region is assumed to vary linearly along the lateral direction, and the lateral gradient of this sea surface elevation in the intertidal region is assumed to equal the lateral surface gradient at $\partial_F\Omega$. This linear assumption accounts for continuity of both the sea surface elevation and its lateral gradient at the interface $\partial_F\Omega$. It also qualitatively represents the water volume deficit during flood and lagged volume during ebb induced by the lateral sea surface gradient as compared to a rigid-lid approximation [see Fig. 6 in Nidzieko and Ralston (2012)]. The intertidal cross-sectionally averaged water level η_f is derived from the intertidal cross-section area based on the linear intertidal surface elevation (see appendix A, section a):

$$\eta_f(x, t) = [\eta(x, y, t) + h_f] \sqrt{\frac{2h_f/B_f}{2h_f/B_f - \text{sign}(y)\partial_y \eta(x, y, t)}} - h_f, \quad \text{at } (x, y) \in \partial_F \Omega, \quad (9)$$

where the intertidal water level η_f (for 1D intertidal model domain) is a function of the water level η at $\partial_F \Omega$ (obtained from the 3D channel model), i.e., the matching condition for water level. Finally, the intertidal water motion is coupled dynamically with the channel water motion through these two matching conditions.

By averaging Eq. (1) over the intertidal cross section, the one-dimensional continuity equation of intertidal water is derived (see details in [appendix A, section b](#)) as

$$\frac{B_f(1 + \eta_f/h_f)}{2} \frac{\partial \eta_f}{\partial t} + \frac{\partial}{\partial x} \left[u_f \frac{h_f B_f (\eta_f/h_f + 1)^2}{4} \right] - \alpha F_n = 0, \quad \text{with } \alpha = \sqrt{1 + \frac{1}{4} \left(\frac{dB}{dx} \right)^2}. \quad (10)$$

Here, $u_f(x, t)$ is the intertidal cross-sectionally averaged longitudinal velocity. Equation (10) shows that the water exchange F_n is determined by the temporal variation rate of the intertidal water storage (first term) and the divergence of the along-estuary water flux across the intertidal cross section (second term), together with the estuary convergence term α .

Likewise, the one-dimensional intertidal momentum equation is derived by averaging Eq. (2) over the intertidal cross section (see [appendix A, section c](#)):

$$\begin{aligned} \frac{\partial u_f}{\partial t} + u_f \frac{\partial u_f}{\partial x} - 4\alpha \frac{M_n - u_f F_n}{B_f h_f (\eta_f/h_f + 1)^2} \\ = -g \frac{\partial \eta_f}{\partial x} - \frac{g}{\rho_0} \frac{h_f + \eta_f \partial \rho_f}{3} \frac{\partial \rho_f}{\partial x} - \frac{2s_f}{h_f + \eta_f} u_f, \end{aligned} \quad (11)$$

with $s_f(x)$ being the intertidal slip parameter and M_n being the lateral momentum exchange across the intertidal-channel interface:

$$M_n = \int_{-h}^{\eta} (\mathbf{u}_h \cdot \mathbf{n}_h) u \, dz, \quad \text{at } (x, y) \in \partial_F \Omega. \quad (12)$$

By assuming a smooth bathymetry in the channel and intertidal regions, the same lateral momentum transport M_n is used over both regions due to the continuity of velocities at $\partial_F \Omega$. The term $\partial_x \rho_f$ is the longitudinal gradient of water density averaged over the intertidal cross section, assumed to be equal to that of the channel water at $\partial_F \Omega$ [i.e., $\partial_x \rho_f = \partial_x \rho$ at $(x, y) \in \partial_F \Omega$].

When considering intertidal habitats distributed throughout the entire estuary (as in [Fig. 1](#)), like in the channel region, the intertidal water level at the seaward limit of the intertidal region is prescribed as

$$\eta_f(x, t) = a_{M_2}^f \cos(\sigma t) + a_{M_4}^f \cos(2\sigma t - \phi^f) + a_{M_0}^f, \quad \text{at } (x, y) \in \partial_F \Omega \cap \partial_S \Omega. \quad (13)$$

Here, $a_{M_2}^f$, $a_{M_4}^f$, $a_{M_0}^f$, and ϕ^f denote the M_2 , M_4 , M_0 tidal amplitudes, and the relative phase between the M_2 and M_4 tidal components laterally averaged over the seaward limit of the intertidal region. These parameters are calculated from the prescribed water level in the channel region [Eq. (4a)] and the linear assumption of the intertidal sea surface elevation [Eq. (9)]. In the case where the water level in the channel region is prescribed to be constant at the seaward boundary (i.e., $\partial_y \eta = 0$), the intertidal water level at this boundary matches that in the channel region: $\eta_f = \eta$.

A constant river discharge R_f is imposed at the landward limit of the intertidal region, where the tidal flux vanishes:

$$u_f(x, t) = R_f^i, \quad \text{with } R_f^i = \frac{2R_f}{B_f h_f}, \quad \text{at } (x, y) \in \partial_F \Omega \cap \partial_R \Omega. \quad (14)$$

Here, R_f^i is the river flux averaged over the intertidal cross section. Equations (5) and (14) show that a total constant river discharge $R = R_c + R_f$ is prescribed at the landward boundary of the estuary. In this study, R_c and R_f are assumed to be proportional to the cross-sectional areas in the channel and intertidal regions for simplicity.

Given that intertidal habitats can be partially distributed along the estuary, however, the seaward/landward limit of these habitats may not be located at the estuary mouth/head. Hence, a closed boundary condition (i.e., $u_f = 0$) is applied at the habitat's seaward/landward limit when the limit is located in the interior estuary.

2) PERTURBATION METHOD

A perturbation method is taken to solve the system of Eqs. (1)–(14). As a first step, the dimensionless form of these equations is derived using a scaling analysis ([appendix B](#)). Next, all terms in the dimensionless equations are compared to a small parameter $\epsilon = a_{M_2}^m/H \ll 1$, with H being the mean water depth at the seaward boundary. Then, all physical variables are expanded asymptotically with respect to ϵ :

$$\psi = \sum_{i=0}^{\infty} \epsilon^i \psi_i = \psi_0 + \epsilon \psi_1 + \epsilon^2 \psi_2 + \dots, \quad (15)$$

where ψ indicates any physical variable (η , u , v , w , η_f , and u_f). By collecting all terms at the same order of ϵ , a system of equations at each order, which describes the water motion at different tidal frequencies, is derived. The equations at each order can then be separately solved. Second and higher orders are neglected in this paper for simplicity.

The governing equations and corresponding boundary conditions of the channel water motion at each order of ϵ except for the side boundary condition [i.e., Eq. (6) imposed at $\partial_F \Omega$] are the same as those presented in [Kumar et al. \(2016, 2017\)](#).

(i) Leading-order water motion

Following [Kumar et al. \(2016\)](#), the leading-order [$O(1)$] system of the channel water motion equations reads

$$\nabla \cdot \mathbf{U}_{M_2} = 0, \quad (16a) \quad \nabla \cdot \mathbf{U}_{M_j} = 0, \quad (21a)$$

$$\frac{\partial u_{M_2}}{\partial t} = f v_{M_2} - g \frac{\partial \eta_{M_2}}{\partial x} + \frac{\partial}{\partial z} \left(A_v \frac{\partial u_{M_2}}{\partial z} \right), \quad (16b) \quad \frac{\partial u_{M_j}}{\partial t} + \underbrace{\mathbf{U}_{M_2} \cdot (\nabla u_{M_2})}_{AC} = f v_{M_j} - g \frac{\partial \eta_{M_j}}{\partial x} + \underbrace{\frac{g}{\rho_0} \frac{\partial p}{\partial x} z}_{GC} + \frac{\partial}{\partial z} \left(A_v \frac{\partial u_{M_j}}{\partial z} \right), \quad (21b)$$

$$\frac{\partial v_{M_2}}{\partial t} = -f u_{M_2} - g \frac{\partial \eta_{M_2}}{\partial y} + \frac{\partial}{\partial z} \left(A_v \frac{\partial v_{M_2}}{\partial z} \right), \quad (16c) \quad \frac{\partial v_{M_j}}{\partial t} + \underbrace{\mathbf{U}_{M_2} \cdot (\nabla v_{M_2})}_{AC} = -f u_{M_j} - g \frac{\partial \eta_{M_j}}{\partial y} + \underbrace{\frac{g}{\rho_0} \frac{\partial p}{\partial y} z}_{GC} + \frac{\partial}{\partial z} \left(A_v \frac{\partial v_{M_j}}{\partial z} \right). \quad (21c)$$

with the leading-order horizontal boundary conditions:

$$\eta_{M_2} = a_{M_2} \cos(\sigma t), \quad \text{at } (x, y) \in \partial_S \Omega, \quad (17a)$$

$$\int_{-h}^0 \mathbf{u}_{h_{M_2}} \cdot \mathbf{n}_h dz = 0, \quad \text{at } (x, y) \in \partial_R \Omega, \quad (17b)$$

$$\int_{-h}^0 \mathbf{u}_{h_{M_2}} \cdot \mathbf{n}_h dz = F_{nM_2}, \quad \text{at } (x, y) \in \partial_F \Omega. \quad (17c)$$

The boundary condition [Eq. (17c)], which is different from that used in Kumar et al. (2016), shows that the leading-order M_2 water motion is modulated by the leading-order water exchange in the presence of intertidal habitats ($F_{nM_2} \neq 0$). The leading-order vertical boundary conditions at the still water level and the bottom are

$$w_{M_2} = \frac{\partial \eta_{M_2}}{\partial t}, \quad \text{and } A_v \frac{\partial \mathbf{u}_{h_{M_2}}}{\partial z} = (0, 0), \quad \text{at } z = 0, \quad (18a)$$

$$w_{M_2} = -\mathbf{u}_{h_{M_2}} \cdot (\nabla h), \quad \text{and } A_v \frac{\partial \mathbf{u}_{h_{M_2}}}{\partial z} = s \mathbf{u}_{h_{M_2}}, \quad \text{at } z = -h. \quad (18b)$$

Based on the nondimensional intertidal water motion equations [see Eqs. (B2) and (B3) in appendix B], the leading-order [$O(1)$] continuity and momentum equations for the intertidal water motion read

$$\frac{B_f}{2} \frac{\partial \eta_{f_{M_2}}}{\partial t} + \frac{\partial}{\partial x} \left(u_{f_{M_2}} \frac{h_f B_f}{4} \right) - \alpha F_{nM_2} = 0, \quad (19a)$$

$$\frac{\partial u_{f_{M_2}}}{\partial t} + \frac{2s_f}{h_f} u_{f_{M_2}} + g \frac{\partial \eta_{f_{M_2}}}{\partial x} = 0, \quad (19b)$$

with the leading-order boundary conditions [Eqs. (B12) and (B13)]:

$$\eta_{f_{M_2}} = a_{f_{M_2}}^f \cos(\sigma t), \quad \text{at } (x, y) \in \partial_F \Omega \cap \partial_S \Omega, \quad (20a)$$

$$u_{f_{M_2}} = 0, \quad \text{at } (x, y) \in \partial_F \Omega \cap \partial_R \Omega. \quad (20b)$$

(ii) First-order water motion

Following Kumar et al. (2017), the first-order [$O(\epsilon^1)$] system of the channel water motion equations reads

Here, the subscript M_j indicates the residual ($M_0, j = 0$) and quarter-diurnal ($M_4, j = 4$) tidal component of the water motion, respectively. The underbrace $\underbrace{\cdot}_{\cdot}$ denotes various physical processes in the channel regions that force the first-order flow. The first-order horizontal boundary conditions are

$$\eta_{M_j} = \underbrace{a_{M_4} \cos(2\sigma t - \varphi) + a_{M_0}}_{EF}, \quad \text{at } (x, y) \in \partial_S \Omega, \quad (22a)$$

$$\int_{-h}^0 \mathbf{u}_{h_{M_j}} \cdot \mathbf{n}_h dz + \underbrace{(\eta_{M_2} \mathbf{u}_{h_{M_2}}|_{z=0}) \cdot \mathbf{n}_h}_{TRFSD} = \underbrace{R_i}_{RD}, \quad \text{at } (x, y) \in \partial_R \Omega, \quad (22b)$$

$$\int_{-h}^0 \mathbf{u}_{h_{M_j}} \cdot \mathbf{n}_h dz + \underbrace{(\eta_{M_2} \mathbf{u}_{h_{M_2}}|_{z=0}) \cdot \mathbf{n}_h}_{TRFSD} = F_{nM_j}, \quad \text{at } (x, y) \in \partial_F \Omega. \quad (22c)$$

The side boundary condition [Eq. (22c)] is different from that used in Kumar et al. (2017) (for $F_{nM_j} \neq 0$), which considers the impact of the first-order water exchange on modulating the M_0 and M_4 water motions. The first-order vertical boundary conditions at the still water level and the bottom are as follows:

$$w_{M_j} = \frac{\partial \eta_{M_j}}{\partial t} + \underbrace{\nabla \cdot (\eta_{M_2} \mathbf{u}_{h_{M_2}})}_{TRFSD}, \quad \text{and} \quad A_v \frac{\partial \mathbf{u}_{h_{M_j}}}{\partial z} = \underbrace{-A_v \eta_{M_2} \frac{\partial^2 \mathbf{u}_{h_{M_2}}}{\partial z^2}}_{NS}, \quad \text{at } z = 0, \quad (23a)$$

$$w_{M_j} = -\mathbf{u}_{h_{M_j}} \cdot (\nabla h), \quad \text{and } A_v \frac{\partial \mathbf{u}_{h_{M_j}}}{\partial z} = s \mathbf{u}_{h_{M_j}}, \quad \text{at } z = -h. \quad (23b)$$

Equations (21)–(23) show that the first-order flow is forced by the external tidal/residual forcing (EF), gravitational circulation (GC), river discharge (RD), nonlinear tidal rectification of the M_2 tide (i.e., advection, denoted by AC), shear-free surface condition (NS), and tidal return flow compensating the Stokes drift (TRFSD).

The nondimensional intertidal water motion equations [Eqs. (B2) and (B3)] (see appendix B) also yield the first-order [$O(\epsilon^1)$] equations for intertidal water motion:

$$\frac{B_f}{2} \frac{\partial \eta_{f_{M_j}}}{\partial t} + \frac{\partial}{\partial x} \left(u_{f_{M_j}} \frac{h_f B_f}{4} \right) + \underbrace{\frac{B_f \eta_{f_{M_2}}}{2 h_f} \frac{\partial \eta_{f_{M_2}}}{\partial t} + \frac{\partial}{\partial x} \left(\eta_{f_{M_2}} u_{f_{M_2}} \frac{B_f}{2} \right)}_{\text{TF}} - \alpha F_{n_{M_j}} = 0, \quad (24a)$$

$$\begin{aligned} & \frac{\partial u_{f_{M_j}}}{\partial t} + \frac{2s_f}{h_f} u_{f_{M_j}} + g \frac{\partial \eta_{f_{M_j}}}{\partial x} + \underbrace{\frac{g}{\rho_0} \frac{h_f \partial \rho_f}{3 \partial x}}_{\text{GC}} \\ &= \underbrace{\frac{2s_f}{h_f^2} \eta_{f_{M_2}} u_{f_{M_2}} - u_{f_{M_2}} \frac{\partial u_{f_{M_2}}}{\partial x} + 4\alpha \frac{M_{n_{M_j}} - u_{f_{M_2}} F_{n_{M_2}}}{h_f B_f}}_{\text{TF}}, \end{aligned} \quad (24b)$$

with the first-order momentum exchange

$$M_{n_{M_j}} = \int_{-h}^0 (\mathbf{u}_{h_{M_2}} \cdot \mathbf{n}_h) u_{M_2} dz, \quad \text{at } (x, y) \in \partial_F \Omega. \quad (25)$$

The first-order boundary conditions [Eqs. (B12) and (B13)] read

$$\eta_{f_{M_j}} = \underbrace{a_{M_4}^f \cos(2\sigma t - \varphi^f) + a_{M_0}^f}_{\text{EF}}, \quad \text{at } (x, y) \in \partial_F \Omega \cap \partial_S \Omega, \quad (26a)$$

$$u_{f_{M_j}} = \underbrace{R_i^f}_{\text{RD}}, \quad \text{at } (x, y) \in \partial_F \Omega \cap \partial_R \Omega. \quad (26b)$$

Here, the term TF includes processes associated with the nonlinear interactions of the M_2 tide in the intertidal region, which combines the nonlinear effects of the water loss/gain [Eq. (24a)] and the momentum loss/gain [Eq. (24b)] of the intertidal water.

3) SEMIANALYTICAL METHOD

A semianalytical approach is utilized to resolve the intertidal and channel water motions at each order of ϵ [Eqs. (16)–(26)]. First, the physical variables are expressed using the complex amplitude to derive analytical relationships between current velocities and sea surface gradients, as well as the vertical distribution of velocities. Then, the finite element method is applied to numerically resolve their horizontal distributions.

(i) Analytical approach

The physical variables at the leading order can be written as

$$\begin{aligned} & (u_{M_2}, v_{M_2}, \eta_{M_2}, u_{f_{M_2}}, \eta_{f_{M_2}}, F_{n_{M_2}}) \\ &= \Re\{(\hat{u}_{M_2}, \hat{v}_{M_2}, \hat{\eta}_{M_2}, \hat{u}_{f_{M_2}}, \hat{\eta}_{f_{M_2}}, \hat{F}_{n_{M_2}}) e^{i\sigma t}\}. \end{aligned} \quad (27)$$

Here, the hat ($\hat{\cdot}$) indicates the complex amplitude and $\Re\{\cdot\}$ denotes the real part of a complex variable. Similar to Kumar et al. (2016), the leading-order current velocities in the 3D channel model domain can be written as a function of sea surface gradients:

$$\hat{\mathbf{u}}_{h_{M_2}} = \mathbf{C}(z, \sigma) \nabla \hat{\eta}_{M_2}, \quad \text{with } \mathbf{C}(z, \sigma) = \begin{bmatrix} C_1(z, \sigma) & C_2(z, \sigma) \\ -C_2(z, \sigma) & C_1(z, \sigma) \end{bmatrix}. \quad (28)$$

The coefficients C_1 and C_2 are functions of the vertical coordinate and the tidal frequency, which determine the vertical structure of the channel M_2 current velocities [see their analytical expressions in Kumar et al. (2016)].

By substituting Eq. (27) into Eq. (19b), we can rewrite the leading-order intertidal current velocity as a function of the intertidal sea surface gradient:

$$\hat{u}_{f_{M_2}} = \beta_{M_2} \frac{\partial \hat{\eta}_{f_{M_2}}}{\partial x}, \quad \text{with } \beta_{M_2} = \frac{-g}{i\sigma + 2s_f/h_f}. \quad (29)$$

By substituting Eqs. (27) and (29) into Eq. (19a), the leading-order lateral water exchange across the interface $\partial_F \Omega$ is derived as

$$\hat{F}_{n_{M_2}} = \frac{B_f}{2\alpha} i\sigma \hat{\eta}_{f_{M_2}} + \frac{1}{\alpha \partial x} \left(\beta_{M_2} \frac{h_f B_f}{4} \frac{\partial \hat{\eta}_{f_{M_2}}}{\partial x} \right). \quad (30)$$

Similarly, all physical variables at the first order of ϵ can be written as

$$\begin{aligned} & (u_{M_j}, v_{M_j}, \eta_{M_j}, u_{f_{M_j}}, \eta_{f_{M_j}}, F_{n_{M_j}}) \\ &= \Re\{(\hat{u}_{M_j}, \hat{v}_{M_j}, \hat{\eta}_{M_j}, \hat{u}_{f_{M_j}}, \hat{\eta}_{f_{M_j}}, \hat{F}_{n_{M_j}}) e^{i\sigma_j t}\}, \end{aligned} \quad (31)$$

with σ_j being the frequency of the residual flow ($\sigma_0 = 0$, for $j = 0$) or that of the M_4 tidal water motion ($\sigma_4 = 2\sigma$, for $j = 4$). As derived by Kumar et al. (2017), the channel current velocities at the first order read

$$\hat{\mathbf{u}}_{h_{M_j}} = \mathbf{C}(z, \sigma_j) \nabla \hat{\eta}_{M_j} + \mathbf{f}_{\text{GC}} + \mathbf{f}_{\text{AC}} + \mathbf{f}_{\text{NS}}, \quad (32)$$

with \mathbf{f}_{GC} , \mathbf{f}_{AC} , and \mathbf{f}_{NS} as the forcing vectors determined by corresponding forcing terms in the channel momentum equations and dynamic boundary conditions [Eqs. (21)–(23)]. Their analytical expressions, as functions of the vertical coordinate and the tidal frequency, can be found in Kumar et al. (2017) and are not repeated here.

The first-order intertidal current velocity can be derived from Eq. (24b):

$$\hat{u}_{f_{M_j}} = \beta_{M_j} \frac{\partial \hat{\eta}_{f_{M_j}}}{\partial x} + f_{\text{GC}}^m + f_{\text{TF}}^m, \quad \text{with } \beta_{M_j} = \frac{-g}{i\sigma_j + 2s_f/h_f}, \quad (33)$$

where f_{GC}^m is the forcing term of GC in the intertidal region [see Eq. (24b)]:

$$f_{\text{GC}}^m = \beta_{M_j} \frac{h_f}{3\rho_0} \frac{\partial \rho_f}{\partial x}, \quad (34)$$

and f_{TF}^m is the TF forcing term associated with the momentum loss/gain [see the momentum equation, Eq. (24b)] in the intertidal region:

$$\Re \left\{ \frac{g}{\beta_{M_j}} f_{\text{TF}}^m e^{i\sigma_j t} \right\} = u_{f_{M_2}} \frac{\partial u_{f_{M_2}}}{\partial x} - 4\alpha \frac{M_{nM_j} - u_{f_{M_2}} F_{nM_2}}{h_f B_f} - \frac{2s_f}{h_f^2} \eta_{f_{M_2}} u_{f_{M_2}}. \quad (35)$$

By substituting Eqs. (31) and (33) into Eq. (24a), the first-order lateral water exchange across the interface $\partial_F \Omega$ is derived as

$$\hat{F}_{nM_j} = \frac{B_f}{2\alpha} i\sigma_j \hat{\eta}_{f_{M_j}} + \frac{1}{\alpha} \frac{\partial}{\partial x} \left[\frac{h_f B_f}{4} \left(\beta_{M_j} \frac{\partial \hat{\eta}_{f_{M_j}}}{\partial x} + f_{\text{GC}}^m + f_{\text{TF}}^m \right) \right] + \frac{f_{\text{TF}}^c}{\alpha}, \quad (36)$$

with f_{TF}^c as the TF forcing term associated with the water loss/gain [see the continuity equation, Eq. (24a)] in the intertidal region:

$$\Re \{ f_{\text{TF}}^c e^{i\sigma_j t} \} = \frac{B_f \eta_{f_{M_2}}}{2h_f} \frac{\partial \eta_{f_{M_2}}}{\partial t} + \frac{1}{2} \frac{\partial}{\partial x} (B_f \eta_{f_{M_2}} u_{f_{M_2}}). \quad (37)$$

(ii) Numerical approach

Following Kumar et al. (2016, 2017), the channel and intertidal water levels at each order of ϵ can be derived by substituting the analytical expressions of the current velocities [Eqs. (28), (29), (32) and (33)] and water exchange [Eqs. (30) and (36)] into the depth-integrated channel continuity equations (from $z = -h$ to $z = 0$) and applying the associated boundary conditions [Eqs. (18) and (23)].

The governing equation of the leading-order water level in the channel model domain reads

$$\nabla \cdot (\mathbf{D}_{M_2} \nabla \hat{\eta}_{M_2}) + i\sigma \hat{\eta}_{M_2} = 0, \quad \text{with } \mathbf{D}_{M_2} = \int_{-h}^0 \mathbf{C}(z, \sigma) dz. \quad (38)$$

The corresponding boundary conditions are

$$\hat{\eta}_{M_2} = a_{M_2}, \quad \text{at } (x, y) \in \partial_S \Omega, \quad (39a)$$

$$(\mathbf{D}_{M_2} \nabla \hat{\eta}_{M_2}) \cdot \mathbf{n}_h = 0, \quad \text{at } (x, y) \in \partial_R \Omega, \quad (39b)$$

$$(\mathbf{D}_{M_2} \nabla \hat{\eta}_{M_2}) \cdot \mathbf{n}_h = \hat{F}_{nM_2}, \quad \text{at } (x, y) \in \partial_F \Omega. \quad (39c)$$

The governing equation for the leading-order water level is a two-dimensional linear elliptic partial differential equation, which is solved numerically by the finite element method (see appendix C, section a).

Likewise, the governing equation of the first-order channel water motion reads (Kumar et al. 2017)

$$\nabla \cdot (\mathbf{D}_{M_j} \nabla \hat{\eta}_{M_j} + \mathbf{F}) + i\sigma_j \hat{\eta}_{M_j} + F_{\text{TRFSD}}^\Omega = 0, \quad \text{with } \mathbf{D}_{M_j} = \int_{-h}^0 \mathbf{C}(z, \sigma_j) dz. \quad (40)$$

Here, the forcing term \mathbf{F} includes contributions of GC, AC, and NS:

$$\mathbf{F} = \int_{-h}^0 (\mathbf{f}_{\text{GC}} + \mathbf{f}_{\text{AC}} + \mathbf{f}_{\text{NS}}) dz, \quad \text{and}$$

$$\Re \{ F_{\text{TRFSD}}^\Omega e^{i\sigma_j t} \} = \nabla \cdot (\eta_{M_2} \mathbf{u}_{h_{M_2}}|_{z=0}). \quad (41)$$

The corresponding boundary conditions read

$$\hat{\eta}_{M_j} = F_{\text{EF}}, \quad \text{at } (x, y) \in \partial_S \Omega, \quad (42a)$$

$$(\mathbf{D}_{M_j} \nabla \hat{\eta}_{M_j} + \mathbf{F}) \cdot \mathbf{n}_h + F_{\text{TRFSD}}^{\partial \Omega} = R_i, \quad \text{at } (x, y) \in \partial_R \Omega, \quad (42b)$$

$$(\mathbf{D}_{M_j} \nabla \hat{\eta}_{M_j} + \mathbf{F}) \cdot \mathbf{n}_h + F_{\text{TRFSD}}^{\partial \Omega} = \hat{F}_{nM_j}, \quad \text{at } (x, y) \in \partial_F \Omega, \quad (42c)$$

with

$$\Re \{ F_{\text{EF}} e^{i\sigma_j t} \} = a_{M_4} \cos(2\sigma t - \varphi) + a_{M_0}, \quad \text{and}$$

$$\Re \{ F_{\text{TRFSD}}^\Omega e^{i\sigma_j t} \} = (\eta_{M_2} \mathbf{u}_{h_{M_2}}|_{z=0}) \cdot \mathbf{n}_h. \quad (43)$$

As this system of equations for the water level is linear, the forcing term associated with each of the different processes is included separately to solve the water motion driven by each process. This results in an explicit dissection of the first-order current velocities driven by different forcings. Similarly, the elliptic equation for the first-order water level is solved numerically (see appendix C, section b).

Therefore, the current velocity in the channel region is decomposed as

$$\mathbf{U} = \underbrace{\mathbf{U}_{M_2}}_{O(\epsilon^0)} + \underbrace{\mathbf{U}_{M_0} + \mathbf{U}_{M_4}}_{O(\epsilon^1)}. \quad (44)$$

Here, \mathbf{U}_{M_2} is the leading-order M_2 tidal current velocity vector, and \mathbf{U}_{M_0} and \mathbf{U}_{M_4} are the first-order residual (M_0) and quarter-diurnal (M_4) tidal current velocity vectors, which can be further decomposed into different contributions:

$$\mathbf{U}_{M_0} = \mathbf{U}_{M_0}^{\text{EF}} + \mathbf{U}_{M_0}^{\text{GC}} + \mathbf{U}_{M_0}^{\text{RD}} + \mathbf{U}_{M_0}^{\text{AC}} + \mathbf{U}_{M_0}^{\text{NS}} + \mathbf{U}_{M_0}^{\text{TRFSD}} + \mathbf{U}_{M_0}^{\text{TF}}, \quad (45)$$

$$\mathbf{U}_{M_4} = \mathbf{U}_{M_4}^{\text{EF}} + \mathbf{U}_{M_4}^{\text{AC}} + \mathbf{U}_{M_4}^{\text{NS}} + \mathbf{U}_{M_4}^{\text{TRFSD}} + \mathbf{U}_{M_4}^{\text{TF}}. \quad (46)$$

In this coupled system between the intertidal and channel waters, the intertidal velocity u_f and the tidal elevations η and η_f are decomposed in the same way as the current velocity \mathbf{U} . This means that intertidal water motions are also separately calculated in terms of different physical mechanisms.

As mentioned after [Eq. (17c)], the intertidal area affects the leading-order M_2 tidal water motion in the channel region through the M_2 water exchange across the interface $\partial_F \Omega$. Equations (45) and (46) also show that intertidal habitats modulate the first-order flow in the channel region in three ways, directly or indirectly. First, the inclusion of intertidal

TABLE 1. Definitions of acronyms of key physical processes.

Acronym	Definition	Equation
EF	External tidal/residual forcing	(22a), (26a)
GC	Gravitational circulation	(21b), (21c), (24b)
RD	River discharge	(22b), (26b)
AC	Advection/tidal rectification of the M_2 tide	(21b), (21c)
NS	No-shear condition at the free surface	(23a)
TRFSD	Tidal return flow that compensates Stokes drift	(22b), (22c), (23a)
TF	Nonlinear interactions of the M_2 tide over tidal flats	(24a), (24b)

areas leads to a direct contribution, TF, to the M_0 and M_4 tidal motions, driven by the nonlinear interactions of the M_2 tidal motion over the intertidal areas. Second, the intertidal water motion directly modulates the first-order processes (i.e., EF, GC, RD, AC, NS, and TRFSD) through the nonzero intertidal–channel water exchange at the M_0 and M_4 tidal frequencies. Finally, by modulating the leading-order M_2 tidal motion within the channel and the associated nonlinear terms, the inclusion of intertidal habitats indirectly affects the first-order M_0 and M_4 tidal water motions within the channel region associated with AC, NS, and TRFSD. All abbreviations of the various physical processes are summarized in Table 1.

b. Experiments design

1) DEFAULT EXPERIMENT

The default experiment considers an idealized, short, tidally dominated and well-mixed estuary, with a length L of 25 km and an exponentially decreasing width of the channel region B :

$$B = B_0 e^{-x/L_b}. \quad (47)$$

Here $B_0 = 5$ km is the width of the channel region at the mouth and $L_b = 30$ km is the estuarine convergence length.

The bathymetry of the channel region in the idealized estuary is characterized by a deep channel in the middle and submerged shoals on both sides:

$$h(x, y) = 0.5h_1(x) \left\{ 1 - \tanh \left[\left(k_c k_s \frac{y}{B} \right)^2 - k_s^2 \right] \right\} + h_2(x) \quad (48)$$

for $|y| \leq B/2$.

Here, k_c is the ratio of the submerged shoal width to the deep channel width and k_s measures the slope between the channel and shoal. The two depth functions $h_1(x)$ and $h_2(x)$ are determined by the water depth at $\partial_F \Omega$, h_f , and that at the thalweg ($y = 0$), $h_c(x)$:

$$h(x, \pm B/2) = 0.5h_1(x)[1 + \tanh(k_s^2 - 0.25k_c^2k_s^2)] + h_2(x) = h_f, \quad (49a)$$

$$h(x, 0) = 0.5h_1(x)[1 + \tanh(k_s^2)] + h_2(x) = h_c(x). \quad (49b)$$

The thalweg water depth decreases linearly landward: $h_c(x) = h_c^{\max}(1 - x/L) + h_c^{\min}x/L$, with h_c^{\max} and h_c^{\min} being the maximum and minimum channel depth at the seaward and

landward boundaries. The intertidal water depth increases linearly from 0 at the shoreline to h_f at $\partial_F \Omega$ (Fig. 2).

In this study, the width ratio between the intertidal and channel regions at the still/undisturbed water level (i.e., $z = 0$),

$$r_B = B_f/B, \quad (50)$$

is considered to be constant along the estuary. This means that the width of the intertidal regions decreases exponentially toward the head, and the width convergence rates of the channel and intertidal regions are identical (see Fig. 2).

In this study, the width-averaged water level induced by the M_4 and M_0 tidal constituents is required to vanish over the seaward boundary for simplicity, i.e., $a_{M_4}^n = a_{M_0}^n = 0$. In the default system, the width average of the semidiurnal tidal amplitude $a_{M_2}^n$ is set to be 2 m at the seaward boundary. The model domain is extended 20 km seaward to reduce numerical inconsistencies caused by the prescribed water level at the seaward boundary (Wei et al. 2017). A total constant river discharge $R = 20 \text{ m}^3 \text{ s}^{-1}$ is prescribed at the landward boundary. The effect of the Coriolis deflection is neglected for simplicity. The vertical eddy viscosity A_v and slip parameter s and s_f are assumed to be constant in time and space. Salinity is prescribed by a hyperbolic tangent function of x (Talke et al. 2009):

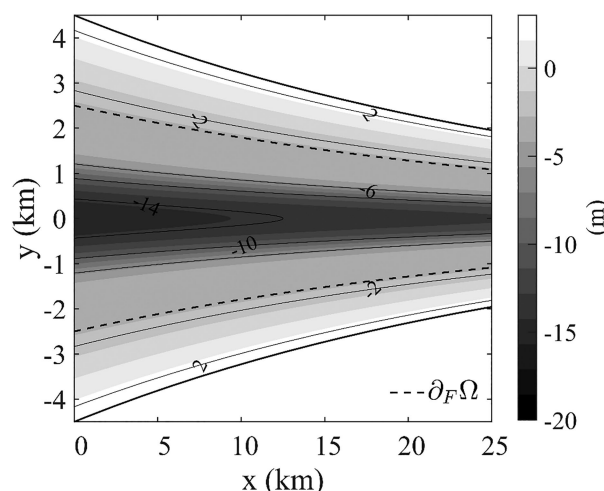


FIG. 2. Idealized geometry and bathymetry in the default estuary. The dashed lines denote the interface between intertidal and channel regions $\partial_F \Omega$.

TABLE 2. Default parameters for the idealized estuary.

Parameters	Description	Value	Unit
L	Estuarine length	25	km
B_0	Width of the channel region at the mouth	5	km
L_b	Estuarine convergence length	30	km
h_c^{\max}	Maximum channel depth	15	m
h_c^{\min}	Minimum channel depth	13	m
h_f	Depth at the side boundary $\partial_F \Omega$	3	m
k_c, k_s	Coefficients determining the lateral bathymetry profile	3, 0.8	
A_v	Vertical eddy viscosity	0.008	$\text{m}^2 \text{s}^{-1}$
s	Slip parameter in the channel region	0.005	m s^{-1}
s_f	Slip parameter in the intertidal region	0.002	m s^{-1}
$a_{M_2}^m$	M_2 tidal amplitude at the mouth	2	m
$a_{M_4}^m$	M_4 tidal amplitude at the mouth	0	m
$a_{M_0}^m$	M_0 tidal amplitude at the mouth	0	m
R	Total river discharge at the head	20	$\text{m}^3 \text{s}^{-1}$
S_m	Salinity at the mouth	31	psu
x_c, x_l	Length parameters of the salinity profile	40, 20	km
r_B	Width ratio between the intertidal and channel regions	0.4	

$$S(x, y) = 0.5S_m \left(1 - \tanh \frac{x - x_c}{x_l} \right). \quad (51)$$

Here, S_m is the salinity at the seaward boundary and x_c and x_l are length parameters that describe the salinity profile. The parameter settings for the default experiment are given in Table 2.

Including intertidal areas in an estuary can increase its tidal prism. Neglecting the minor variations in the M_2 tidal amplitude along the short estuary, the tidal prism without intertidal regions is $\int_0^L 2a_{M_2} B dx$, while the increased tidal prism associated with intertidal areas is $\int_0^L 2a_{M_2} B_f dx$. This means that the inclusion of intertidal habitats leads to an increase in the tidal prism by a factor of $r_B = B_f/B$. This corresponds to a 40% increase in the tidal prism of the default system.

2) SENSITIVITY EXPERIMENTS

Besides the default experiment (hereafter referred to as scenario I), five sensitivity experiments are conducted to investigate how intertidal habitat width (scenario II), intertidal habitat position (scenarios III and IV), estuary convergence (scenario V), and estuary length (scenario VI) affect the coupled tidal water motion (Table 3). In scenario II, the width of intertidal areas is halved by reducing r_B to 0.2. In scenarios III and IV, intertidal areas are located only in the lower ($0 \leq x \leq L/2$) and upper ($L/2 \leq x \leq L$) estuaries, respectively. In scenario V, a stronger estuary convergence is considered by decreasing L_b to

5 km, typical of short, convergent systems like the Blackwater Estuary (Wei et al. 2021). In scenario VI, the estuary length is increased to 150 km, typical of long, convergent systems like the Humber Estuary (Townend and Whitehead 2003).

In all scenarios, the bathymetry and salinity distributions remain the same, as defined by Eqs. (48) and (51). The only exception is that, in the long estuary experiment (with $L = 150$ km), the water depth at the thalweg ($y = 0$) decreases from 15 m at the mouth to 3 m at the head [Eq. (49b)], while the salinity decreases from 31 psu at the mouth to nearly 0 at the head [Eq. (51)]. The maximum longitudinal gradient of salinity in this experiment is -0.8 psu km^{-1} in the lower estuary. The model domain in the sensitivity experiments is extended 20 km seaward, similar to the default scenario.

In the sensitivity study, we run two experiments in each scenario, i.e., with ($r_B \neq 0$, see Table 3) and without (by setting $r_B = 0$) intertidal habitats. To investigate the impact of reclamation or restoration/creation of intertidal habitats on the hydrodynamics in the whole estuary, the contribution of intertidal habitats to the channel water motion is derived by comparing the results in each of these experiments with intertidal habitats to those without intertidal habitats. In experiments with and without intertidal habitats, all boundary conditions and estuary parameters of the channel region, including the bathymetry and geometry, are identical. The same periodic tidal forcing and constant total river discharge are prescribed, in both experiments, at the seaward and landward boundaries, respectively.

TABLE 3. Overview of model scenarios with intertidal habitats.

No.	Scenarios	L (km)	L_b (km)	r_B	Intertidal position
I	Default experiment	25	30	0.4	$0 \leq x \leq L$
II	Smaller intertidal width	25	30	0.2	$0 \leq x \leq L$
III	Lower-reach intertidal area	25	30	0.4	$0 \leq x \leq L/2$
IV	Upper-reach intertidal area	25	30	0.4	$L/2 \leq x \leq L$
V	Stronger estuary convergence	25	5	0.4	$0 \leq x \leq L$
VI	Larger estuary length	150	30	0.4	$0 \leq x \leq L$

The major difference between the two experiments is the lateral water exchange, which is zero (i.e., $F_n = 0$) when excluding intertidal habitats (i.e., $r_B = 0$, vertical closed walls at $\partial_F \Omega$).

c. Model validation

To test the capability of the semianalytical model in reproducing estuarine hydrodynamics in both the channel and intertidal domains after inclusion of intertidal habitats, the semianalytical model results in the default experiment are compared with the results obtained from a state-of-the-art numerical model using Delft3D (Deltare 2021). All forcing conditions and estuary parameter settings are the same in two models except that quadratic bottom friction is used in the numerical model, whereas the semianalytical model assumes linear bottom friction. The quadratic bottom friction coefficients in the numerical model are determined by requiring energy dissipation within the intertidal and channel regions during a tidal cycle to be the same in both numerical and semianalytical models. Detailed descriptions of the model validation can be found in [appendix D, section a](#).

d. Tidal asymmetry decomposition

To quantify effects of intertidal habitats on tidal asymmetry, we use three tidal asymmetry indicators: tidal duration asymmetry γ_{TDA} , slack water asymmetry γ_{SWA} , and peak current asymmetry γ_{PCA} (de Swart and Zimmerman 2009; Gong et al. 2016; Guo et al. 2018, 2019), which are given by

$$\gamma(\chi) = \frac{\frac{1}{N_\chi - 1} \sum_{i=1}^{N_\chi} (\chi_i - \langle \chi \rangle)^3}{\left[\frac{1}{N_\chi - 1} \sum_{i=1}^{N_\chi} (\chi_i - \langle \chi \rangle)^2 \right]^{3/2}} = \begin{cases} \gamma_{\text{TDA}}, & \chi = \partial_t \eta, \\ \gamma_{\text{SWA}}, & \chi = \partial_t u, \\ \gamma_{\text{PCA}}, & \chi = u. \end{cases} \quad (52)$$

Here, χ_i represents the time series of tidal signals (i.e., $\partial_t \eta$, $\partial_t u$, u), $\langle \chi \rangle$ is the mean value of the signals, and N_χ is the number of time series. Here, γ_{TDA} measures the duration asymmetry of the rising and falling tides, γ_{SWA} measures the slack duration asymmetry of the high and low water, and γ_{PCA} measures the asymmetry of the peak flood and ebb currents. Positive skewness values mean flood dominance and vice versa. The skewness γ_{SWA} and γ_{PCA} are important to the transport of fine and coarse sediments, respectively (Dronkers 1986; Nidzieko and Ralston 2012).

The skewness is calculated based on each harmonic tidal constituent [see Nidzieko (2010) for a detailed derivation]. For simplicity, only the M_2 , M_4 , and M_0 components are considered when computing the skewness in our study. Based on Eqs. (45) and (46), these skewness indicators can be further separated into contributions associated with different processes that drive the M_2 , M_0 , and M_4 tidal water motions (detailed in [appendix E](#)).

3. Results

The performance of the semianalytical model in reproducing estuarine water motions in the channel and intertidal domains

is demonstrated in [section 3a](#). The impact of intertidal habitats on estuarine hydrodynamics is quantified in [section 3b](#). The dominant physical processes of the intertidal effects are discussed for the default experiment in [section 3c](#). The sensitivities of the intertidal effects to the intertidal habitat width, intertidal habitat position, estuary convergence, and estuary length, as well as their controlling processes, are investigated in [section 3d](#).

a. Semianalytical model performance

To demonstrate the performance of the extended semianalytical model, the simulated M_2 , M_4 , and M_0 current velocities in the channel and intertidal regions and the water exchange between both regions are compared with those obtained from the Delft3D model and the semianalytical model of Kumar et al. (2017), respectively.

1) CHANNEL WATER MOTION

The numerically simulated tidal and residual water motion in the channel region is qualitatively well reproduced by the extended semianalytical model ([Fig. 3](#), comparing the left and middle columns).

The spatial distributions of the depth-averaged tidal current at the M_2 and M_4 tidal frequency in the extended semianalytical model with intertidal habitats are highly consistent with the numerical results. In both models, the longitudinal M_2 tidal current is stronger in the channel than on the shoals and maximizes (up to 1.2 m s^{-1}) at the mouth ([Figs. 3a,b](#)), while the lateral current velocity is stronger on the shoals than in the channel and peaks (up to 0.12 m s^{-1}) at the mouth ([Figs. 3d,e](#)). The longitudinal M_4 tidal current also shows similar spatial patterns and magnitudes in both models, with the strongest current of more than 0.1 m s^{-1} at the regions between the channel and shoals and in the lower-estuary channel ([Figs. 3g,h](#)).

Spatial patterns of the depth-averaged residual circulation in the numerical model and the extended semianalytical model are also consistent ([Figs. 3j,k](#)). In the lower estuary ($x = 0\text{--}10 \text{ km}$), there is a strong inflow (up to 0.15 m s^{-1}) at the regions between the channel and shoals with a weaker outflow elsewhere. In the upper estuary, there is an inflow ($\sim 0.06 \text{ m s}^{-1}$) in the channel and outflow ($\sim 0.06 \text{ m s}^{-1}$) on the shoals. The extended semianalytical model overestimates the residual inflow speed by $\sim 0.05 \text{ m s}^{-1}$ at the regions between the channel and shoals when compared to the numerical model. The cross-sectional distribution of velocities at each tidal frequency in the extended semianalytical model also agrees well with that in the numerical model (see [Fig. D1](#) in [appendix D](#)).

When compared to the semianalytical model of Kumar et al. (2016, 2017) where no intertidal habitats are considered, the extended semianalytical model with intertidal habitats exhibits superior performance in reproducing the numerically simulated M_2 , M_4 , and M_0 tidal dynamics in the channel region. Neglecting interactions between the intertidal and channel waters results in significantly underestimated M_2 tidal currents. By excluding the intertidal area in the semianalytical model, the maximum longitudinal current is decreased from

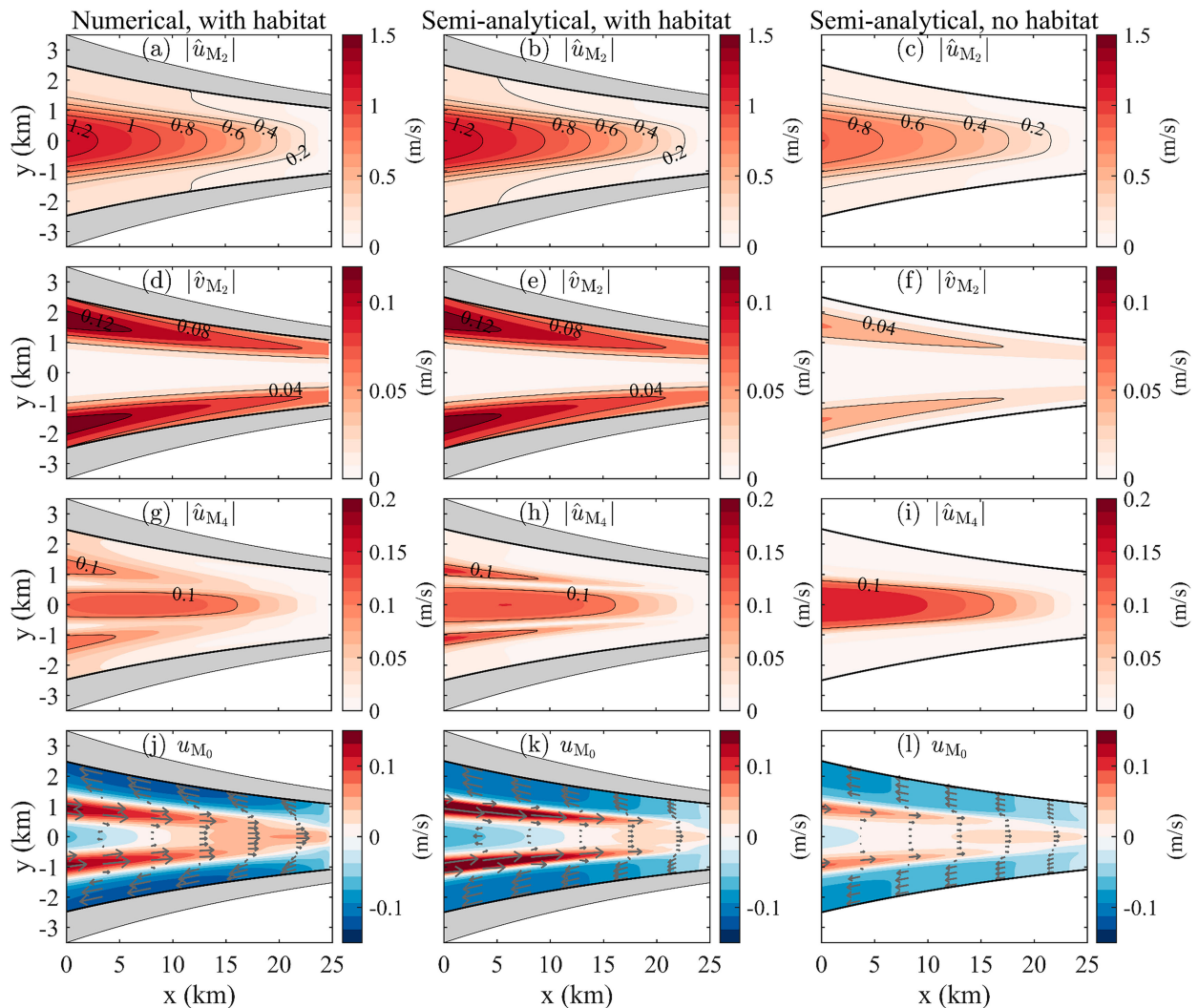


FIG. 3. Depth-averaged tidal and residual velocity obtained from (left) the numerical model with intertidal habitats, (middle) the semi-analytical model with intertidal habitats extended in this study, and (right) the semianalytical model without intertidal habitats as used by Kumar et al. (2017) at the (a)–(f) M_2 , (g)–(i) M_4 , and (j)–(l) M_0 tidal frequencies, respectively. Arrows denote the horizontal velocity vector. Gray areas represent the intertidal regions.

1.2 to 0.8 m s^{-1} in the channel near the mouth, and the maximum lateral current decreased from 0.12 to 0.04 m s^{-1} on the shoals near the mouth (Figs. 3c,f). The horizontal patterns of the M_4 current and residual circulation without considering intertidal habitat effects also differ greatly from the numerical results (Figs. 3i,l). In the absence of intertidal habitats, strong M_4 tidal currents occur in the channel with a maximum amplitude of $\sim 0.15 \text{ m s}^{-1}$ in the lower estuary. The residual circulation shows a depth-averaged inflow (up to $\sim 0.05 \text{ m s}^{-1}$) in the channel and outflow (up to $\sim 0.06 \text{ m s}^{-1}$) on the shoals.

2) INTERTIDAL WATER MOTION

The magnitude and along-estuary variability of the longitudinal velocity averaged over the intertidal cross section calculated by the extended semianalytical model are also in good

agreement with the numerical results (Fig. 4). In both models, the M_2 intertidal flow velocity decreases its magnitude from $\sim 0.15 \text{ m s}^{-1}$ at the estuary mouth to zero at the estuary head (see Fig. 4, black lines). The M_4 intertidal velocity in the two models has similar magnitudes (up to 0.03 m s^{-1}) which decreases to zero near the estuary head (see Fig. 4, blue lines). The residual current in the intertidal region is directed seaward in both models, which decreases from $\sim 0.05 \text{ m s}^{-1}$ at the mouth to zero at the head (see Fig. 4, red lines).

3) WATER EXCHANGE BETWEEN THE INTERTIDAL AND CHANNEL REGIONS

As shown in Eq. (6), the interaction between the intertidal and channel waters is directly driven by the lateral water exchange F_n across the interface $\partial_F \Omega$. The amplitude and phase of the exchange calculated from the extended semianalytical

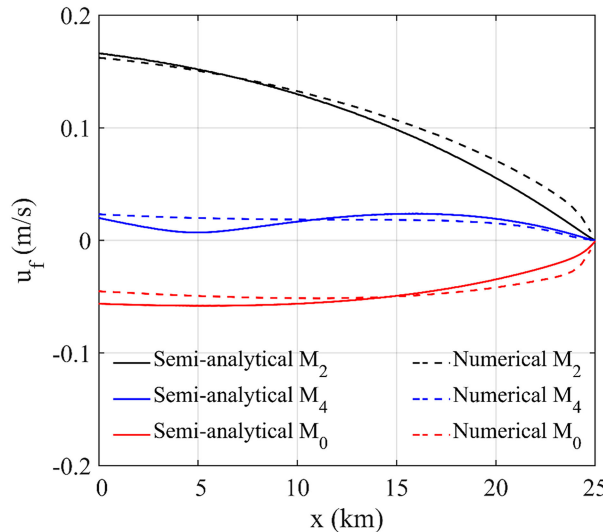


FIG. 4. Intertidal velocity u_f averaged over the intertidal cross section obtained from the semianalytical (solid lines) and numerical models (dashed lines). The current velocity u_f in the numerical model is calculated by averaging the 3D velocities over the intertidal cross section and then decomposing them into M_0 , M_2 , and M_4 tidal constituents.

model also align well with the numerical results (Fig. 5, comparing solid and dashed lines).

The semidiurnal water exchange per unit length ($F_{n_{M_2}}$) decreases from approximately $0.3 \text{ m}^2 \text{ s}^{-1}$ at the mouth to $0.15 \text{ m}^2 \text{ s}^{-1}$ at the head (Fig. 5a, black lines), and its phase increases from -88° at the mouth to 7° along the estuary (Fig. 5b, black lines). The semidiurnal water exchange is nearly 3 times as large as the quarter-diurnal exchange ($F_{n_{M_4}}$), the amplitude of which decreases from $\sim 0.1 \text{ m}^2 \text{ s}^{-1}$ at the mouth to

$0.05 \text{ m}^2 \text{ s}^{-1}$ at the head with its phase decreasing from -84° to -91° (Fig. 5b, blue lines). The residual water exchange ($F_{n_{M_0}}$) is less than $0.02 \text{ m}^2 \text{ s}^{-1}$ throughout the estuary (Fig. 5a, red lines).

b. Effects of intertidal habitats on the channel water motion

The influence of intertidal habitats on estuarine hydrodynamics is investigated by quantifying the differences in the water level $\Delta\eta$, current velocity Δu , and tidal asymmetry $\Delta\gamma$ in the channel region between scenarios with and without intertidal habitats. These differences ($\Delta\eta$, Δu , and $\Delta\gamma$) are calculated by subtracting the results in the experiment without considering intertidal habitats from those in the experiment with intertidal habitats.

1) SEMIDIURNAL TIDE

In the presence of intertidal habitats, the water exchange between the intertidal and channel regions leads to substantial alterations in the channel water motion. The tidal amplitude and phase along the estuary in the presence and absence of intertidal habitats are shown in Fig. 6. The M_2 tidal surface amplitude ($|\hat{\eta}_{M_2}|$) increases from 2 m at the estuary mouth to 2.27 m at the head, amplified by up to 0.27 m (Fig. 6a). When excluding the intertidal habitats, however, the M_2 tidal amplitude increases from 2 to 2.19 m with an amplification of less than 0.19 m. This indicates that intertidal habitats increase the tidal amplitude by up to 0.08 m in the idealized estuary. The larger M_2 tidal phases in the presence of intertidal habitats compared to those without intertidal habitats mean that these habitats only slightly slow down the M_2 tidal propagation (by up to $\sim 2^\circ$) throughout the idealized estuary (Fig. 6b).

The influence of intertidal habitats on the M_2 tidal and residual currents is shown in Fig. 7. The depth-averaged

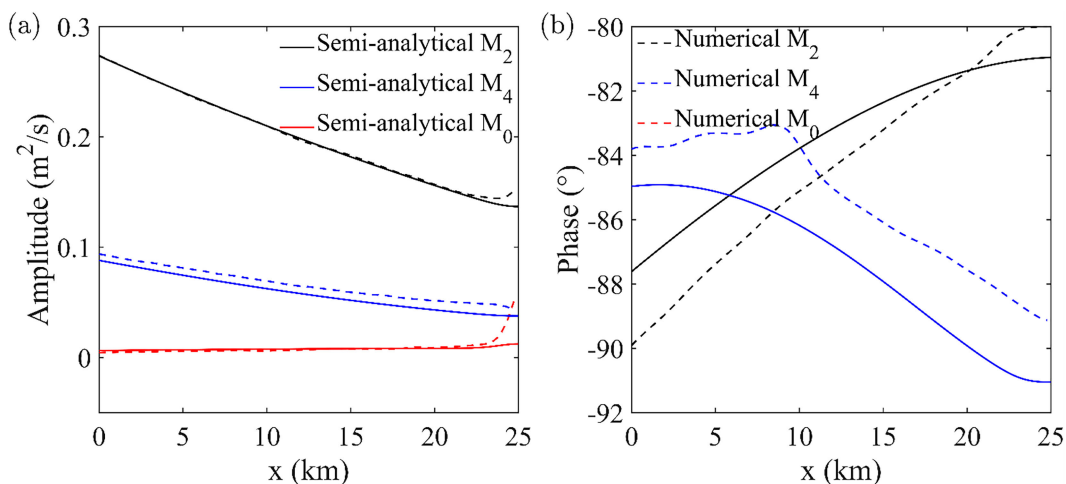


FIG. 5. (a) Amplitude and (b) phase of the water exchange F_n between intertidal and channel regions at the M_2 (black), M_4 (blue), and M_0 (red) tidal frequencies, obtained from the semianalytical (solid lines) and numerical models (dashed lines), respectively. The water exchange F_n in the numerical model is calculated by integrating the 3D velocities over the water depth at the interface $\partial_F\Omega$ and then decomposing them into M_0 , M_2 , and M_4 tidal constituents.

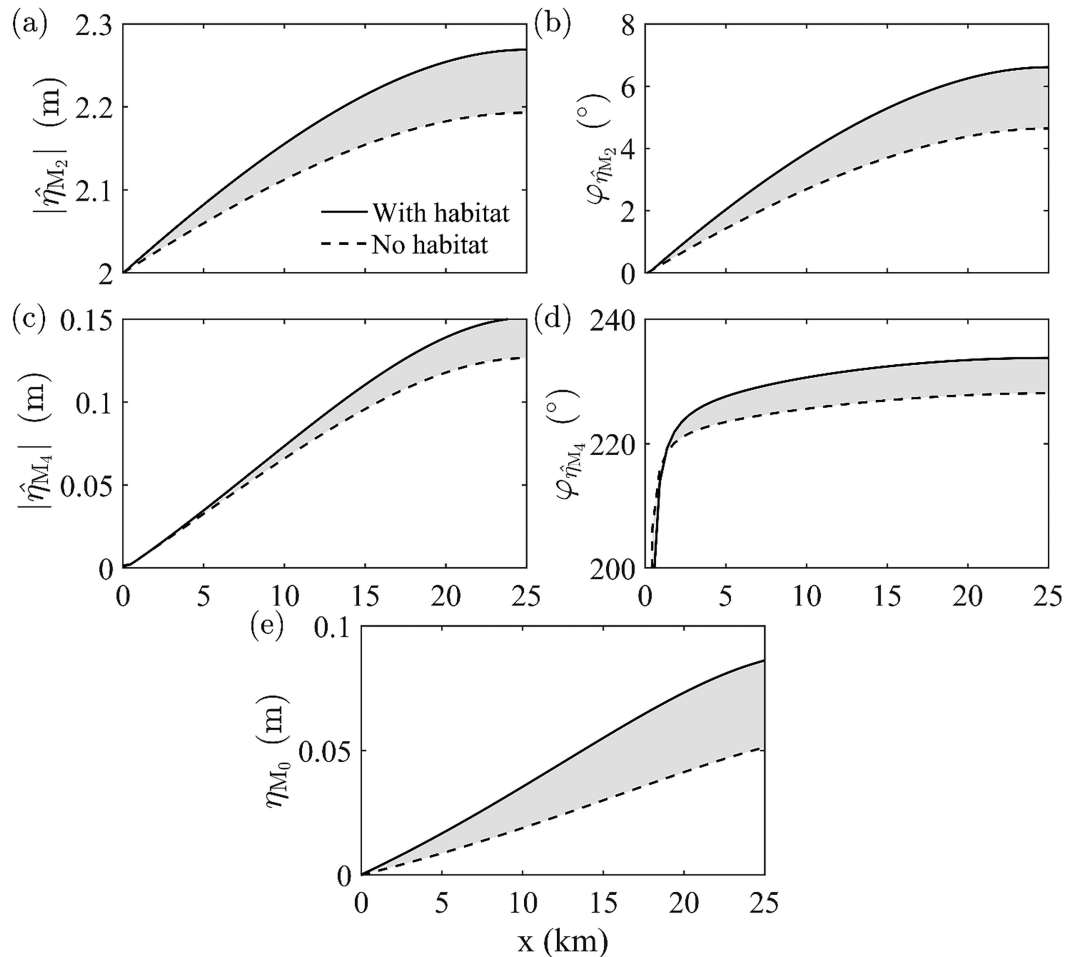


FIG. 6. Comparison of the tidal elevation along the estuary between scenarios with (solid lines) and without (dashed lines) intertidal habitats. (a)–(d) The width-averaged tidal amplitude and phase at the (first row) M_2 and (second row) M_4 tidal frequencies. (e) The width-averaged residual (M_0) water level.

longitudinal M_2 tidal current ($|\hat{u}_{M_2}|$) is strengthened by up to 0.35 m s^{-1} due to intertidal habitats (see Fig. 7a), and its phase is delayed by $\sim 3^\circ$ (Fig. 7b). The strongest lateral M_2 tidal current on the shoals is increased by 0.07 m s^{-1} after including intertidal habitats (Figs. 3e,f). The amplification and delay of the M_2 tide due to intertidal habitats align with previous numerical studies of the Taizhou Bay, China (Zhang et al. 2015, 2016); Darwin Harbor, Australia; and Xiangshan Bay, China (Li et al. 2012, 2018a).

2) QUARTER-DIURNAL TIDE

The quarter-diurnal tidal water motion is also strongly affected by intertidal habitats. The M_4 tidal amplitude $|\hat{\eta}_{M_4}|$ increases landward by up to 0.15 and 0.12 m with and without intertidal habitats, respectively (Fig. 6c). This means that the M_4 tide is amplified by up to 0.03 m. Its phase is delayed by $\sim 6^\circ$ due to intertidal habitats (Fig. 6d). The inclusion of intertidal habitats leads to an increase in the M_4 tidal velocity amplitude ($|\hat{u}_{M_4}|$) by up to 0.1 m s^{-1} at the lower-estuary regions between the channel and shoals and a decrease in $|\hat{u}_{M_4}|$ by

$\sim 0.05 \text{ m s}^{-1}$ in the channel (Fig. 7c). The M_4 tidal currents on the lower-estuary shoals are also slightly strengthened by intertidal habitats. These habitats also result in an increased phase of the M_4 tidal velocity by $\sim 10^\circ$ in the channel and more than 60° at the regions between the channel and shoals, together with a decreased phase by more than 60° on the shoals (see Fig. 7d). The impact of intertidal habitats on the M_4 tidal motion is also consistent with numerical investigation of the Xiangshan Bay (Li et al., 2018b).

3) RESIDUAL CIRCULATION

The intertidal habitats strongly modulate the residual water motions in the channel region. The residual sea surface elevation (η_{M_0}) increases landward by up to 0.09 and 0.05 m with and without intertidal habitats, respectively (Fig. 6e). This indicates that the residual water level is increased by $\sim 0.04 \text{ m}$ due to intertidal habitats. Moreover, intertidal habitats have a pronounced impact on both the spatial pattern and strength of the residual circulation (see Figs. 3k,l). The inclusion of intertidal habitats results in an increase in the outflow on the

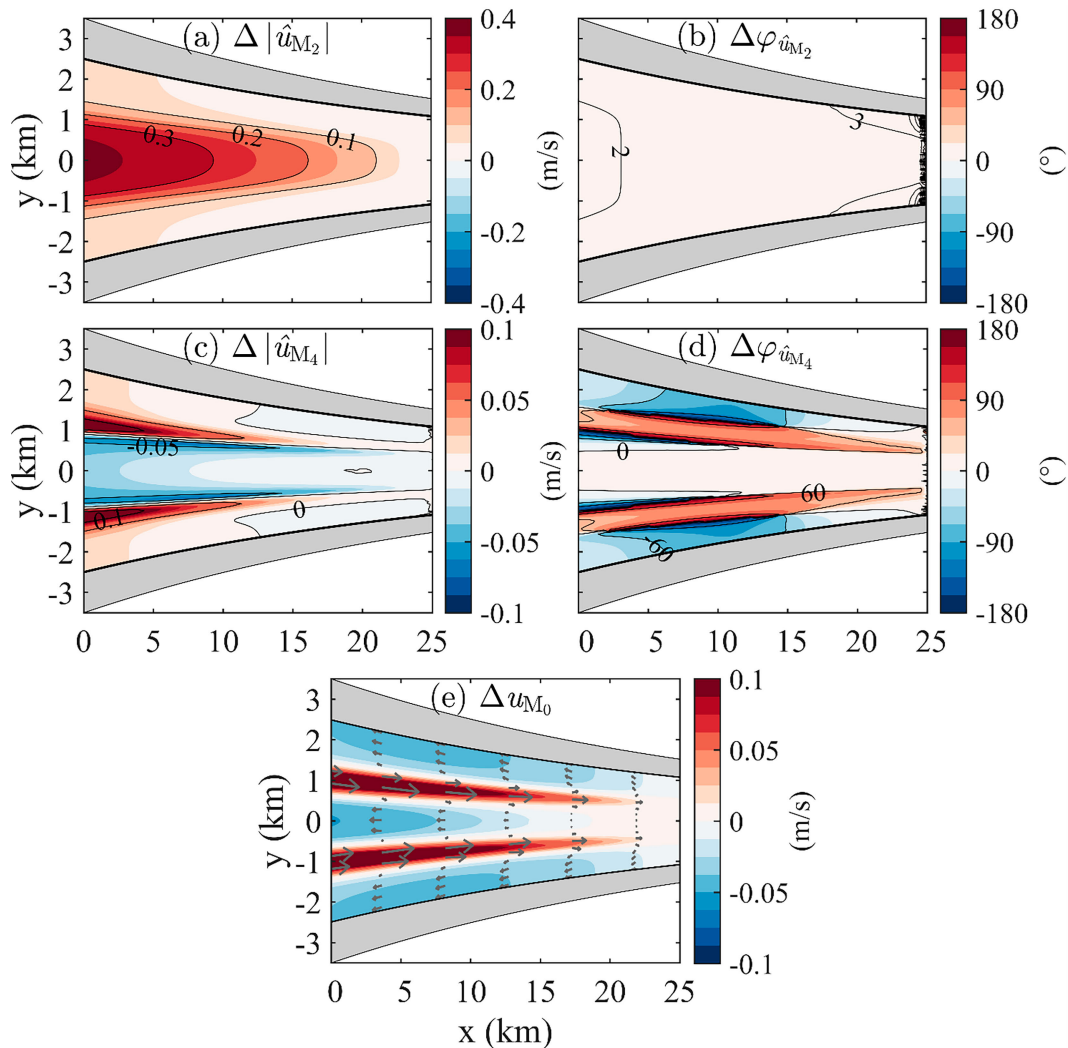


FIG. 7. (a)–(d) Differences in the amplitude and phase of the depth-averaged velocity at the (first row) M_2 and (second row) M_4 tidal frequencies between experiments with and without intertidal habitats. (e) Difference in the depth-averaged residual circulation between experiments with and without intertidal habitats.

shoals (by up to $\sim 0.03 \text{ m s}^{-1}$) and in the channel (by up to 0.05 m s^{-1}) and an increase in the inflow at the regions between the channel and shoals by up to 0.15 m s^{-1} (Fig. 7e).

4) TIDAL ASYMMETRY

The impact of intertidal habitats on tidal asymmetry is assessed by comparing the three skewness indicators [see Eq. (52)] between experiments with and without intertidal habitats (Fig. 8). The skewness γ_{TDA} is positive in both experiments, indicating flood dominance with shorter rising tides than falling tides. In both scenarios, γ_{TDA} increases landward, as also found in the Huangmaohai Estuary, China (Gong et al. 2016). This means that the duration of rising tides decreases landward (Figs. 8a,b). By including intertidal habitats, γ_{TDA} is slightly increased in the upper estuary with prolonged falling tides (Fig. 8c).

In the absence of intertidal habitats, the skewness γ_{SWA} is mainly positive with a longer high-water slack (i.e., flood

dominance) except at the lower-estuary regions between the channel and shoals (Fig. 8d). Including intertidal habitats results in a substantially decreased skewness γ_{SWA} throughout the estuary, indicating enhanced ebb dominance or reduced flood dominance (Figs. 8e,f). This finding is in agreement with the model results for Newport Bay, the United States (Guo et al. 2018).

The skewness γ_{PCA} shows a similar spatial pattern to that of the depth-averaged residual circulation in experiments with and without intertidal habitats (see Figs. 8g,h and 3k,l), highlighting the importance of residual circulation to the tidal asymmetry in peak current velocity. Without intertidal habitats, the skewness γ_{PCA} is negative on the shoals (i.e., ebb dominance, with a larger peak ebb velocity than peak flood velocity) and positive in most of the channel (i.e., flood dominance, with a larger peak flood velocity). In the presence of intertidal habitats, however, the skewness γ_{PCA} becomes

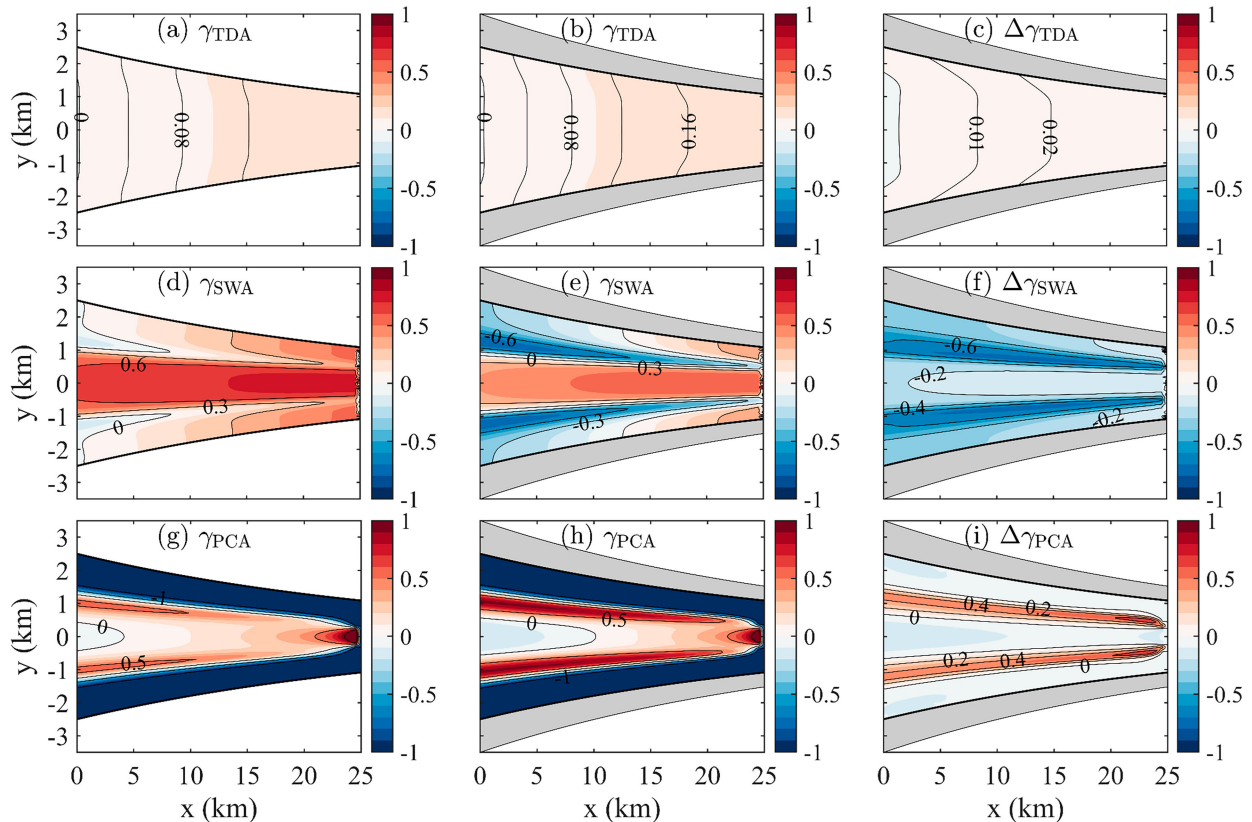


FIG. 8. Horizontal distribution of the three tidal skewness indicators (first row) γ_{TDA} , (second row) γ_{SWA} , and (third row) γ_{PCA} in the experiments (middle) with and (left) without intertidal habitats, and (right) the differences in these indicators between both the experiments.

negative in the lower-estuary channel ($x = 0-10$ km) and positive near the regions between the channel and shoals. This suggests that the intertidal habitats weaken the flood dominance in the channel [see also in Guo et al. (2018)] and significantly strengthen the flood dominance near the regions between the channel and shoals (Fig. 8i). The ebb dominance on the shoals is also enhanced by intertidal habitats.

c. Controlling physical processes of the channel water motion

The influence of intertidal habitats on the dominant processes that control the M_2 , M_4 , and M_0 tidal water motion as well as tidal asymmetry in the channel region is discussed in this section.

1) M_2 TIDAL WATER MOTION

The enhanced predominant M_2 tidal oscillations $|\hat{\eta}_{M_2}|$ due to intertidal habitats can be explained by the resonance/reflection characteristics of the tidal wave propagation in short estuaries. As reviewed by Talke and Jay (2020), decreasing water depth in short estuaries (with lengths less than a quarter of the tidal wavelength) leads to tidal amplification by bringing these systems closer to the quarter-wave resonance condition. Since the idealized estuary considered in the default experiment is typical

of short systems ($L = 25$ km, much less than a quarter of the frictionless M_2 tidal wavelength, approximately 400 km, based on a mean depth of ~ 10 m), the reduced cross-sectionally averaged water depth, resulting from the inclusion of intertidal habitats, leads to enhanced M_2 tidal oscillations (see more discussion in section 4a). Moreover, the tidal prism is enlarged by $\sim 40\%$ due to the presence of intertidal habitats, which significantly enhances the M_2 tidal currents ($|\hat{u}_{M_2}|$) in the idealized estuary considered here (Stark et al. 2017; Mahavadi et al. 2024). The importance of the increased tidal prism to the intertidal effects on estuarine dynamics is detailed in appendix D, section b.

2) M_4 TIDAL WATER MOTION

As shown in Eq. (46), the first-order M_4 tidal motion is driven by various processes. Due to the inclusion of intertidal habitats, the enhanced leading-order M_2 tidal currents greatly strengthen the first-order M_4 (and M_0) water motions associated with several nonlinear processes including AC, TRFSD, and NS (i.e., indirect effect). The direct effects of the nonzero M_4 (and M_0) water exchange F_n on these processes are much weaker due to the small magnitude of F_n at the first order (Fig. 5a).

The contributions of each process to the depth-averaged M_4 tidal current in experiments with and without intertidal habitats are shown in Fig. 9. When excluding intertidal habitats,

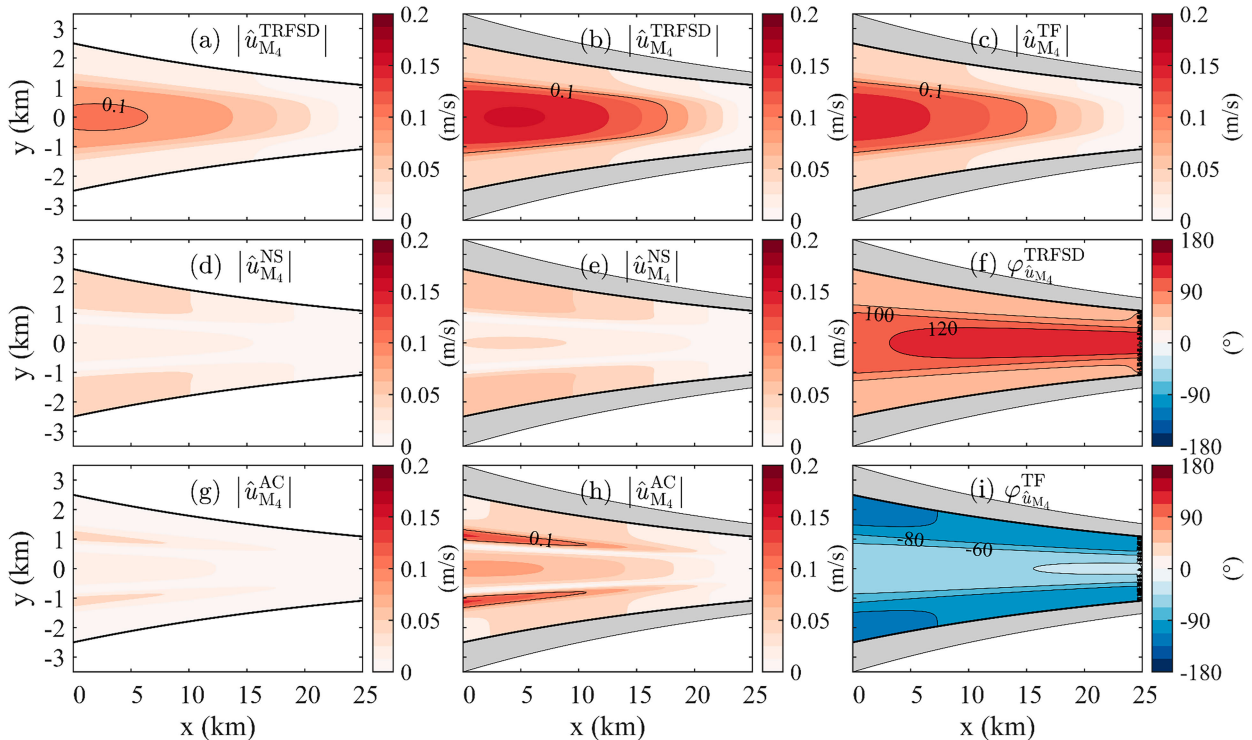


FIG. 9. Amplitude of the depth-averaged longitudinal M_4 tidal velocity driven by (a),(b) TRFSD, (d),(e) NS, and (g),(h) AC (left) with-out and (middle) with intertidal habitats, respectively. (c) The TF-induced M_4 current with intertidal habitats, which becomes zero when excluding these habitats. (f),(i) The phase of the M_4 tidal current driven by TRFSD and TF with intertidal habitats.

the M_4 tidal motion is dominated by TRFSD (up to 0.1 m s^{-1} ; Fig. 9a), while contributions of other processes are minor (Figs. 9d,g). After including the intertidal habitats, the amplified M_2 tidal currents substantially increases the M_4 tidal contribution associated with AC, TRFSD, and NS (Figs. 9b,e,h). The TRFSD ($\sim 0.15 \text{ m s}^{-1}$) also dominates the generation of the M_4 tide in the presence of intertidal habitats (see Fig. 9b). However, inclusion of intertidal habitats results in a strong TF-induced M_4 tidal current (up to 0.15 m s^{-1} ; Fig. 9c). This current is nearly out of phase with that induced by TRFSD (Figs. 9f,i). Hence, intertidal habitat leads to dampened M_4 tidal motion in the channel (see Fig. 7c). However, the augmented M_4 tidal current associated with AC and NS results in a strengthened M_4 tidal current at the lower-estuary regions between the channel and shoals and on the lower-estuary shoals (Figs. 9d,e,g,h), respectively.

3) RESIDUAL WATER MOTION

Since the residual (M_0) water exchange between the channel and intertidal regions is close to zero (see Fig. 5a), the residual current due to the residual lateral water exchange (TF) is negligible (not shown here). Nevertheless, the amplified M_2 tidal currents caused by intertidal habitats strongly affects the residual circulation and the dominant physical processes controlling the residual circulation.

When excluding intertidal habitats, the residual circulation is dominated by AC (up to 0.10 m s^{-1}), which features an

inflow at the regions between the channel and shoals and outflow elsewhere (Fig. 10c), and NS (up to 0.05 m s^{-1}) characterized by an inflow in the channel and outflow on the shoals (Fig. 10e). The residual flow due to GC and TRFSD shows a similar pattern to NS but with a smaller magnitude (see Figs. 10a,g). After including intertidal habitats, the AC-induced residual circulation is significantly strengthened (by up to 0.10 m s^{-1}) and surpasses all the other processes (see Fig. 10d), dominating the changes in the total residual circulation (Fig. 7e). The residual flow due to NS is also enhanced (Fig. 10f), contributing to the strengthened outflow on the shoals (Fig. 7e). The residual flow due to GC and TRFSD is almost unchanged by intertidal habitats (Figs. 10b,h). The large influence of intertidal habitats on the residual circulation through AC is consistent with Zheng et al. (2003).

4) TIDAL ASYMMETRY

The skewness indicators γ_{TDA} and γ_{SWA} are determined by the M_2 and M_4 tidal components only, whereas γ_{PCA} is also affected by the residual circulation [see Eqs. (E1)–(E3)]. Contributions of dominant processes to these indicators are shown in Fig. 11. The M_4 tidal elevation due to TRFSD ($\eta_{M_4}^{\text{TRFSD}}$) associated with the amplified M_2 tide in the presence of intertidal habitats leads to an increased γ_{TDA} (Fig. 11b). The TF-induced M_4 tidal motion ($\eta_{M_4}^{\text{TF}}$ and $U_{M_4}^{\text{TF}}$), however, results in a decreased γ_{TDA} and γ_{SWA} throughout the estuary (Figs. 11a,c). The AC-induced M_4 tidal current ($U_{M_4}^{\text{AC}}$) enhanced

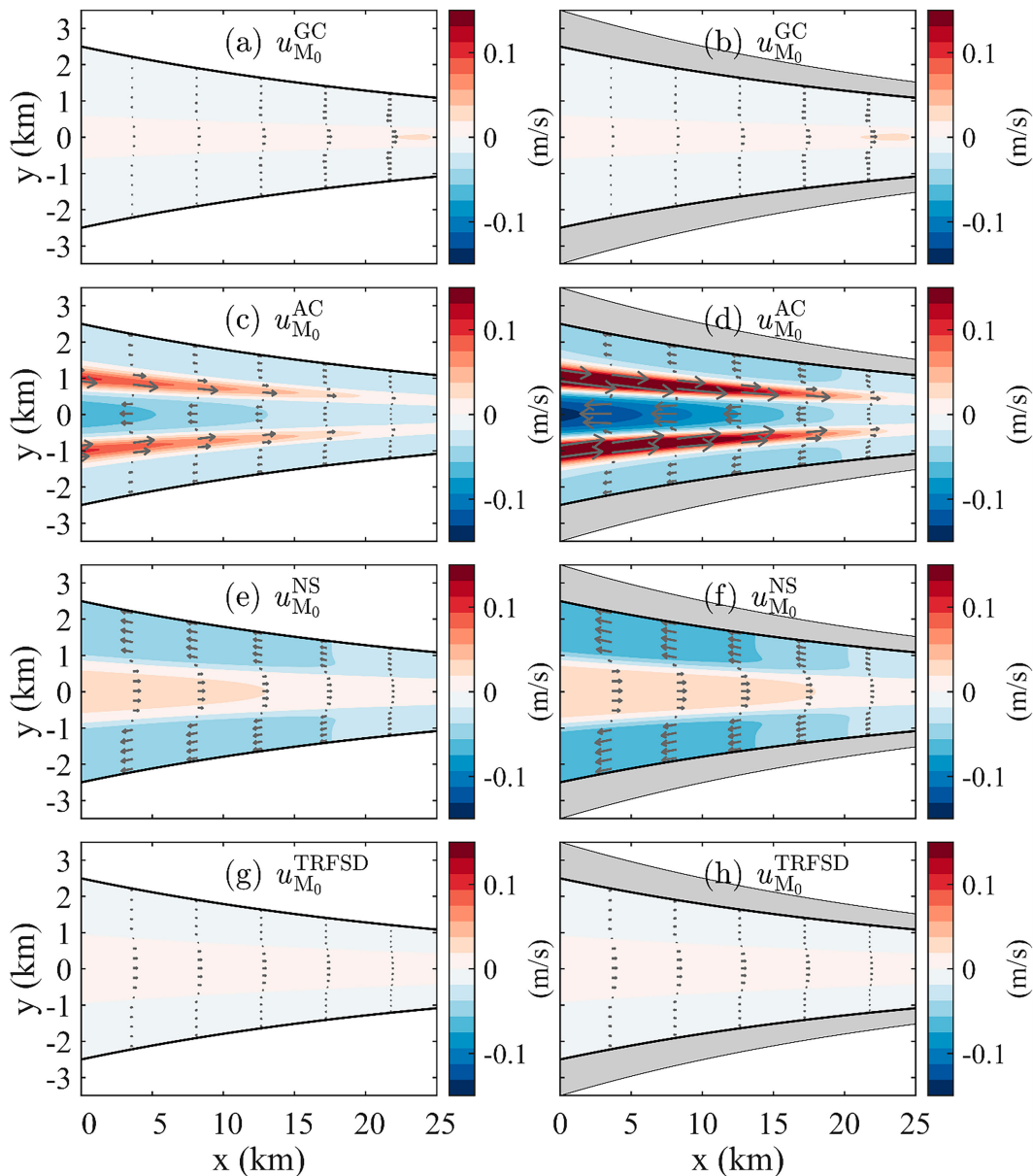


FIG. 10. The depth-averaged residual (M_0) circulation driven by (a),(b) GC, (c),(d) AC, (e),(f) NS, and (g),(h) TRFSD (left) without and (right) with of intertidal habitats, respectively.

by intertidal habitats also contributes to a decreased γ_{SWA} at the regions between the channel and shoals (Fig. 11d). The intertidal effects on the skewness γ_{PCA} are controlled by the strengthened residual current due to AC ($U_{M_0}^{AC}$, Fig. 11f). The skewness γ_{PCA} due to the M_4 tidal current induced by TF is substantially negative (Fig. 11e). These results show that the TF process reduces the values of all three skewness indicators and promotes ebb dominance of the channel water motion.

d. Sensitivity analysis

To investigate the sensitivity of the intertidal effects on estuarine hydrodynamics to the characteristics of intertidal

habitats and estuary geometry, we analyze the intertidal effects on the sea surface elevation (Fig. 12), tidal currents (Fig. 13), and tidal asymmetry (Fig. 14) in the channel domain in five additional sensitivity experiments (Table 3). These experiments consider a smaller intertidal habitat width (scenario II), intertidal habitats covering only the lower reach (scenario III) or the upper reach (scenario IV), a stronger width convergence (scenario V), and a larger estuary length (scenario VI), with and without intertidal habitats, respectively. Since the results of channel water motions without intertidal habitats for scenarios I–IV have been analyzed in Figs. 3 and 6, the no-habitat results of water level and tidal currents in more

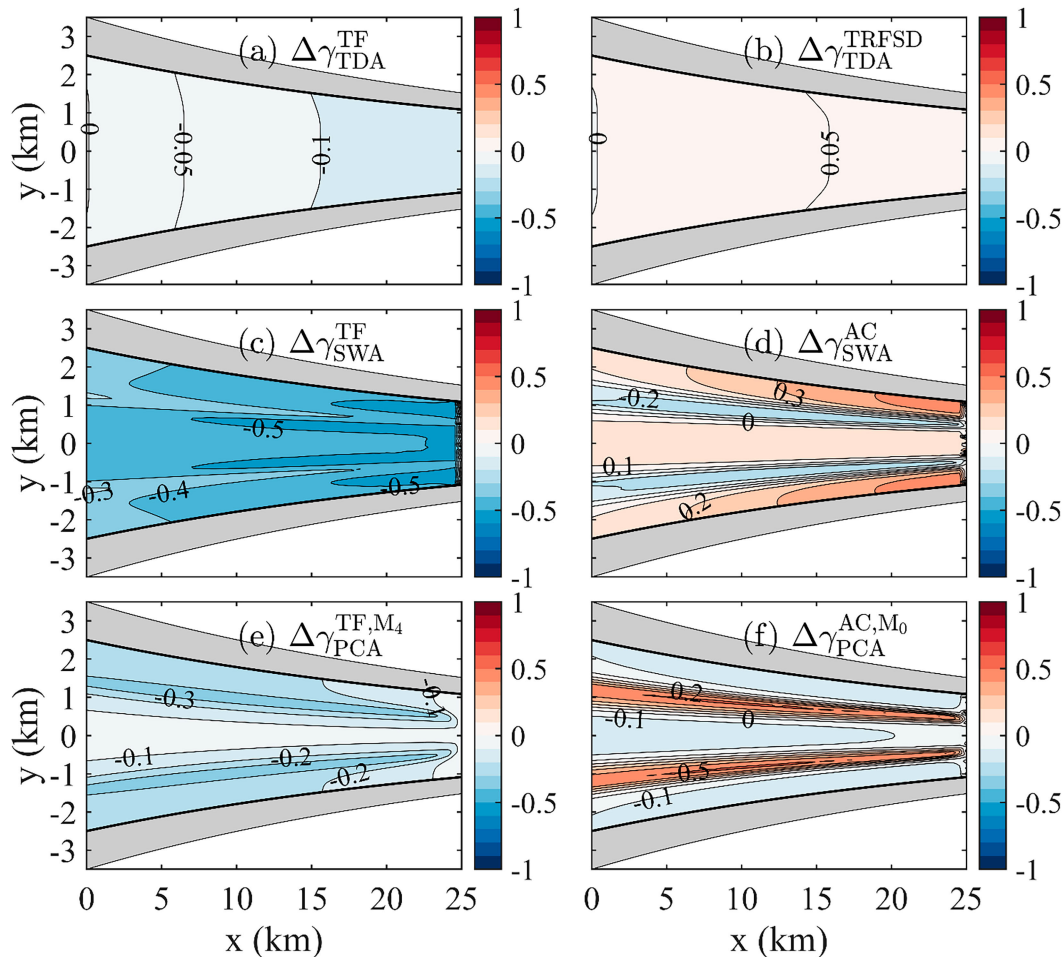


FIG. 11. Intertidal effects on γ_{TDA} due to M_4 tidal elevation driven by (a) TF and (b) TRFSD, on γ_{SWA} due to M_4 tidal currents driven by (c) TF and (d) AC, and on γ_{PCA} due to (e) M_4 tidal current driven by TF and (f) M_0 residual circulation driven by AC, respectively.

convergent (scenario V) and long-estuary (scenario VI) experiments are shown in Figs. F1 and F2, respectively (see appendix F).

1) INTERTIDAL HABITAT WIDTH

Reducing the ratio r_B from 0.4 to 0.2 (scenario II) halves the width of the intertidal region. As a result, the intertidal effects on the amplitude of the M_2 and M_4 tidal elevation and currents, as well as the M_0 surface elevation and residual circulation, are approximately halved (see Figs. 12 and 13a–c). This reduces the intertidal effect on γ_{SWA} by 30%–50% (see Figs. 14a and 8f) and reduces the intertidal effect on γ_{PCA} by half (see Figs. 14b and 8i). Since $\Delta\gamma_{TDA}$ is small in all scenarios (e.g., see Fig. 8c), its sensitivity is not discussed hereafter.

Halving the width of intertidal regions decreases the water exchange by half [because $F_n \propto B_f$, see Eq. (10)], which correspondingly weakens the intertidal effects on the M_2 tidal amplitude by half [see also in Li et al. (2018b), Speer and Aubrey (1985)]. Also, the intertidal effects due to all nonlinear processes are approximately halved (see Figs. 15a–c),

resulting in halved intertidal effects on the total M_4 tidal motion, M_0 residual circulation, and also the tidal asymmetry (see Figs. E1a–c).

2) INTERTIDAL HABITAT POSITION

Including intertidal habitats only in the lower estuary (scenario III) or the upper estuary (scenario IV) results in substantially different water motion in the channel region. The intertidal effects on the sea surface elevation, flow velocities, and tidal skewness indicators in scenario I, where intertidal habitats are distributed throughout the entire estuary, are roughly equivalent to the combined intertidal effects observed in experiments with intertidal habitats located in both the lower (scenario IV) and upper (scenario V) estuaries.

Similar to the default experiment (scenario I), inclusion of intertidal habitats in the upper or lower estuary results in an amplified M_2 tide along the estuary (see Fig. 12a) by up to 0.06 or 0.02 m, respectively. The lower-estuary intertidal habitats cause an increased M_4 tidal amplitude (by ~ 0.02 m), while the upper-estuary habitats induce a decreased M_4 tidal

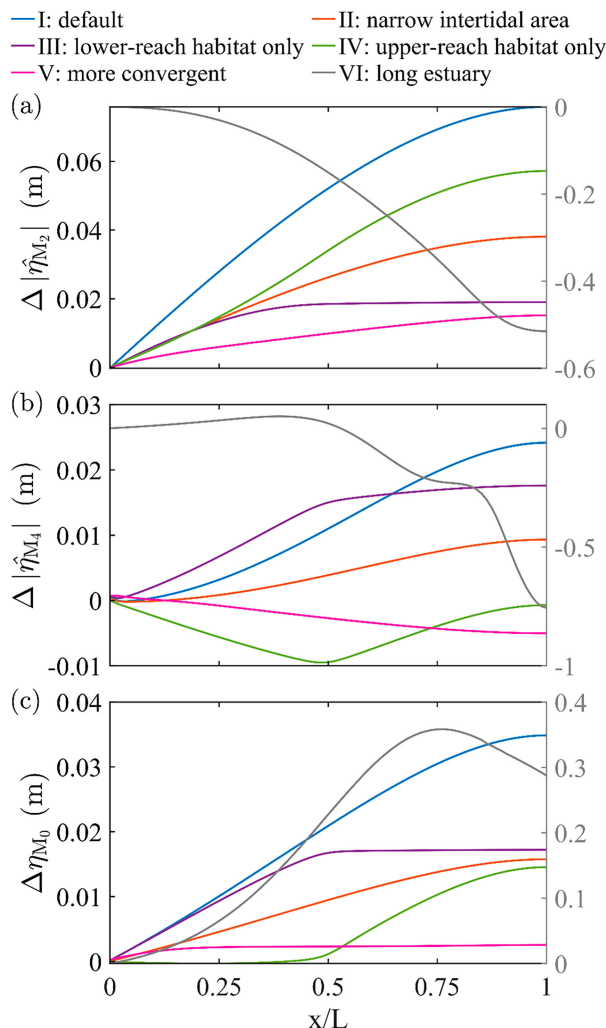


FIG. 12. The intertidal effects on the sea surface amplitude at the (a) M_2 , (b) M_4 , and (c) M_0 tidal frequencies, in the default experiment (scenario I; blue lines), experiment with a smaller intertidal width (scenario II; orange lines), experiment with intertidal habitats located partially in the lower (scenario III; purple lines) or upper (scenario IV; green lines) estuary, experiment with a stronger estuary convergence (scenario V; pink lines), and experiment with a larger estuary length (scenario VI; gray lines), respectively. Note that the gray y axis on the right is utilized for the long-estuary scenario only.

amplitude (by ~ 0.01 m, see Fig. 12b). The residual sea surface is increased by ~ 0.02 m by the lower-estuary or upper-estuary habitats (see Fig. 12c).

Patterns of the effects of the lower-estuary or upper-estuary habitats on tidal/residual currents and tidal skewness are similar to those in the default experiment. It is interesting to note that intertidal habitats in the lower estuary only affects the flow velocities and tidal skewness indicators in the lower estuary, without affecting them in the upper estuary (Figs. 13d–f and 14c,d). Including intertidal habitats in the upper estuary, however, modulates the water motion and tidal asymmetry throughout the estuary (Figs. 13g–i and 14e,f). Moreover, the

strength of these effects is of the same magnitude in both scenarios, even though intertidal width of the upper-estuary habitats is smaller than that in the lower part. This means that compared to the lower-estuary habitats, the upper-estuary habitats can induce an even larger effect on tidal velocities and tidal asymmetries if considering the same intertidal width (hence a larger r_B due to estuary convergence), according to the sensitivity of intertidal effects to r_B derived in section 3d(1). This implies that the strength of intertidal effects on estuarine hydrodynamics is determined by the width ratio between intertidal and channel regions instead of the intertidal width, as noted by Jay (1991), Hepkema et al. (2018), and Winterwerp and Wang (2013). The dominant processes controlling the intertidal effects of upper-estuary or lower-estuary habitats on the tidal/residual currents and tidal asymmetries are similar to those in the default experiment (see Figs. 15d–i and E1d–i).

3) ESTUARY CONVERGENCE

By reducing the estuarine convergence length L_b from 30 to 5 km in scenario V, the estuarine hydrodynamics is strongly modulated by the weakened tidal water motions (see Fig. F1, pink lines, and Figs. F2a–c). This can be explained by the characteristics of the tidal wave resonance in the estuary. In short systems ($L = 25$ km), a decrease in L_b makes the systems move farther from the resonance condition (i.e., the quarter-wave resonance), hence leading to a weakened predominant M_2 tidal current (Talke and Jay 2020). As a result, the nonlinear processes (e.g., TRFSD, TF, AC, see Figs. 15j–l) are substantially weakened, yielding a weakened M_4 tidal and residual water motions. The intertidal effects on sea surface elevation, tidal/residual currents, and tidal asymmetries are also weakened substantially.

When considering a strong width convergence, the presence of intertidal habitats only slightly modifies the tidal elevation at each frequency, with the M_2 tide amplified, M_4 tide dampened, and M_0 sea surface increased by less than 0.02 m (Fig. 12). The M_2 tidal currents are enhanced by less than 0.1 m s^{-1} throughout the estuary (Fig. 13j). The M_4 tidal currents are enhanced by up to 0.03 m s^{-1} on the lower-estuary shoals and weakened by less than 0.02 m s^{-1} elsewhere (Fig. 13k). The landward residual circulation is strengthened by up to 0.03 m s^{-1} at the lower-estuary regions between the channel and shoals (Fig. 13l). The intertidal effects on tidal current, residual circulation, and tidal asymmetries (Figs. 14g,h) in estuaries with a stronger width convergence show patterns similar to those in the default experiment, with their dominant processes shown in Figs. 15j–l and E1j–l.

4) ESTUARY LENGTH

Increasing the estuary length L from 25 to 150 km (scenario VI) substantially enhances the tidal water motions (see Fig. F1, gray lines, and Figs. F2d–f). This can be explained by the wave resonance characteristics in estuaries considered in this study. Increasing L in short estuaries moves the system closer to the resonance condition (Talke and Jay 2020), hence significantly enhancing the predominant M_2 tidal currents

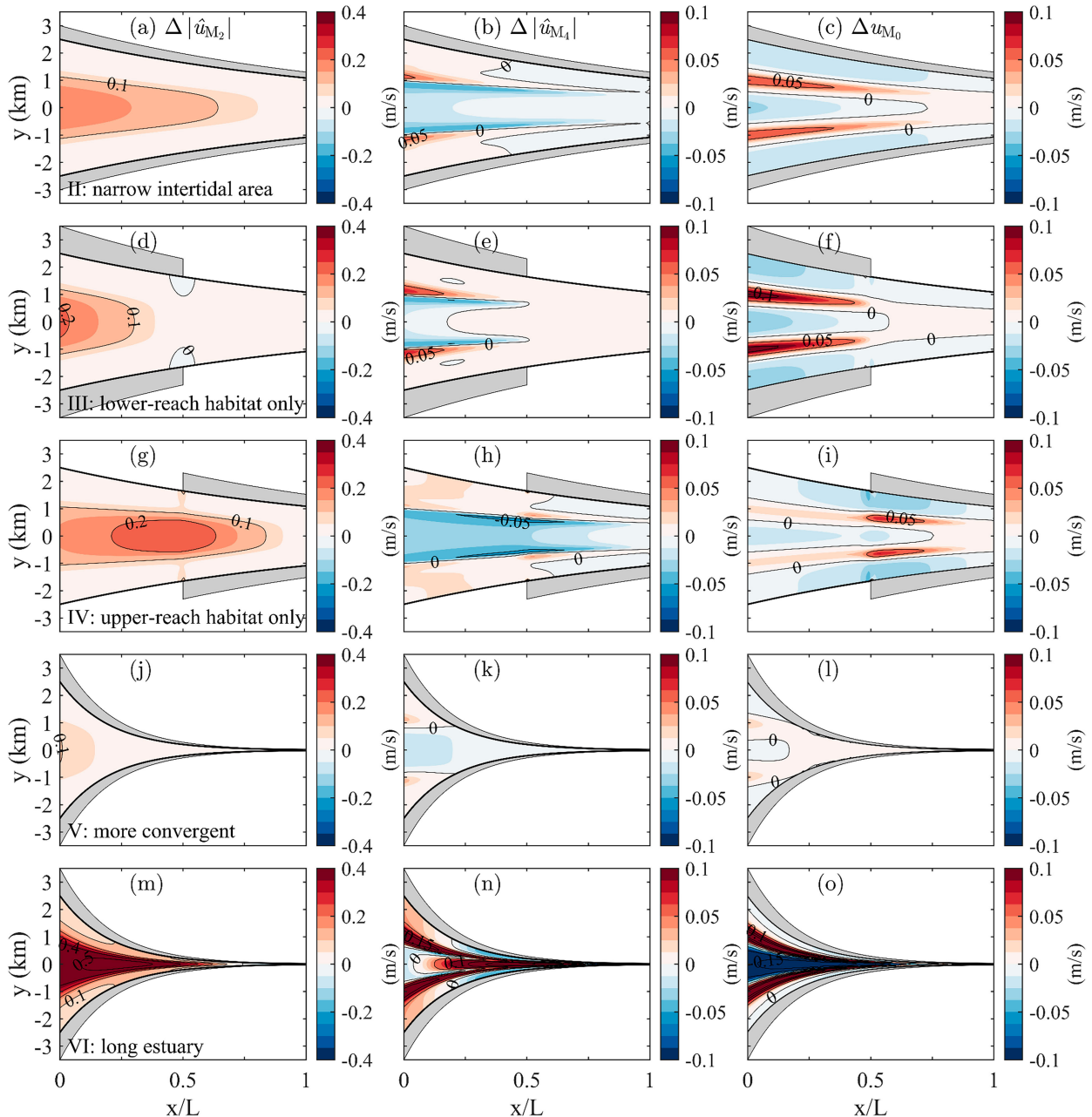


FIG. 13. The intertidal effects on the depth-averaged velocity amplitude at the (left) M_2 , (middle) M_4 , and (right) M_0 tidal frequencies in scenarios (first row) II, (second row) III, (third row) IV, (fourth row) V, and (fifth row) VI, respectively.

together with the first-order M_4 and M_0 currents driven by the nonlinear processes (e.g., TRFSD, TF, AC, see Figs. 15m–o). This is also emphasized by Wei et al. (2022) in their sensitivity studies on tidal and residual currents to L .

The intertidal effects on estuarine hydrodynamics are also augmented substantially by increasing L . Contrary to all the other experiments, the intertidal habitats in the long system ($L = 150$ km) significantly dampen the predominant M_2 tide by up to 0.5 m (Fig. 12a). This can be understood as the reduced water depth due to the inclusion of intertidal habitats

moves the system farther from the resonance condition in the long estuary (Talke and Jay 2020). This indicates intertidal effects on tidal wave propagation strongly depend on estuary length due to distinct resonance/reflection characteristics of tidal wave propagation in short and long estuaries. Due to the presence of intertidal habitats, the M_4 tide is amplified by up to 0.05 m in the lower estuary and damped by more than 0.5 m in the upper estuary (Fig. 12b). The residual sea surface is increased by up to 0.4 m in the upper estuary (Fig. 12c).

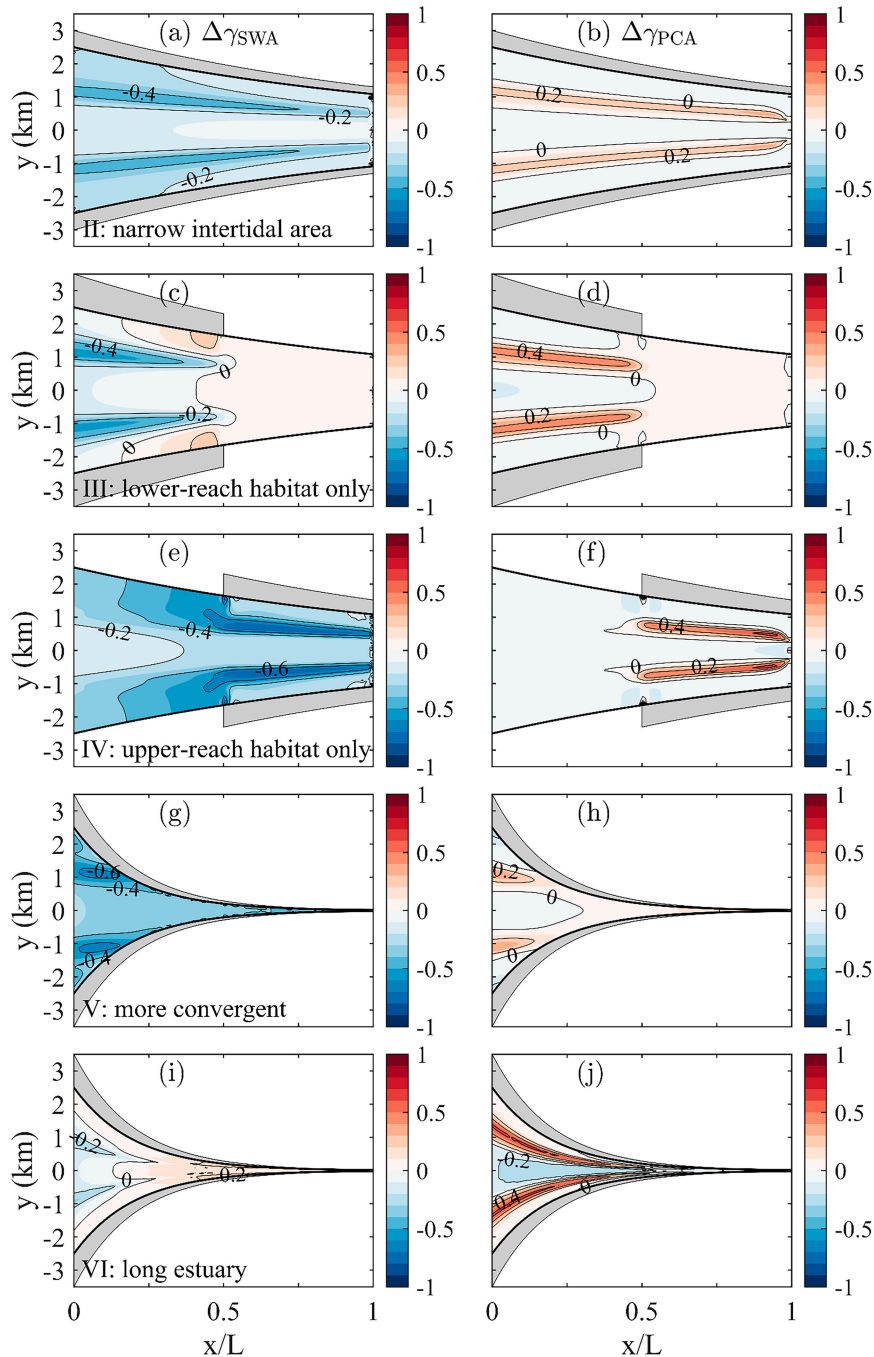


FIG. 14. The intertidal effects on the tidal skewness indicators (left) γ_{SWA} and (right) γ_{PCA} in scenarios (first row) II, (second row) III, (third row) IV, (fourth row) V, and (fifth row) VI, respectively.

With the enhanced tidal water motions in the long estuary, the intertidal habitats strengthen the M_2 tidal currents by up to 0.5 m s^{-1} throughout the estuary (Fig. 13m). This is due to the enlarged tidal prism as found in the Scheldt Estuary (Stark et al. 2017), despite the dampened M_2 tidal oscillations. The M_4 tidal currents are strongly enhanced in the midestuary

channel and at the lower-estuary shoals by more than 0.2 m s^{-1} (Fig. 13n). This is dominated by the enhanced nonlinear process TRFSD (Fig. 15m) together with AC and NS (not shown here). The M_4 tidal currents are weakened elsewhere by more than 0.2 m s^{-1} especially in the upper estuary (Fig. 13n) due to the counteracting effects of the TF-induced M_4 tidal current

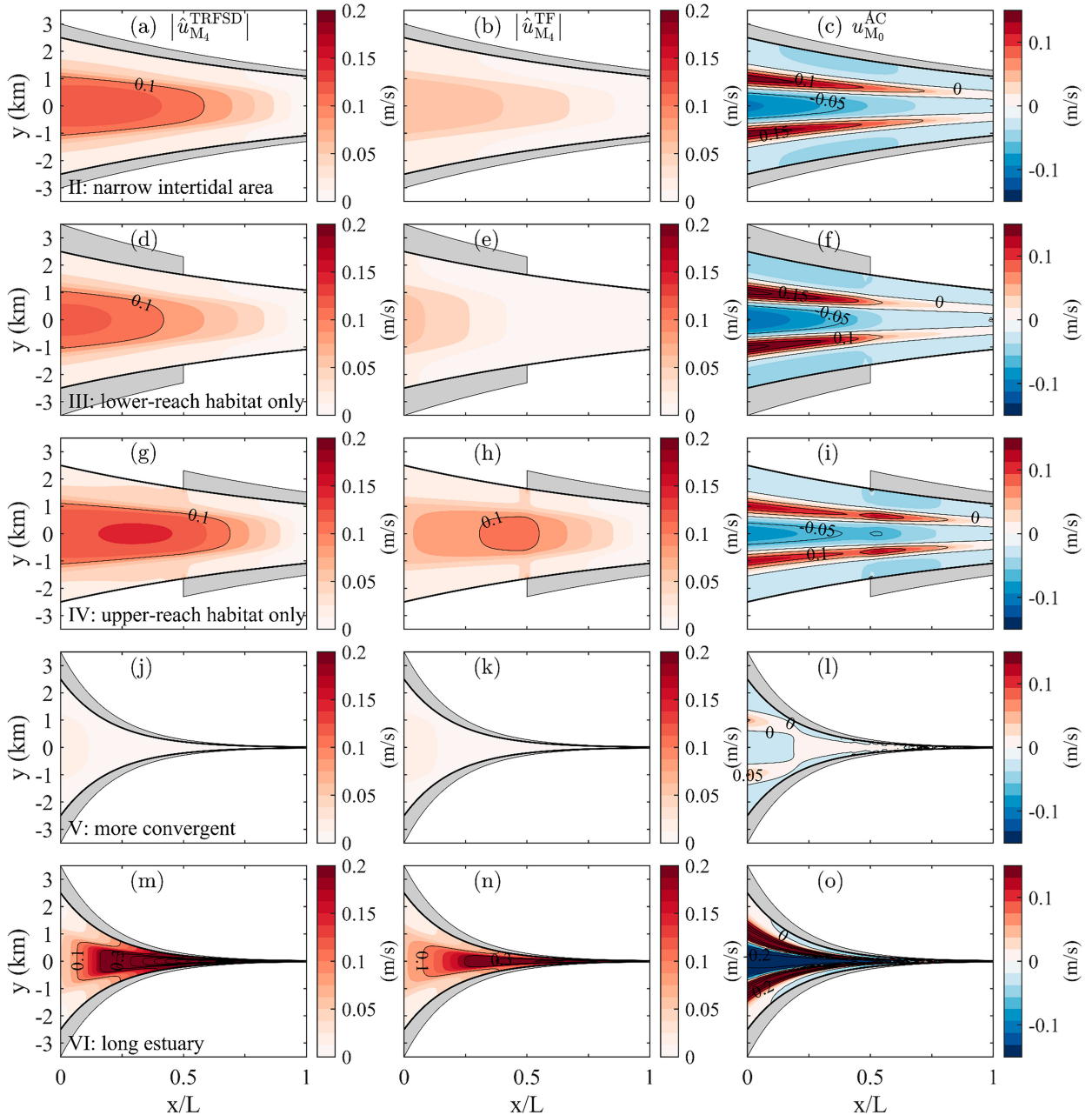


FIG. 15. Depth-averaged M_4 tidal velocity due to (left) TRFSD and (middle) TF, along with depth-averaged residual circulation due to (right) AC in the presence of intertidal habitats in scenarios (first row) II, (second row) III, (third row) IV, and (fourth row) V, respectively.

(Fig. 15n) on the TRFSD-induced M_4 tidal current as mentioned above. The intertidal habitats considerably strengthen the residual circulation by up to 0.2 m s^{-1} , dominated by the significantly enhanced AC in the long estuary (Fig. 15o).

Different from the other experiments where intertidal habitats lead to a decreased γ_{SWA} throughout the estuary, these habitats in long estuaries only decrease γ_{SWA} in the lower-estuary channel and increase it elsewhere (Fig. 14j). This is driven by the TF-induced M_4 tidal current (Fig. E1m) together with the AC-induced M_4 tidal current (Fig. E1n)

enhanced by the inclusion of intertidal habitats. The intertidal effect on γ_{PCA} shows similar patterns to those in the default experiment (Fig. 14j), which is dominated by the AC-induced residual circulation enhanced by intertidal habitats (Fig. E1o).

4. Discussion

a. Implications of the intertidal–channel interactions

Our results reveal that intertidal habitats can strongly modulate estuarine hydrodynamics in tidally dominated, well-mixed

estuaries. This has strong implications for the estuarine material transport and water quality. For instance, the strengthened lateral circulations near the channel shoulders, driven by the strongly amplified tidal rectification in the presence of intertidal habitats, can contribute significantly to the channel–shoal sediment exchange and potentially affect morphological evolution in both channel and intertidal regions (McSweeney et al. 2016). Besides, the different responses of the M_2 , M_4 , and residual water motion to the intertidal habitats mean that the relative importance of different physical processes controlling the estuarine material transport can be strongly affected by intertidal habitats. As literature shows, by reducing the mean water depth, intertidal habitats can amplify the predominant (e.g., M_2) tide in short estuaries [e.g., Darwin Harbor (Li et al. 2012), Xiangshan Bay (Li et al. 2018a)], with $L < \sim 50$ km] and dampen the tide in long [e.g., Scheldt Estuary (Stark et al. 2017), Satilla River Estuary (Zheng et al. 2003), Delaware Bay (Lee et al. 2017), with $L > \sim 100$ km] estuaries. However, intertidal habitats always enhance the predominant tidal currents in these estuaries due to the enlarged tidal prism by including intertidal water storage areas (Zheng et al. 2003; Li et al. 2017, 2014; Stark et al. 2017). These habitats also tend to strengthen the residual circulation and increase the lateral variability in the depth-averaged residual currents (see Fig. 3). This implies that the presence of these habitats may strengthen the salt/sediment transport caused by the M_2 tidal advection and residual circulation (Wei et al. 2016, 2018; Li et al. 2014).

The strong sensitivity of estuarine dynamics to the position of intertidal habitats revealed in this study means that reclaiming/restoring intertidal habitats at different longitudinal locations can have substantially different impacts on estuarine dynamics. In particular, the pronounced impact of upper-estuary intertidal habitats on the lower reach implies that losses of upper-estuary habitats can significantly influence the dynamics throughout the estuary. Thus, it is crucial to account for the broader effects of localized intertidal habitat changes on the entire estuary during the design phase of reclamation or restoration projects.

More importantly, the intertidal effects on tidal dynamics significantly vary with estuary length and width convergence, implying that the role of intertidal regions can differ greatly from estuary to estuary. The sensitivity of intertidal effects on the dominant tidal propagation to the estuary length suggests that climate mitigation measures (e.g., intertidal habitat restorations) may trigger undesired effects in short estuaries (i.e., increased tidal range and aggravated flood risks). In long systems with weak convergence, however, these measures may effectively dampen tides and thereby have larger flood mitigation potential. Meanwhile, climate change and human activities like the construction of physical barriers (e.g., sluice gates, weirs) have significantly altered these estuarine characteristics (Talke and Jay 2020), potentially leading to additional shifts in intertidal effects on estuarine hydrodynamics and the dominant controlling processes. For example, the steepening/narrowing of these habitats, caused by either sea level rise or land reclamation, can weaken residual circulation and reduce the dominance of advection in the total residual circulation. This highlights the importance of understanding how intertidal

effects on tidal dynamics respond to changes in estuarine characteristics (e.g., length, convergence) and forcing conditions, particularly in the context of potential restoration and creation of intertidal regions for climate mitigation.

A comprehensive understanding of the impact of intertidal habitats on the channel water motion and its dominant mechanisms derived from this study also offers valuable insights into how various climate mitigation measures could potentially affect estuarine water quality, morphology, and primary production (Dronkers 2016; Liu and de Swart 2015; Talke et al. 2009; Zhu et al. 2021).

b. Model limitations and unresolved processes

Our study systematically investigates the impact of intertidal habitats on the tidal and residual water motions in tidally dominated, well-mixed estuaries. However, it is important to recognize the constraints inherent in the semianalytical approach employed in our study, which relies on specific simplifications and assumptions detailed in section 2.

The semianalytical model is tailored for tidally dominated, well-mixed or weakly stratified estuaries with a small river discharge, where the salinity and vertical eddy viscosity are prescribed to be vertically homogenous and time independent. This means that the model diagnostically resolves gravitational circulation and disregards the interaction between tides, asymmetric tidal turbulence, residual circulation, and salt intrusion. However, tidal variations in the vertical eddy viscosity and diffusivity, driven by temporal changes in vertical shear, stratification, and water depth, can strongly affect residual circulation and salt transport (Wei et al. 2021). Another limitation lies in the linearization of bottom friction, which allows for the examination of distinct processes but may lead to an overestimation of residual circulation and overtides (Fig. 3).

There are several other unresolved processes in our model. For example, the hydrodynamics in the intertidal region is described using one-dimensional shallow-water equations, neglecting the influence of lateral variations in intertidal parameters/variables, such as bottom friction, sea surface gradient, and velocity on interactions between intertidal and channel waters. This might contribute to the observed differences in the intertidal velocities between the numerical and extended semianalytical models (Fig. 4). Also, our idealized model assumes a linear intertidal bed profile, yet in real estuaries, the profile can be concave up or convex up (Friedrichs 2011). This implies that the intertidal effects derived in this study might be either underestimated or overestimated due to the simplified representation of intertidal bathymetry. In estuaries considered in this study, the intertidal habitats affect the tidal and residual water motions mostly through changing the total estuarine tidal prism (appendix D, section b). However, since both the mean water depth and tidal prism are altered after including intertidal habitats, the individual impacts of intertidal habitats on estuarine water motion through modulating the mean water depth, tidal prism, or nonzero water exchange cannot be explicitly isolated in our results.

Last but not least, the sensitivity analysis in our study may yield different results when considering a different set of

estuary parameters (e.g., geometry, bathymetry, and bottom friction) (Alebrege et al. 2013; Friedrichs and Aubrey 1994; Li et al. 2016). For example, the strength of bed friction and the rate of topographic convergence determine tidal properties in estuaries predominantly (Jay 1991), which causes tides to be dampened by intertidal habitats in frictionally dominated systems but amplified by these habitats in less frictional estuaries (Li et al. 2016). A steeper channel–shoal bathymetric structure can lead to tidal amplification (Ensing et al. 2015) and reinforce intertidal effects through the increased water exchange resulting from enhanced tidal motions and lateral currents (Zhou et al. 2020). Also, by focusing on exponentially converging estuaries in our experiments, the intertidal effects on estuarine circulation in small estuaries with strong channel curvature (Tao and Zhu 2022) are not considered. Finally, Coriolis effects are found to be minor in this study (not shown), but they can lead to strong secondary circulation and interactions between intertidal and channel waters in larger, wider estuaries (Huijts et al. 2006). A more comprehensive understanding of the impact of intertidal habitats on estuarine dynamics necessitates the exploration of a broader range of parameter space in future studies.

5. Conclusions

In this study, we extended a three-dimensional semianalytical model to investigate the influence of intertidal habitats on estuarine hydrodynamics in tidally dominated, well-mixed estuaries, with a particular focus on the interaction between intertidal and channel waters. The results obtained from our extended semianalytical model were compared with those from a numerical Delft3D model, demonstrating a good reproduction of tidal and residual water motion in both the channel and intertidal regions.

By comparing the tidal and residual water motions between estuaries with and without intertidal habitats, we found that intertidal habitats can notably affect estuarine hydrodynamics. In the short estuary considered in our default experiment, intertidal habitats amplify and delay the predominant M_2 tides and currents, leading to a significantly strengthened M_4 and M_0 water motion as a result of enhanced nonlinear processes such as tidal rectification (AC) and tidal return flow (TRFSD). Lateral water exchange between the intertidal and channel regions results in a new M_4 and M_0 contribution (TF). The TF-induced M_4 tidal current dampens the total M_4 tidal motion in the channel because it is out of phase with the dominant M_4 contributions. Elsewhere, intertidal habitats enhance the M_4 tidal current due to the increased contributions of AC and the shear-free surface condition (NS). The residual circulation is dominated by AC and NS in the absence of intertidal habitats, with an inflow in the channel and outflow on the shoals. Inclusion of intertidal habitats considerably shifts the pattern and strength of the residual circulation due to the strengthened AC, resulting in a strong inflow at the regions between the channel and shoals and outflow in the channel.

Intertidal habitats strongly affect tidal asymmetry due to their impact on the M_2 , M_0 , and M_4 tidal motions. The TF-induced

M_4 tidal motion results in an increased duration of low water slack and an increased peak ebb velocity, thereby promoting ebb dominance throughout the estuary. Meanwhile, the enhanced AC due to intertidal habitats increases the peak flood velocity and promotes flood-dominant peak current at the regions between the channel and shoals. In the channel and on the shoals, however, AC tends to promote ebb dominance in the peak current.

The influence exerted by intertidal habitats is sensitive to the characteristics of intertidal habitats and estuaries. By halving the intertidal habitat width, the intertidal effects on the water motion, tidal asymmetry, and water exchange between intertidal and channel regions are halved. Relocating intertidal habitats from the lower estuary to the upper estuary brings about substantial alterations in the channel water motion. Lower-estuary intertidal habitats primarily affect only the lower reach surrounded by these habitats, while the effects of the upper-estuary habitats are considerable throughout the estuary. By increasing the estuary width convergence rate, the abovementioned intertidal effects are substantially weakened. More importantly, the roles of intertidal habitats on tidal dynamics strongly vary with the estuary length. By increasing the estuary length, the intertidal habitat leads to damping of the predominant M_2 tide and strengthened M_2 tidal currents in long estuaries, where intertidal effects become much stronger than those in short estuaries.

Our study reveals the complex interactions between intertidal and channel hydrodynamics, highlighting the potential importance of intertidal habitats to estuarine material transport. The strong sensitivity of intertidal effects to intertidal and estuarine characteristics suggests that future intertidal habitat changes can significantly influence the estuarine ecosystems and their responses to climate change and human interventions.

Acknowledgments. We acknowledge funding from the Key Laboratory of Ministry of Education for Coastal Disaster and Protection (J202201). This work is also supported by the National Natural Science Foundation of China (NSFC; U2040203), the Fundamental Research Funds for the Central Universities (B240205032), the U.K. Natural Environment Research Council (CHAMFER project, NE/W004992/1), the China Scholarship Council (CSC; File 202406710099), and State Key Laboratory of Water Disaster Prevention (2024491011). X. W. also acknowledges support from the Royal Society International Exchanges 2022 Cost Share (IEC\NSFC\223066). We acknowledge the constructive comments from Henk M. Schuttelaars and two anonymous reviewers, which have substantially improved our paper.

Data availability statement. All data used in this paper are available on Zenodo (<https://doi.org/10.5281/zenodo.8250051>).

APPENDIX A

Governing Equations of Intertidal Water Motion

The three-dimensional shallow-water motion equations [Eqs. (1)–(3)] are first used to describe the 3D intertidal

dynamics, where η and $\mathbf{U} = (u, v, w)$ also represent the 3D intertidal sea surface elevation and velocities. Then, the one-dimensional governing equations for the water motion in the intertidal regions are derived by averaging the three-dimensional shallow-water equations over the intertidal cross section.

As a first step, the continuity and momentum equations integrated from $z = -h$ to $z = \eta$ are derived. Then, these equations are integrated from the interface $(\partial_F \Omega)$ $y = B/2$ to the time-varying shoreline $y = B_t/2$ and divided by the area of the intertidal cross section. This yields the cross-sectionally averaged equations for the intertidal water motion. Note that the Coriolis deflection term in the intertidal momentum equation (i.e., fv) is assumed to be negligible.

a. Linear assumption of intertidal sea surface elevation

Based on the linear intertidal surface elevation (Fig. A1, blue line), the intertidal cross-sectionally averaged water level η_f is derived from the intertidal cross-sectional area A_f with intertidal water storage unchanged (i.e., two triangular areas are identical in Fig. A1):

$$A_f = \int_{B/2}^{B_t/2} (\eta + h) dy = \frac{(h_f + \eta)^2}{2[2h_f B_f - \text{sign}(y) \partial_y \eta]} \\ = B_f \frac{(h_f + \eta_f)^2}{4h_f}, \quad \text{at } (x, y) \in \partial_F \Omega. \quad (\text{A1})$$

Taking the square root of Eq. (A1) yields η_f as a function of η at $\partial_F \Omega$ [Eq. (9)].

b. Intertidal continuity equation

The depth-integrated continuity equation reads

$$\int_{-h}^{\eta} \nabla \cdot \mathbf{U} dz = \nabla \cdot \int_{-h}^{\eta} \mathbf{u}_h dz + \overbrace{w|_{z=\eta} - \nabla \eta \cdot \mathbf{u}_h|_{z=\eta}}^{=0} \\ \times \overbrace{-w|_{z=-h} - \nabla h \cdot \mathbf{u}_h|_{z=-h}}^{=0}, \\ = \frac{\partial}{\partial x} \int_{-h}^{\eta} u dz + \frac{\partial}{\partial y} \int_{-h}^{\eta} v dz + \frac{\partial \eta}{\partial t} = 0. \quad (\text{A2})$$

Then, the intertidal cross-sectional integral of the continuity equation is derived as

$$\int_{B/2}^{B_t/2} \int_{-h}^{\eta} \nabla \cdot \mathbf{U} dz dy \\ = \frac{\partial(u_f A_f)}{\partial x} + \overbrace{\frac{\partial}{\partial x} \left(-\frac{B_t}{2} \right) \int_{-h}^{\eta} u dz \Big|_{y=B_t/2} + \int_{-h}^{\eta} v dz \Big|_{y=B_t/2}}^{=0} \\ + \overbrace{\frac{d}{dx} \left(\frac{B}{2} \right) \int_{-h}^{\eta} u dz \Big|_{y=B/2} - \int_{-h}^{\eta} v dz \Big|_{y=B/2}}^{=-\alpha F_n} + \int_{B/2}^{B_t/2} \frac{\partial \eta}{\partial t} dy, \\ = \frac{\partial(u_f A_f)}{\partial x} - \alpha F_n + \frac{\partial A_f}{\partial t} = 0. \quad (\text{A3})$$

with the intertidal cross-sectionally averaged velocity

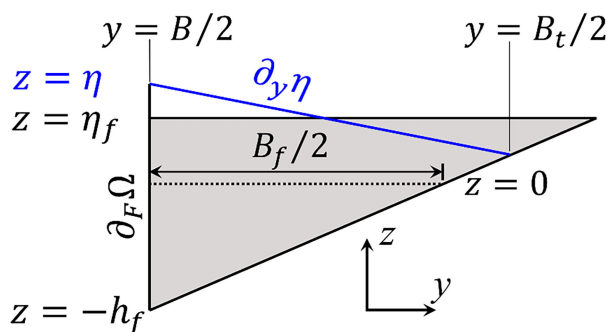


FIG. A1. Sketch of the intertidal cross section with the linearly varying intertidal surface elevation (blue line) and uniform cross-sectionally averaged water level (black horizontal line).

$$u_f = \frac{1}{A_f} \int_{B/2}^{B_t/2} \int_{-h}^{\eta} u dz dy. \quad (\text{A4})$$

Here, the lateral water transport F_n across the interface $\partial_F \Omega$ reads

$$F_n = \int_{-h}^{\eta} \mathbf{u}_h \cdot \mathbf{n}_h dz, \quad \text{with } \mathbf{n}_h = \frac{1}{\alpha} \left[-\frac{1}{2} \frac{dB}{dx}, \text{sign}(y) \right] \\ \text{at } (x, y) \in \partial_F \Omega, \quad (\text{A5})$$

and the term α is associated with the estuary width convergence

$$\alpha = \sqrt{1 + \frac{1}{4} \left(\frac{dB}{dx} \right)^2}. \quad (\text{A6})$$

The depth-integrated flux at the time-varying shoreline $y = \pm B_t/2$ is equal to zero due to zero total water depth here. Substituting Eqs. (A1) and (A4) into Eq. (A3) yields the one-dimensional intertidal continuity equation as shown in Eq. (10).

c. Intertidal momentum equation

In this section, the different terms in the momentum equation [Eq. (2)] integrated over the intertidal cross section are derived.

The depth-integrated inertia term in Eq. (2) reads

$$\int_{-h}^{\eta} \left[\frac{\partial u}{\partial t} + \nabla \cdot (u \mathbf{U}) \right] dz = \frac{\partial}{\partial t} \int_{-h}^{\eta} u dz + \nabla \cdot \int_{-h}^{\eta} u \mathbf{u}_h dz \\ + \overbrace{u \left(w - \nabla \eta \cdot \mathbf{u}_h - \frac{\partial \eta}{\partial t} \right) \Big|_{z=\eta}}^{=0} - \overbrace{u(w + \nabla h \cdot \mathbf{u}_h) \Big|_{z=-h}}^{=0}, \\ = \frac{\partial}{\partial t} \int_{-h}^{\eta} u dz + \frac{\partial}{\partial x} \int_{-h}^{\eta} uu dz + \frac{\partial}{\partial y} \int_{-h}^{\eta} uv dz. \quad (\text{A7})$$

The intertidal cross-sectional integral of the inertia term becomes

$$\begin{aligned}
\int_{B/2}^{B/2} \int_{-h}^{\eta} \left[\frac{\partial u}{\partial t} + \nabla \cdot (u\mathbf{U}) \right] dz dy &= \frac{\partial(u_f A_f)}{\partial t} + \frac{\partial(u_f u_f A_f)}{\partial x} \\
&+ \underbrace{\frac{\partial}{\partial x} \left(-\frac{B_t}{2} \int_{-h}^{\eta} uu dz \right) \Big|_{y=\frac{B_t}{2}} + \int_{-h}^{\eta} uv dz \Big|_{y=\frac{B_t}{2}}}_{=0} \\
&+ \underbrace{\frac{d}{dx} \left(\frac{B}{2} \int_{-h}^{\eta} uu dz \right) \Big|_{y=\frac{B}{2}} - \int_{-h}^{\eta} uv dz \Big|_{y=\frac{B}{2}}}_{=-\alpha M_n}, \\
&\underbrace{= \alpha u_f F_n}_{= \alpha u_f F_n} \\
&= u_f \frac{\partial A_f}{\partial t} + u_f \frac{\partial(u_f A_f)}{\partial x} + A_f \frac{\partial u_f}{\partial t} + u_f A_f \frac{\partial u_f}{\partial x} - \alpha M_n,
\end{aligned} \tag{A8}$$

with the cross-sectional integral of $(u - u_f)(u - u_f)$ induced by the cross-sectional variation of current velocities over intertidal habitats assumed to be minor and hence neglected (Speer 1984). Here, the lateral momentum transport M_n across the interface $\partial_F \Omega$ reads

$$M_n = \int_{-h}^{\eta} (\mathbf{u}_h \cdot \mathbf{n}_h) u dz, \quad \text{at } (x, y) \in \partial_F \Omega. \tag{A9}$$

Applying the dynamic boundary conditions [Eqs. (7) and (8)], the depth-integrated vertical shear stress is derived as

$$\int_{-h}^{\eta} \frac{\partial}{\partial z} \left(A_v \frac{\partial u}{\partial z} \right) dz = -su|_{z=-h}. \tag{A10}$$

The intertidal cross-sectional integral of the vertical mixing term becomes

$$\begin{aligned}
\int_{B/2}^{B/2} \int_{-h}^{\eta} \frac{\partial}{\partial z} \left(A_v \frac{\partial u}{\partial z} \right) dz dy &= \int_{B/2}^{B/2} (-su|_{z=-h}) dy, \\
&= -\frac{B_t - B}{2} su|_{z=-h} = -B_f \frac{h_f + \eta_f}{2h_f} s_f u_f,
\end{aligned} \tag{A11}$$

with the overbar $\bar{\cdot}$ means the intertidal width average, hence $s_f = \overline{su}|_{z=-h}/u_f$ measuring the average strength of bottom friction over intertidal habitats. Also, the intertidal cross-sectional integral of the barotropic term reads

$$\int_{B/2}^{B/2} \int_{-h}^{\eta} \left(-g \frac{\partial \eta}{\partial x} \right) dz dy = -A_f g \frac{\partial \eta_f}{\partial x}, \tag{A12}$$

with the cross-sectional integral of $[\partial(\eta - \eta_f)]/\partial x$ induced by the correlations between the lateral structures of the longitudinal surface gradient and the total water depth over intertidal habitats assumed to be negligible (Speer 1984).

The intertidal cross-sectional integral of the baroclinic term is derived by assuming the longitudinal density gradient to be cross-sectionally uniform:

$$\begin{aligned}
\int_{B/2}^{B/2} \int_{-h}^{\eta} \left(-\frac{g}{\rho_0} \int_z^{\eta} \frac{\partial \rho}{\partial x} dz \right) dz dy &= -\frac{g}{\rho_0} \frac{\partial \rho_f}{\partial x} \int_{B/2}^{B/2} \int_{-h}^{\eta} (\eta - z) dz dy \\
&= -A_f \frac{h_f + \eta_f}{3} \frac{g}{\rho_0} \frac{\partial \rho_f}{\partial x},
\end{aligned} \tag{A13}$$

with $\partial_x \rho_f$ as the intertidal cross-sectionally averaged density gradient. Finally, dividing the above-derived cross-sectionally integrated terms in the momentum equation by A_f yields the one-dimensional intertidal momentum equation [Eq. (11)].

APPENDIX B

Scaling Analysis

A perturbation method is utilized to solve the channel water motion equations coupled with intertidal water motion equations, scaling physical variables with their typical scales:

$$\tilde{t} = \sigma t, (\tilde{x}, \tilde{y}, \tilde{B}_f) = (x, y, B_f)/L, (\tilde{u}, \tilde{v}, \tilde{u}_f) = (u, v, u_f)/U,$$

$$(\tilde{\eta}, \tilde{\eta}_f) = (\eta, \eta_f)/a_{M_2}^m, (\tilde{z}, \tilde{h}, \tilde{h}_f) = (z, h, h_f)/H,$$

$$\partial_{\tilde{x}} \tilde{\rho}_f = \partial_x \rho_f / \rho_H. \tag{B1}$$

Here, the nondimensional variables are indicated by tilde (\sim), with $U = \epsilon \sigma L$ as the typical longitudinal tidal velocity, ϵ as the ratio of the mean M_2 tidal amplitude $a_{M_2}^m$ to the mean water depth H at the seaward boundary, L as the estuary length, and ρ_H as the typical longitudinal density gradient [see details in Kumar et al. (2016, 2017)]. The dimensionless form of the channel water motion equations is the same as those derived by Kumar et al. (2016), while the new scaled boundary condition at the interface $\partial_F \Omega$ and the intertidal water motion equations are derived below.

a. Intertidal water motion equations

The dimensionless intertidal water motion equations [Eqs. (10) and (11)] reads

$$\frac{\partial}{\partial \tilde{x}} \left[\tilde{u}_f \frac{\tilde{h}_f \tilde{B}_f (1 + \epsilon \tilde{\eta}_f / \tilde{h}_f)^2}{4} \right] + \frac{\tilde{B}_f (1 + \epsilon \tilde{\eta}_f / \tilde{h}_f)}{2} \frac{\partial \tilde{\eta}_f}{\partial \tilde{t}} - \alpha \tilde{F}_n = 0, \tag{B2}$$

$$\begin{aligned}
\frac{\partial \tilde{u}_f}{\partial \tilde{t}} + \epsilon \tilde{u}_f \frac{\partial \tilde{u}_f}{\partial \tilde{x}} - 4\epsilon \alpha \frac{\tilde{M}_n - \tilde{u}_f \tilde{F}_n}{\tilde{B}_f \tilde{h}_f (1 + \epsilon \tilde{\eta}_f / \tilde{h}_f)^2} \\
= -\frac{gH}{\sigma^2 L^2} \frac{\partial \tilde{\eta}_f}{\partial \tilde{x}} - \frac{gH \rho_H}{\rho_0 \sigma U} \frac{\tilde{h}_f + \epsilon \tilde{\eta}_f \partial \tilde{\rho}_f}{3 \partial \tilde{x}} - \frac{2s_f}{H \sigma} \frac{\tilde{u}_f}{(\tilde{h}_f + \epsilon \tilde{\eta}_f)},
\end{aligned} \tag{B3}$$

with the dimensionless lateral water and momentum exchange across the interface $\partial_F \Omega$:

$$\tilde{F}_n = \frac{F_n}{UH} = \int_{-\tilde{h}}^{\epsilon\tilde{\eta}} \tilde{\mathbf{u}}_h \cdot \mathbf{n}_h d\tilde{z} = \int_{-\tilde{h}}^0 \tilde{\mathbf{u}}_h \cdot \mathbf{n}_h d\tilde{z} + \epsilon\tilde{\eta}\tilde{\mathbf{u}}_h|_{\tilde{z}=0} \cdot \mathbf{n}_h, \quad (\text{B4})$$

$$\tilde{M}_n = \frac{M_n}{U^2H} = \int_{-\tilde{h}}^{\epsilon\tilde{\eta}} \tilde{u}\tilde{\mathbf{u}}_h \cdot \mathbf{n}_h d\tilde{z} = \int_{-\tilde{h}}^0 \tilde{u}\tilde{\mathbf{u}}_h \cdot \mathbf{n}_h d\tilde{z} + \epsilon\tilde{\eta}\tilde{u}\tilde{\mathbf{u}}_h|_{\tilde{z}=0} \cdot \mathbf{n}_h. \quad (\text{B5})$$

Following Kumar et al. (2016), the barotropic term gH/σ^2L^2 and the friction term $2s_f/H\sigma$ are at $O(1)$, while the baroclinic term $gH\rho_H/\rho_0\sigma U$ is at $O(\epsilon)$. The term α associated with the estuary width convergence is considered as $O(1)$. The nonlinear term $1/(\tilde{h}_f + \epsilon\tilde{\eta}_f)$ in the intertidal water motion equations is expanded asymptotically in $\tilde{\eta}_f/\tilde{h}_f$:

$$\frac{1}{\tilde{h}_f + \epsilon\tilde{\eta}_f} = \frac{1}{\tilde{h}_f} - \epsilon\frac{\tilde{\eta}_f}{\tilde{h}_f^2} + O(\epsilon^2). \quad (\text{B6})$$

Combining Eqs. (B2)–(B6) with the asymptotical expansion of physical variables Eq. (15), the intertidal water motion equations at each order of ϵ are derived [Eqs. (19) and (24)].

b. Linear assumption of intertidal sea surface elevation

Assuming the slope of the intertidal habitat ($2h_f/B_f \sim 10^{-3}$) much larger than the lateral gradient of the surface elevation $\partial_y\eta$ ($\sim 10^{-5}$), the square root term in Eq. (9) can be asymptotically expanded in $\partial_y\eta/(2h_f/B_f)$ ($\ll 1$):

$$\eta_f \approx \eta + \text{sign}(y) \frac{h_f + \eta \partial \eta}{4h_f/B_f \partial y} + \frac{3h_f}{8(2h_f/B_f)^2} \left(\frac{\partial \eta}{\partial y} \right)^2, \quad (\text{B7})$$

with second and higher orders neglected. The last two terms on the right-hand side show that the relationship between the intertidal surface elevation η_f and the channel surface elevation η strongly depends on the intertidal habitat width and the water depth at the side boundary $\partial_f\Omega$. The dimensionless form of Eq. (B7) reads

$$\tilde{\eta}_f = \tilde{\eta} + \text{sign}(\tilde{y}) \frac{\tilde{h}_f + \tilde{\eta} \epsilon \partial \tilde{\eta}}{4\tilde{h}_f/\tilde{B}_f \partial \tilde{y}} + \frac{3\tilde{h}_f}{8} \left(\frac{\partial \tilde{\eta}}{\partial \tilde{y}} \right)^2 \epsilon. \quad (\text{B8})$$

By combining Eqs. (15) and (B8), the leading-order and first-order forms of the linear assumption can be derived, respectively:

$$\eta_{f_{M_2}} = \eta_{M_2} + \text{sign}(y) \frac{B_f \partial \eta_{M_2}}{4 \partial y}, \quad (\text{B9})$$

$$\eta_{f_{M_j}} = \eta_{M_j} + \text{sign}(y) \frac{B_f \partial \eta_{M_j}}{4 \partial y} + \underbrace{\delta_{M_j}}_{\text{TF}}. \quad (\text{B10})$$

Here, δ_{M_j} is the modification of the intertidal surface elevation generated by the nonlinear effect of the leading-order water motion (contributing to the TF process, i.e., nonlinear intertidal interactions):

$$\delta_{M_j} = \text{sign}(y) \frac{\eta_{M_2}}{4h_f/B_f} \frac{\partial \eta_{M_2}}{\partial y} + \frac{3h_f}{8(2h_f/B_f)^2} \frac{\partial \eta_{M_2}}{\partial y} \frac{\partial \eta_{M_2}}{\partial y}. \quad (\text{B11})$$

c. Intertidal boundary conditions

The dimensionless seaward boundary condition in the intertidal region [Eq. (13)] reads

$$\tilde{\eta}_f = \frac{a_{M_2}^f}{a_{M_2}^m} \cos(\tilde{t}) + \frac{a_{M_4}^f}{a_{M_2}^m} \cos(2\tilde{t} - \varphi^f) + \frac{a_{M_0}^f}{a_{M_2}^m}. \quad (\text{B12})$$

The landward boundary condition [Eq. (14)] reads

$$\tilde{u}_f = \frac{R_i^f}{U}. \quad (\text{B13})$$

Here, $a_{M_2}^f/a_{M_2}^m$ is assumed to be at $O(1)$, and $a_{M_4}^f/a_{M_2}^m$, $a_{M_0}^f/a_{M_2}^m$, and R_i^f/U are considered to be at $O(\epsilon)$ in tidally dominated estuaries considered in this study.

APPENDIX C

Finite Element Method

The finite element method is utilized to solve the elliptic equation for the water level at each order of ϵ . As a first step, the weak form of the governing equations for the water levels in the channel and intertidal regions are derived. Then, these weak formulations are discretized within the model domain.

a. Leading-order water motion

The weak form of the leading-order M_2 water motion equation is derived by multiplying Eq. (38) with a test function V , integrating it over the channel model domain Ω , and applying the corresponding boundary conditions [Eq. (39)] and integration by parts. It yields

$$\begin{aligned} 0 &= \iint_{\Omega} [\nabla \cdot (\mathbf{D}_{M_2} \nabla \hat{\eta}_{M_2}) + i\sigma \hat{\eta}_{M_2}] V dx dy \\ &= - \iint_{\Omega} (\mathbf{D}_{M_2} \nabla \hat{\eta}_{M_2}) \cdot \nabla V dx dy + \int_{\partial_f \Omega} \hat{F}_{n_{M_2}} V ds \\ &\quad + \iint_{\Omega} i\sigma \hat{\eta}_{M_2} V dx dy, \end{aligned} \quad (\text{C1})$$

with the test function $V = 0$ at $\partial_S\Omega$. The second term on the right-hand side of the equation is induced by the nonzero lateral water exchange between intertidal and channel regions, and it is derived according to Eq. (30) and corresponding boundary conditions [Eq. (20)]:

$$\int_{\partial_f \Omega} \hat{F}_{n_{M_2}} V ds = \int_{\partial_f \Omega} \frac{i\sigma B_f}{2\alpha} \hat{\eta}_{f_{M_2}} V ds - \frac{\beta_{M_2} h_f B_f}{4\alpha} \frac{\partial \hat{\eta}_{f_{M_2}}}{\partial x} \frac{\partial V}{\partial x} ds. \quad (\text{C2})$$

Then, the channel domain is discretized using triangles as detailed in Shewchuk (1996), with N nodes in the interior or at the side/landward boundaries (unconstraint nodes) and M nodes located at the seaward boundary (constraint nodes). The one-dimensional intertidal model domain is also discretized using line segments, with N_f being the number of nodes in the interior including the landward boundary and M_f being the number of nodes at the seaward boundary. Here, M_f is

equal to 2 or 0 when the seaward limit of intertidal habitats is located at the estuary mouth or in the interior estuary. Following Kumar et al. (2016), the unknown complex amplitude of the sea surface elevation in the channel and intertidal regions is approximated by the continuous piecewise polynomials:

$$\begin{aligned} (\hat{\eta}_{M_2}, \hat{\eta}_{M_i}) &= \sum_{k=1}^P (\hat{\eta}_{M_{2k}}, \hat{\eta}_{M_{ik}}) \phi_k; \\ (\hat{\eta}_{f_{M_2}}, \hat{\eta}_{f_{M_i}}) &= \sum_{k=P+1}^{P+P_f} (\hat{\eta}_{f_{M_{2k}}}, \hat{\eta}_{f_{M_{ik}}}) \phi_k. \end{aligned} \quad (C3)$$

Here, ϕ_k indicates the Lagrange basis function, which is equal to 1 at node k and 0 at other nodes; $P = N + M$ and $P_f = N_f + M_f$ are the total nodes of the channel and intertidal model domains, respectively. Since the intertidal and channel water levels at $M + M_f$ constraint nodes are provided by the seaward boundary conditions [see Eqs. (39a) and (42a)], we have $N + N_f$ unknown variables in Eq. (C3) at each order.

By substituting Eq. (C3) into Eq. (C1) and taking $V = \phi_i$, the discretized governing equation for $\hat{\eta}_{M_2}$ is derived as

$$\begin{aligned} 0 &= - \sum_{k=1}^P \hat{\eta}_{M_{2k}} \iint_{\Omega} \mathbf{D}_{M_2} \nabla \phi_k \cdot \nabla \phi_i \, dx \, dy \\ &\quad + \sum_{k=1}^P \hat{\eta}_{M_{2k}} \iint_{\Omega} i \sigma \phi_k \phi_i \, dx \, dy \\ &\quad - \sum_{k=P+1}^{P+P_f} \hat{\eta}_{f_{M_{2k}}} \int_F \frac{\beta_{M_2} h_f B_f}{4\alpha} \frac{\partial \phi_k}{\partial x} \frac{\partial \phi_i}{\partial x} \, ds \\ &\quad + \sum_{k=P+1}^{P+P_f} \hat{\eta}_{f_{M_{2k}}} \int_{\partial_F \Omega} \frac{i \sigma B_f}{2\alpha} \phi_k \phi_i \, ds. \end{aligned} \quad (C4)$$

This yields N equations (for $i = 1, 2, \dots, N$) with $N + N_f$ unknown numbers. Hence, another N_f equations are needed to solve this system. According to the linear assumption of the intertidal water level (appendix B, section b), these equations are derived by deriving the weak form of Eq. (B9) that links $\hat{\eta}_{f_{M_2}}$ to $\hat{\eta}_{M_2}$ at the interface $\partial_F \Omega$:

$$\sum_{k=P+1}^{P+P_f} \hat{\eta}_{f_{M_{2k}}} \int_{\partial_F \Omega} \phi_k \phi_i \, ds = \sum_{k=1}^P \hat{\eta}_{M_{2k}} \int_{\partial_F \Omega} \left[\phi_k + \frac{B_f \text{sign}(y) \partial \phi_k}{4 \partial y} \right] \phi_i \, ds, \quad (C5)$$

with $i = P + 1, P + 2, \dots, P + N_f$. Therefore, the linear closed system of equations for the leading-order water motion can be solved.

b. First-order water motion

Likewise, the weak form of Eq. (40) for the first-order water motion is derived by multiplying it with the test function V , integrating it over the channel model domain Ω , and applying the corresponding boundary conditions [Eq. (42)] and integration by parts. It yields

$$\begin{aligned} 0 &= \iint_{\Omega} [\nabla \cdot (\mathbf{D}_{M_j} \nabla \hat{\eta}_{M_j} + \mathbf{F}) + i \sigma_j \hat{\eta}_{M_j} + F_{\text{TRFSD}}^{\Omega}] V \, dx \, dy \\ &= - \iint_{\Omega} (\mathbf{D}_{M_j} \nabla \hat{\eta}_{M_j} + \mathbf{F}) \cdot \nabla V \, dx \, dy \\ &\quad + \int_{\partial_F \Omega} (\hat{F}_{n_{M_j}} - F_{\text{TRFSD}}^{\partial \Omega}) V \, ds \\ &\quad + \int_{\partial_R \Omega} (R_i - F_{\text{TRFSD}}^{\partial \Omega}) V \, ds + \iint_{\Omega} i \sigma_j \hat{\eta}_{M_j} V \, dx \, dy \\ &\quad + \iint_{\Omega} F_{\text{TRFSD}}^{\Omega} V \, dx \, dy. \end{aligned} \quad (C6)$$

Here, the nonzero lateral water exchange term is derived by integrating Eq. (36) over $\partial_F \Omega$ and applying corresponding boundary conditions [Eq. (26)]:

$$\begin{aligned} \int_{\partial_F \Omega} \hat{F}_{n_{M_j}} V \, ds &= \int_{\partial_F \Omega} \left(\frac{i \sigma_j B_f}{2\alpha} \hat{\eta}_{f_{M_j}} + \frac{f_{\text{TF}}^c}{\alpha} \right) V \, ds + \frac{h_f B_f}{2} R_i^f V \\ &\quad - \int_{\partial_F \Omega} \frac{h_f B_f}{4\alpha} \left(\beta_{M_j} \frac{\partial \hat{\eta}_{f_{M_j}}}{\partial x} + f_{\text{GC}}^m + f_{\text{TF}}^m \right) \frac{\partial V}{\partial x} \, ds. \end{aligned} \quad (C7)$$

By substituting Eq. (C3) into Eq. (C6) and taking $V = \phi_i$, the discretized governing equation for $\hat{\eta}_{M_j}$ is derived as

$$\begin{aligned} &- \sum_{k=1}^P \hat{\eta}_{M_{jk}} \iint_{\Omega} \mathbf{D}_{M_j} \nabla \phi_k \cdot \nabla \phi_i \, dx \, dy + \sum_{k=1}^P \hat{\eta}_{M_{jk}} \iint_{\Omega} i \sigma_j \phi_k \phi_i \, dx \, dy - \sum_{k=P+1}^{P+P_f} \hat{\eta}_{f_{M_{jk}}} \int_{\partial_F \Omega} \frac{\beta_{M_j} h_f B_f}{4\alpha} \frac{\partial \phi_k}{\partial x} \frac{\partial \phi_i}{\partial x} \, ds \\ &\quad + \sum_{k=P+1}^{P+P_f} \hat{\eta}_{f_{M_{jk}}} \int_{\partial_F \Omega} \frac{i \sigma_j B_f}{2\alpha} \phi_k \phi_i \, ds \\ &= \underbrace{\int_{\partial_F \Omega} \frac{h_f B_f f_{\text{TF}}^m}{4\alpha} \frac{\partial \phi_i}{\partial x} \, ds}_{\text{TF}} - \underbrace{\int_{\partial_F \Omega} \frac{f_{\text{TF}}^c}{\alpha} \phi_i \, ds}_{\text{GC+AC+NS}} + \underbrace{\iint_{\Omega} \mathbf{F} \cdot \nabla \phi_i \, dx \, dy}_{\text{GC}} + \underbrace{\int_{\partial_F \Omega} \frac{h_f B_f f_{\text{GC}}^m}{4\alpha} \frac{\partial \phi_i}{\partial x} \, ds}_{\text{GC}} \underbrace{\int_{\partial_R \Omega} R_i \phi_i \, ds - \frac{h_f B_f}{2} R_i^f \phi_i}_{\text{RD}} \\ &\quad + \underbrace{\int_{\partial_F \Omega \cup \partial_R \Omega} F_{\text{TRFSD}}^{\partial \Omega} \phi_i \, ds - \iint_{\Omega} F_{\text{TRFSD}}^{\Omega} \phi_i \, dx \, dy}_{\text{TRFSD}}. \end{aligned} \quad (C8)$$

This yields N equations (for $i = 1, 2, \dots, N$) with $N + N_f$ unknown numbers. The other N_f equations are then derived from the discretized weak form of the relationship between $\hat{\eta}_{f_{M_j}}$ and $\hat{\eta}_{M_j}$ at $\partial_F \Omega$ [see Eq. (B10)]:

$$\begin{aligned} & \sum_{k=P+1}^{P+P_f} \hat{\eta}_{f_{M_j k}} \int_{\partial_F \Omega} \phi_k \phi_i ds \\ &= \sum_{k=1}^P \hat{\eta}_{M_j k} \int_{\partial_F \Omega} \left[\phi_k + \frac{B_f \text{sign}(y)}{4} \frac{\partial \phi_k}{\partial y} \right] \phi_i ds + \underbrace{\int_{\partial_F \Omega} \hat{\delta}_{M_j} \phi_i ds}_{\text{TF}}, \end{aligned} \quad (\text{C9})$$

with $i = N + 1, N + 2, \dots, N + N_f$ and $\hat{\delta}_{M_j} = \Re\{\hat{\delta}_{M_j} e^{i\sigma_j t}\}$ [see Eq. (B11)]. Therefore, the linear algebraic equations can be solved for each forcing term separately in the first-order system.

APPENDIX D

Model Comparison

a. Model validation

All parameter settings are the same in the numerical Delft3D model and the semianalytical model. However, unlike the semianalytical model that considers a linearized bed shear stress, the Delft3D model uses the quadratic friction law. To ensure consistency between the two models, the tidally averaged energy dissipation integrated over the intertidal and channel domains of the numerical model (as a function of the Chezy coefficient) is required to be the same as that in the semianalytical model (Hepkema et al. 2018; Lorentz 1926; Terra et al. 2005). This yields the Lorentz linearization condition

$$\iint_{\Omega} \left\langle \frac{g}{C^2} |u_*|^2 \right\rangle dx dy = \iint_{\Omega} \langle s u_*^2 \rangle dx dy, \quad (\text{D1})$$

$$\int_0^L \left\langle B_f \frac{g}{C_f^2} |u_f|^2 \right\rangle dx = \int_0^L \langle B_f s_f u_f^2 \rangle dx. \quad (\text{D2})$$

Here, $\langle \cdot \rangle$ denotes the tidal average; C and C_f are the Chezy coefficients in the channel and intertidal regions, respectively; and $u_* = u|_{z=-h}$ is the bottom frictional velocity in the 3D channel model domain. Based on semianalytical model results and Eqs. (D1) and (D2), the Chezy coefficients C and C_f in the numerical model are calculated. Note that only the longitudinal tidal current at the M_2 tidal frequency is considered in Eqs. (D1) and (D2) because the lateral and higher-order currents are much weaker than the leading-order longitudinal currents.

The spatial patterns of the depth-averaged currents at each tidal frequency qualitatively agree in both models, as shown in Fig. 3. The lateral and vertical distributions of the tidal current and residual circulation are also well reproduced by the extended semianalytical model in comparison with the numerical model in the presence of intertidal habitats (Fig. D1).

b. Role of changes in tidal prism

When comparing our extended semianalytical model with that of Kumar et al. (2017), the tidal prism is changed by including intertidal regions as mentioned in section 2b(1). To understand the role of tidal prism associated with the inclusion of intertidal habitats in estuaries dynamics, we investigated the differences between the two models: one with and one without intertidal habitats, while considering the same tidal prism. Since the tidal prism is enlarged by a factor of r_B due to the presence of intertidal habitats, the estuary width in the experiment without intertidal habitats is increased by a factor of r_B to maintain the same tidal prism. Other parameters are the same as those used in the default experiment with intertidal habitats (Table 2). The depth-averaged velocities obtained from the experiments with and without intertidal regions are shown in Fig. D2. The semidiurnal, quarter-diurnal, and residual currents show similar patterns between the experiments with and without intertidal habitats (see Fig. D2), when the tidal prism is kept unchanged. This implies that, in estuaries considered in this study, the intertidal areas influence the tidal and residual water motions mostly through changing the tidal prism.

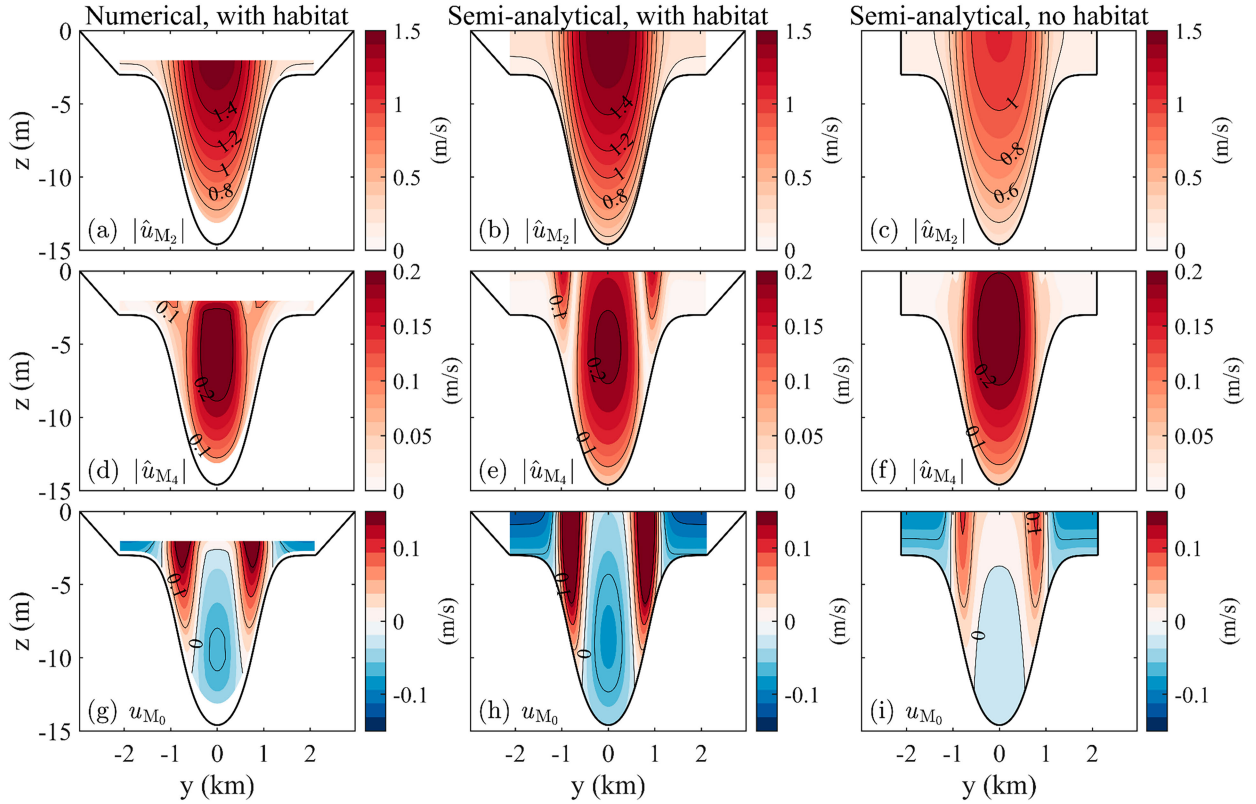


FIG. D1. Cross-sectional distribution (at $x = 5$ km) of the tidal and residual velocity obtained from (left) the numerical model with intertidal habitats, (middle) the semianalytical model with intertidal habitats, and (right) the semianalytical model without intertidal habitats at (a)–(c) M_2 , (d)–(f) M_4 , and (g)–(i) M_0 tidal frequencies, respectively. The blank spaces near the surface and bottom in the first column result from the discontinuous time series above the low tide and the inadequate resolution of the sigma-layer near the bottom.

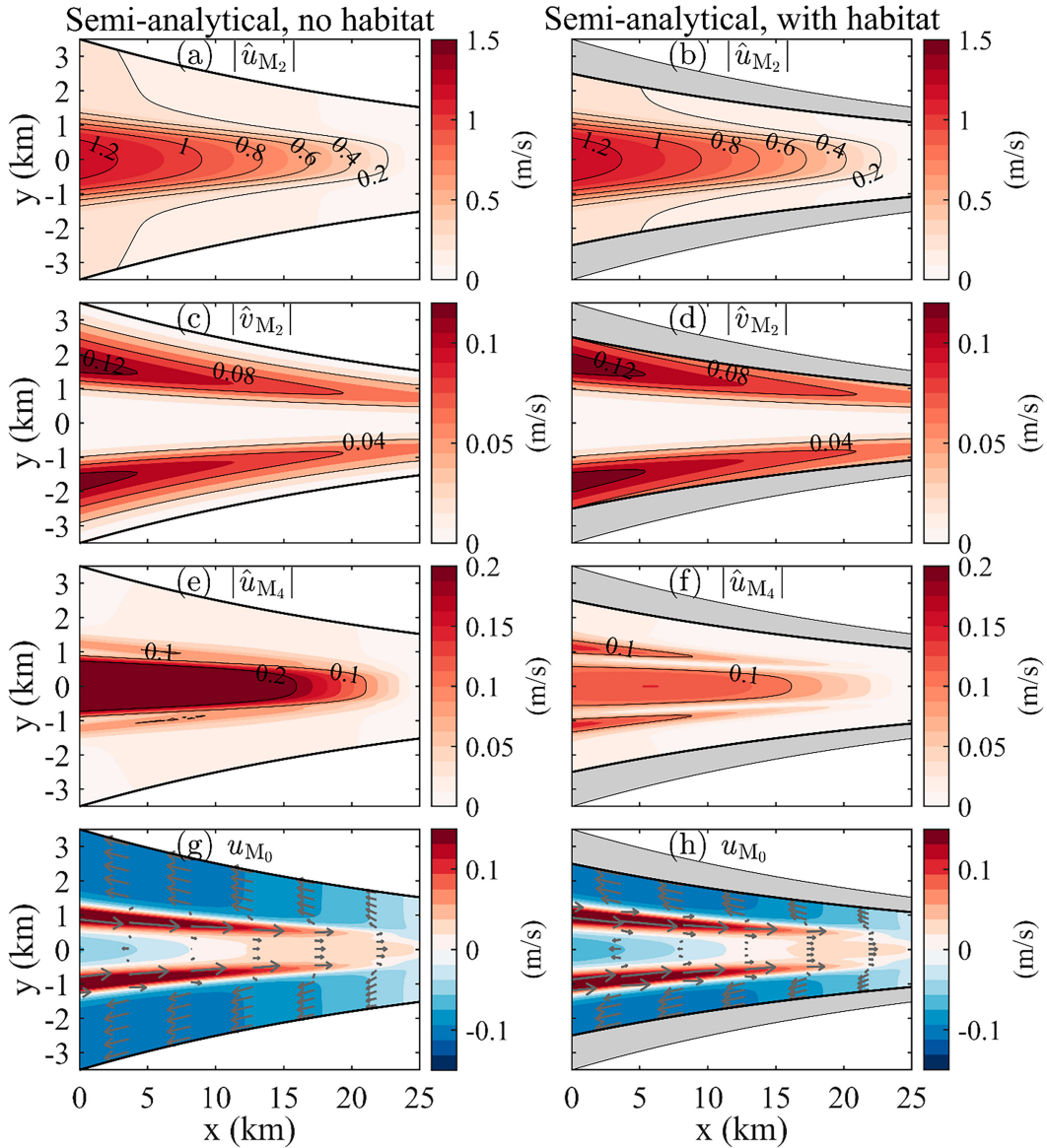


FIG. D2. Depth-averaged velocity obtained from the experiments (left) with no intertidal habitats and (right) with intertidal habitats at the (a)–(d) M₂, (e),(f) M₄, and (g),(h) M₀ tidal frequencies, considering the same tidal prism as in the default experiment. Gray areas represent the intertidal regions.

APPENDIX E

Tidal Asymmetry Decomposition

Since the M₀ and M₄ water levels and currents ($\hat{\eta}_{M_4}$, \hat{u}_{M_4} , and u_{M_0}) result from different contributions, as shown in Eqs. (45) and (46), the three skewness indicators [Eq. (52)] are also controlled by different processes at each tidal frequency:

$$\gamma_{\text{TDA}} = \alpha^{\text{TDA}} \Im \left\{ \hat{\eta}_{M_4} e^{2i\varphi_{\hat{\eta}_{M_2}}} \right\}, \quad (\text{E1})$$

$$\gamma_{\text{SWA}} = \alpha^{\text{SWA}} \Im \left\{ \hat{u}_{M_4} e^{2i\varphi_{\hat{u}_{M_2}}} \right\}, \quad (\text{E2})$$

$$\gamma_{\text{PCA}} = \alpha_{M_4}^{\text{PCA}} \Re \left\{ \hat{u}_{M_4} e^{2i\varphi_{u_{M_2}}} \right\} + \alpha_{M_0}^{\text{PCA}} u_{M_0}, \quad (\text{E3})$$

with

$$\alpha^{\text{TDA}} = \frac{\frac{3}{2} |\hat{\eta}_{M_2}|^2}{\left[\frac{1}{2} (|\hat{\eta}_{M_2}|^2 + 4|\hat{\eta}_{M_4}|^2) \right]^{3/2}}, \quad (\text{E4})$$

$$\alpha^{\text{SWA}} = \frac{\frac{3}{2} |\hat{u}_{M_2}|^2}{\left[\frac{1}{2} (|\hat{u}_{M_2}|^2 + 4|\hat{u}_{M_4}|^2) \right]^{3/2}}, \quad (\text{E5})$$

$$\alpha_{M_4}^{\text{PCA}} = \frac{\frac{3}{4}|\hat{u}_{M_2}|^2}{\left[\frac{1}{2}(|\hat{u}_{M_2}|^2 + |\hat{u}_{M_4}|^2) + (u_{M_0})^2\right]^{3/2}}, \quad (\text{E6})$$

$$\alpha_{M_0}^{\text{PCA}} = \frac{\left[\frac{3}{2}(|\hat{u}_{M_2}|^2 + |\hat{u}_{M_4}|^2) + (u_{M_0})^2\right]}{\left[\frac{1}{2}(|\hat{u}_{M_2}|^2 + |\hat{u}_{M_4}|^2) + (u_{M_0})^2\right]^{3/2}}. \quad (\text{E7})$$

Here, $|\hat{\eta}_{M_2}|$, $\varphi_{\hat{\eta}_{M_2}}$, $|\hat{\eta}_{M_4}|$, and $\varphi_{\hat{\eta}_{M_4}}$ indicate the amplitude and phase of the M_2 and M_4 tidal elevations; $|\hat{u}_{M_2}|$, $\varphi_{\hat{u}_{M_2}}$, $|\hat{u}_{M_4}|$, and $\varphi_{\hat{u}_{M_4}}$ represent the amplitude and phase of the M_2 and M_4 tidal velocities; and $\Im\{\cdot\}$ denotes the imaginary part of a complex variable. The dominant processes that control the intertidal effects on tidal asymmetry for five sensitivity experiments are shown in Fig. E1.

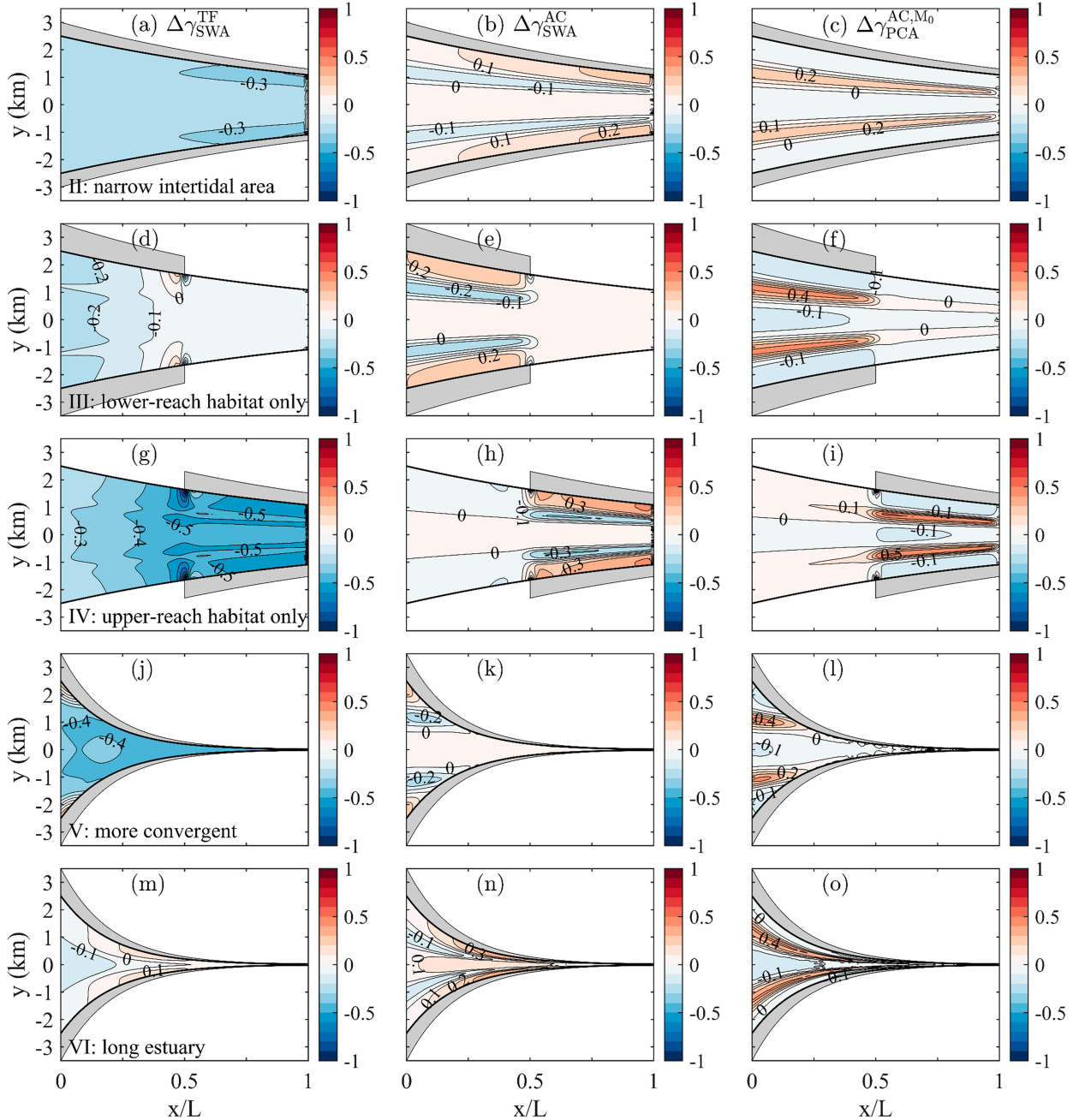


FIG. E1. Intertidal effects on γ_{SWA} due to M_4 tidal currents driven by (left) TF and (middle) AC, and on γ_{PCA} due to M_0 residual circulation driven by (right) AC, in sensitivity scenarios (first row) II, (second row) III, (third row) IV, (fourth row) V, and (fifth row) VI, respectively.

APPENDIX F

More Convergent and Long Estuary Scenarios

As the results without intertidal habitats in less convergent and short-estuary experiments (i.e., scenarios I–IV) have been already shown in Figs. 3 and 6, this section shows the no-habitat results of water level (Fig. F1) and tidal/residual currents (Fig. F2) in more convergent (scenario V) and long-estuary (scenario VI) experiments.

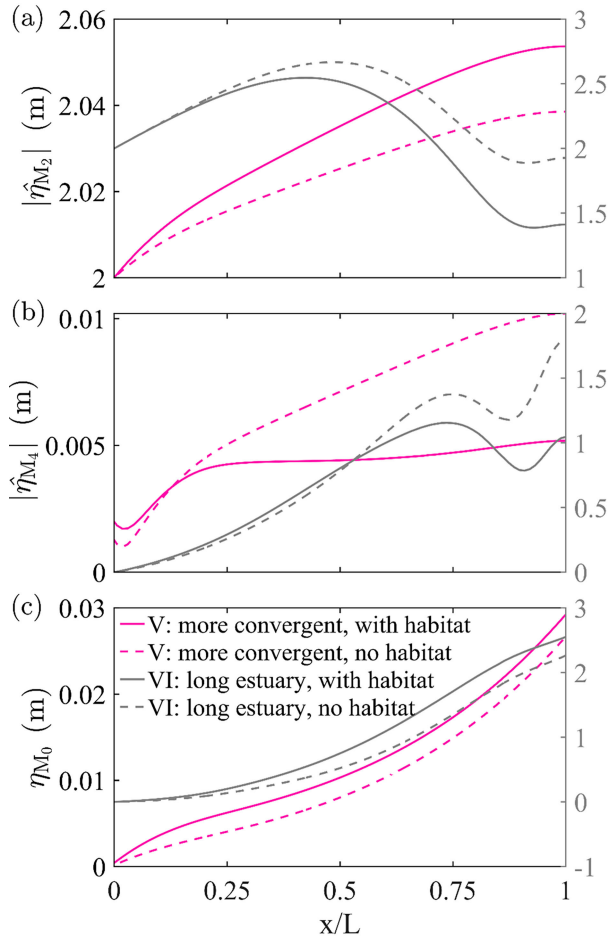


FIG. F1. The sea surface amplitude with (solid lines) and without (dashed lines) intertidal regions at the (a) M_2 , (b) M_4 , and (c) M_0 tidal frequencies in the experiment with a stronger estuary convergence (scenario V; pink lines) and experiment with a larger estuary length (scenario VI; gray lines), respectively. Note that the gray y axis on the right is utilized for the long estuary scenario only.

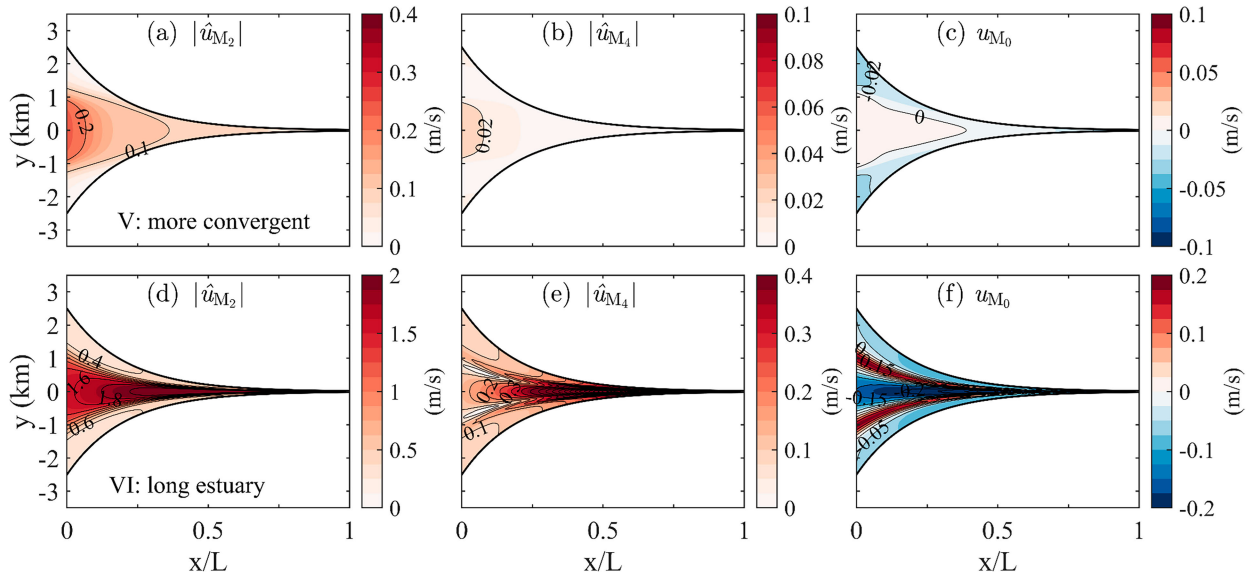


FIG. F2. The depth-averaged velocity amplitude without intertidal regions at the (left) M_2 , (middle) M_4 , and (right) M_0 tidal frequencies in (a)–(c) scenario V and (d)–(f) scenario VI, respectively.

REFERENCES

- Alembrechtse, N. C., H. E. de Swart, and H. M. Schuttelaars, 2013: Resonance characteristics of tides in branching channels. *J. Fluid Mech.*, **728**, R3, <https://doi.org/10.1017/jfm.2013.319>.
- Bom, R. A., J. A. van Gils, K. Molenaar, A. Y. Kwarteng, R. Victor, and E. O. Folmer, 2020: The intertidal mudflats of Barr Al Hikman, Sultanate of Oman, as feeding, reproduction and nursery grounds for brachyuran crabs. *Hydrobiologia*, **847**, 4295–4309, <https://doi.org/10.1007/s10750-020-04418-4>.
- Chen, S.-N., W. R. Geyer, C. R. Sherwood, and D. K. Ralston, 2010: Sediment transport and deposition on a river-dominated tidal flat: An idealized model study. *J. Geophys. Res.*, **115**, C10040, <https://doi.org/10.1029/2010JC006248>.
- Crooks, S., A. E. Sutton-Grier, T. G. Troxler, N. Herold, B. Bernal, L. Schile-Beers, and T. Wirth, 2018: Coastal wetland management as a contribution to the US National Greenhouse Gas Inventory. *Nat. Climate Change*, **8**, 1109–1112, <https://doi.org/10.1038/s41558-018-0345-0>.
- Cushman-Roisin, B., and J.-M. Beckers, 2011: *Introduction to Geophysical Fluid Dynamics: Physical and Numerical Aspects*. International Geophysics Series, Vol. 101, Academic Press, 828 pp.
- Deltares, 2021: Delft3D-flow hydro-morphodynamics user manual, Deltares, accessed 8 July 2021, <https://oss.deltares.nl/web/delft3d/>.
- de Swart, H. E., and J. T. F. Zimmerman, 2009: Morphodynamics of tidal inlet systems. *Annu. Rev. Fluid Mech.*, **41**, 203–229, <https://doi.org/10.1146/annurev.fluid.010908.165159>.
- Doody, J. P., 2004: ‘Coastal squeeze’—An historical perspective. *J. Coastal Conserv.*, **10**, 129–138, [https://doi.org/10.1652/1400-0350\(2004\)010\[0129:CSAHP2.0.CO;2](https://doi.org/10.1652/1400-0350(2004)010[0129:CSAHP2.0.CO;2).
- Dronkers, J., 1986: Tidal asymmetry and estuarine morphology. *Neth. J. Sea Res.*, **20**, 117–131, [https://doi.org/10.1016/0077-7579\(86\)90036-0](https://doi.org/10.1016/0077-7579(86)90036-0).
- , 2016: *Dynamics of Coastal Systems*. 2nd ed. World Scientific, 780 pp.
- Ensing, E., H. E. de Swart, and H. M. Schuttelaars, 2015: Sensitivity of tidal motion in well-mixed estuaries to cross-sectional shape, deepening, and sea level rise: An analytical study. *Ocean Dyn.*, **65**, 933–950, <https://doi.org/10.1007/s10236-015-0844-8>.
- Finotello, A., D. Tognin, L. Carniello, M. Ghinassi, E. Bertuzzo, and A. D’Alpaos, 2023: Hydrodynamic feedbacks of salt-marsh loss in the shallow microtidal back-barrier lagoon of Venice (Italy). *Water Resour. Res.*, **59**, e2022WR032881, <https://doi.org/10.1029/2022WR032881>.
- Fortunato, A. B., and A. Oliveira, 2005: Influence of intertidal flats on tidal asymmetry. *J. Coastal Res.*, **215**, 1062–1067, <https://doi.org/10.2112/03-0089.1>.
- Friedrichs, C. T., 2011: —Tidal flat morphodynamics: A synthesis. *Treatise on Estuarine and Coastal Science*, E. Wolanski and D. McLusky, Eds., Academic Press, 137–170.
- , and O. S. Madsen, 1992: Nonlinear diffusion of the tidal signal in frictionally dominated embayments. *J. Geophys. Res.*, **97**, 5637–5650, <https://doi.org/10.1029/92JC00354>.
- , and D. G. Aubrey, 1994: Tidal propagation in strongly convergent channels. *J. Geophys. Res.*, **99**, 3321–3336, <https://doi.org/10.1029/93JC03219>.
- Gong, W., H. Schuttelaars, and H. Zhang, 2016: Tidal asymmetry in a funnel-shaped estuary with mixed semidiurnal tides. *Ocean Dyn.*, **66**, 637–658, <https://doi.org/10.1007/s10236-016-0943-1>.
- Gu, J., M. Luo, X. Zhang, G. Christakos, S. Agusti, C. M. Duarte, and J. Wu, 2018: Losses of salt marsh in China: Trends, threats and management. *Estuarine Coastal Shelf Sci.*, **214**, 98–109, <https://doi.org/10.1016/j.ecss.2018.09.015>.
- Guo, L., M. Brand, B. F. Sanders, E. Foufoula-Georgiou, and E. D. Stein, 2018: Tidal asymmetry and residual sediment transport in a short tidal basin under sea level rise. *Adv. Water Resour.*, **121**, 1–8, <https://doi.org/10.1016/j.advwatres.2018.07.012>.
- , Z. B. Wang, I. Townend, and Q. He, 2019: Quantification of tidal asymmetry and its nonstationary variations. *J. Geophys. Res. Oceans*, **124**, 773–787, <https://doi.org/10.1029/2018JC014372>.
- , C. Zhu, F. Xu, W. Xie, M. van der Wegen, I. Townend, Z. B. Wang, and Q. He, 2022: Reclamation of tidal flats within tidal basins alters centennial morphodynamic adaptation to sea-level rise. *J. Geophys. Res. Earth Surf.*, **127**, e2021JF006556, <https://doi.org/10.1029/2021JF006556>.

- Hepkema, T. M., H. E. de Swart, A. Zagaris, and M. Duran-Matute, 2018: Sensitivity of tidal characteristics in double inlet systems to momentum dissipation on tidal flats: A perturbation analysis. *Ocean Dyn.*, **68**, 439–455, <https://doi.org/10.1007/s10236-018-1142-z>.
- Huijts, K. M. H., H. M. Schuttelaars, H. E. de Swart, and A. Valle-Levinson, 2006: Lateral entrainment of sediment in tidal estuaries: An idealized model study. *J. Geophys. Res.*, **111**, C12016, <https://doi.org/10.1029/2006JC003615>.
- Jay, D. A., 1991: Green's law revisited: Tidal long-wave propagation in channels with strong topography. *J. Geophys. Res.*, **96**, 20 585–20 598, <https://doi.org/10.1029/91JC01633>.
- Koch, M. S., E. Maltby, G. A. Oliver, and S. A. Bakker, 1992: Factors controlling denitrification rates of tidal mudflats and fringing salt marshes in south-west England. *Estuarine Coastal Shelf Sci.*, **34**, 471–485, [https://doi.org/10.1016/S0272-7714\(05\)80118-0](https://doi.org/10.1016/S0272-7714(05)80118-0).
- Kumar, M., H. M. Schuttelaars, P. C. Roos, and M. Möller, 2016: Three-dimensional semi-idealized model for tidal motion in tidal estuaries. *Ocean Dyn.*, **66**, 99–118, <https://doi.org/10.1007/s10236-015-0903-1>.
- , —, and —, 2017: Three-dimensional semi-idealized model for estuarine turbidity maxima in tidally dominated estuaries. *Ocean Modell.*, **113**, 1–21, <https://doi.org/10.1016/j.ocemod.2017.03.005>.
- Lee, J., and Coauthors, 2021: The first national scale evaluation of organic carbon stocks and sequestration rates of coastal sediments along the West Sea, South Sea, and East Sea of South Korea. *Sci. Total Environ.*, **793**, 148568, <https://doi.org/10.1016/j.scitotenv.2021.148568>.
- Lee, S. B., M. Li, and F. Zhang, 2017: Impact of sea level rise on tidal range in Chesapeake and Delaware Bays. *J. Geophys. Res. Oceans*, **122**, 3917–3938, <https://doi.org/10.1002/2016JC012597>.
- Le Hir, P., W. Roberts, O. Cazaillet, M. Christie, P. Bassoullet, and C. Bacher, 2000: Characterization of intertidal flat hydrodynamics. *Cont. Shelf Res.*, **20**, 1433–1459, [https://doi.org/10.1016/S0278-4343\(00\)00031-5](https://doi.org/10.1016/S0278-4343(00)00031-5).
- Li, C., H. M. Schuttelaars, P. C. Roos, J. H. Damveld, W. Gong, and S. J. M. H. Hulscher, 2016: Influence of retention basins on tidal dynamics in estuaries: Application to the Ems estuary. *Ocean Coastal Manage.*, **134**, 216–225, <https://doi.org/10.1016/j.ocecoaman.2016.10.010>.
- Li, L., X. H. Wang, D. Williams, H. Sidhu, and D. Song, 2012: Numerical study of the effects of mangrove areas and tidal flats on tides: A case study of Darwin Harbour, Australia. *J. Geophys. Res.*, **117**, C06011, <https://doi.org/10.1029/2011JC007494>.
- , —, F. Andutta, and D. Williams, 2014: Effects of mangroves and tidal flats on suspended-sediment dynamics: Observational and numerical study of Darwin Harbour, Australia. *J. Geophys. Res. Oceans*, **119**, 5854–5873, <https://doi.org/10.1002/2014JC009987>.
- , W. Guan, Z. He, Y. Yao, and Y. Xia, 2017: Responses of water environment to tidal flat reduction in Xiangshan Bay: Part II locally re-suspended sediment dynamics. *Estuarine Coastal Shelf Sci.*, **198**, 114–127, <https://doi.org/10.1016/j.ecss.2017.08.042>.
- , —, J. Hu, P. Cheng, and X. H. Wang, 2018a: Responses of water environment to tidal flat reduction in Xiangshan Bay: Part I hydrodynamics. *Estuarine Coastal Shelf Sci.*, **206**, 14–26, <https://doi.org/10.1016/j.ecss.2017.11.003>.
- , T. Ye, Z. He, and Y. Xia, 2018b: A numerical study on the effect of tidal flat's slope on tidal dynamics in the Xiangshan Bay, China. *Acta Oceanol. Sin.*, **37**, 29–40, <https://doi.org/10.1007/s13131-018-1263-8>.
- Liu, B., and H. E. de Swart, 2015: Impact of river discharge on phytoplankton bloom dynamics in eutrophic estuaries: A model study. *J. Mar. Syst.*, **152**, 64–74, <https://doi.org/10.1016/j.jmarsys.2015.07.007>.
- Lorentz, H. A., 1926: *Verslag Staatscommissie Zuiderzee 1918–1926*. Algemeene Landsdrukkerij, 345 pp.
- Ma, T., X. Li, J. Bai, and B. Cui, 2019: Impacts of coastal reclamation on natural wetlands in large river deltas in China. *Chin. Geogr. Sci.*, **29**, 640–651, <https://doi.org/10.1007/s11769-019-1049-8>.
- Mahavadi, T. F., R. Seiffert, J. Kelln, and P. Fröhle, 2024: Effects of sea level rise and tidal flat growth on tidal dynamics and geometry of the Elbe estuary. *Ocean Sci.*, **20**, 369–388, <https://doi.org/10.5194/os-20-369-2024>.
- Mariotti, G., and S. Fagherazzi, 2012: Channels-tidal flat sediment exchange: The channel spillover mechanism. *J. Geophys. Res.*, **117**, C03032, <https://doi.org/10.1029/2011JC007378>.
- McSweeney, J. M., R. J. Chant, and C. K. Sommerfield, 2016: Lateral variability of sediment transport in the Delaware estuary. *J. Geophys. Res. Oceans*, **121**, 725–744, <https://doi.org/10.1002/2015JC010974>.
- Möller, I., and Coauthors, 2014: Wave attenuation over coastal salt marshes under storm surge conditions. *Nat. Geosci.*, **7**, 727–731, <https://doi.org/10.1038/ngeo2251>.
- Moraes, R. P. L., B. G. Reguero, I. Mazarrasa, M. Ricker, and J. A. Juanes, 2022: Nature-based solutions in coastal and estuarine areas of Europe. *Front. Environ. Sci.*, **10**, 829526, <https://doi.org/10.3389/fenvs.2022.829526>.
- Murray, N. J., and Coauthors, 2019: The global distribution and trajectory of tidal flats. *Nature*, **565**, 222–225, <https://doi.org/10.1038/s41586-018-0805-8>.
- Nidzieko, N. J., 2010: Tidal asymmetry in estuaries with mixed semidiurnal/diurnal tides. *J. Geophys. Res.*, **115**, C08006, <https://doi.org/10.1029/2009JC005864>.
- , and D. K. Ralston, 2012: Tidal asymmetry and velocity skew over tidal flats and shallow channels within a macrotidal river delta. *J. Geophys. Res.*, **117**, C03001, <https://doi.org/10.1029/2011JC007384>.
- Nienhuis, J. H., A. D. Ashton, D. A. Edmonds, A. J. F. Hoitink, A. J. Kettner, J. C. Rowland, and T. E. Törnqvist, 2020: Global-scale human impact on delta morphology has led to net land area gain. *Nature*, **577**, 514–518, <https://doi.org/10.1038/s41586-019-1905-9>.
- Orton, P. M., and Coauthors, 2015: Channel shallowing as mitigation of coastal flooding. *J. Mar. Sci. Eng.*, **3**, 654–673, <https://doi.org/10.3390/jmse3030654>.
- Picado, A., J. M. Dias, and A. B. Fortunato, 2010: Tidal changes in estuarine systems induced by local geomorphologic modifications. *Cont. Shelf Res.*, **30**, 1854–1864, <https://doi.org/10.1016/j.csr.2010.08.012>.
- Schuerch, M., and Coauthors, 2018: Future response of global coastal wetlands to sea-level rise. *Nature*, **561**, 231–234, <https://doi.org/10.1038/s41586-018-0476-5>.
- Schuttelaars, H. M., V. N. de Jonge, and A. Chernetsky, 2013: Improving the predictive power when modelling physical effects of human interventions in estuarine systems. *Ocean Coastal Manage.*, **79**, 70–82, <https://doi.org/10.1016/j.ocecoaman.2012.05.009>.
- Shewchuk, J. R., 1996: Triangle: Engineering a 2D quality mesh generator and Delaunay triangulator. *Applied Computational Geometry Towards Geometric Engineering*, M. C. Lin and D. Manocha, Eds., Lecture Notes in Computer Science, Vol. 1148, Springer, 203–222.

- Speer, P. E., 1984: Tidal distortion in shallow estuaries. Ph.D. thesis, Massachusetts Institute of Technology and the Woods Hole Oceanographic Institution, 210 pp., <https://dspace.mit.edu/bitstream/handle/1721.1/57918/12220747-MIT.pdf;sequence=2>.
- , and D. G. Aubrey, 1985: A study of non-linear tidal propagation in shallow inlet/estuarine systems Part II: Theory. *Estuarine Coastal Shelf Sci.*, **21**, 207–224, [https://doi.org/10.1016/0272-7714\(85\)90097-6](https://doi.org/10.1016/0272-7714(85)90097-6).
- Stark, J., S. Smolders, P. Meire, and S. Temmerman, 2017: Impact of intertidal area characteristics on estuarine tidal hydrodynamics: A modelling study for the Scheldt Estuary. *Estuarine Coastal Shelf Sci.*, **198**, 138–155, <https://doi.org/10.1016/j.ecss.2017.09.004>.
- Talke, S. A., and D. A. Jay, 2020: Changing tides: The role of natural and anthropogenic factors. *Ann. Rev. Mar. Sci.*, **12**, 121–151, <https://doi.org/10.1146/annurev-marine-010419-010727>.
- , H. E. de Swart, and V. N. de Jonge, 2009: An idealized model and systematic process study of oxygen depletion in highly turbid estuaries. *Estuaries Coasts*, **32**, 602–620, <https://doi.org/10.1007/s12237-009-9171-y>.
- Tao, J., and R. Zhu, 2022: Exploring the three-dimensional flow-sediment dynamics and trapping mechanisms in a curved estuary: The role of salinity and circulation. *Front. Mar. Sci.*, **9**, 976332, <https://doi.org/10.3389/fmars.2022.976332>.
- Terra, G. M., W. J. de Berg, and L. R. M. Maas, 2005: Experimental verification of Lorentz' linearization procedure for quadratic friction. *Fluid Dyn. Res.*, **36**, 175–188, <https://doi.org/10.1016/j.fluidyn.2005.01.005>.
- Teuchies, J., and Coauthors, 2013: Estuaries as filters: The role of tidal marshes in trace metal removal. *PLOS ONE*, **8**, e70381, <https://doi.org/10.1371/journal.pone.0070381>.
- Townend, I., and P. Whitehead, 2003: A preliminary net sediment budget for the Humber estuary. *Sci. Total Environ.*, **314–316**, 755–767, [https://doi.org/10.1016/S0048-9697\(03\)00082-2](https://doi.org/10.1016/S0048-9697(03)00082-2).
- Wang, Y. P., S. Gao, J. Jia, C. E. L. Thompson, J. Gao, and Y. Yang, 2012: Sediment transport over an accretional intertidal flat with influences of reclamation, Jiangsu coast, China. *Mar. Geol.*, **291–294**, 147–161, <https://doi.org/10.1016/j.margeo.2011.01.004>.
- Wei, X., G. P. Schramkowski, and H. M. Schuttelaars, 2016: Salt dynamics in well-mixed estuaries: Importance of advection by tides. *J. Phys. Oceanogr.*, **46**, 1457–1475, <https://doi.org/10.1175/JPO-D-15-0045.1>.
- , M. Kumar, and H. M. Schuttelaars, 2017: Three-dimensional salt dynamics in well-mixed estuaries: Influence of estuarine convergence, coriolis, and bathymetry. *J. Phys. Oceanogr.*, **47**, 1843–1871, <https://doi.org/10.1175/JPO-D-16-0247.1>.
- , —, and H. M. Schuttelaars, 2018: Three-dimensional sediment dynamics in well-mixed estuaries: Importance of the internally generated overtide, spatial settling lag, and gravitational circulation. *J. Geophys. Res. Oceans*, **123**, 1062–1090, <https://doi.org/10.1002/2017JC012857>.
- , H. M. Schuttelaars, M. E. Williams, J. M. Brown, P. D. Thorne, and L. O. Amoudry, 2021: Unraveling interactions between asymmetric tidal turbulence, residual circulation, and salinity dynamics in short, periodically weakly stratified estuaries. *J. Phys. Oceanogr.*, **51**, 1395–1416, <https://doi.org/10.1175/JPO-D-20-0146.1>.
- , M. E. Williams, J. M. Brown, P. D. Thorne, and L. O. Amoudry, 2022: Salt intrusion as a function of estuary length in periodically weakly stratified estuaries. *Geophys. Res. Lett.*, **49**, e2022GL099082, <https://doi.org/10.1029/2022GL099082>.
- Winterwerp, J. C., and Z. B. Wang, 2013: Man-induced regime shifts in small estuaries—I: Theory. *Ocean Dyn.*, **63**, 1279–1292, <https://doi.org/10.1007/s10236-013-0662-9>.
- Yang, Z., and T. Wang, 2015: Responses of estuarine circulation and salinity to the loss of intertidal flats—A modeling study. *Cont. Shelf Res.*, **111**, 159–173, <https://doi.org/10.1016/j.csr.2015.08.011>.
- Zedler, J. B., 2004: Compensating for wetland losses in the United States. *Ibis*, **146**, 92–100, <https://doi.org/10.1111/j.1474-919X.2004.00333.x>.
- Zhang, Q., J. F. Tao, C. K. Zhang, W. Q. Dai, and F. Xu, 2015: Effect of the large-scale reclamation of tidal flats on the hydrodynamic characteristics in the Taizhou Bay. *Mar. Sci. Bull.*, **34**, 392–398, <https://doi.org/10.11840/j.issn.1001-6392.2015.04.005>.
- , —, and J. Yang, 2016: Numerical study on the transport timescale in a river-influenced macro-tidal estuary. *J. Coastal Res.*, **75**, 193–197, <https://doi.org/10.2112/SI75-039.1>.
- Zheng, L., C. Chen, and H. Liu, 2003: A modeling study of the Satilla River estuary, Georgia. I: Flooding-drying process and water exchange over the salt marsh-estuary-shelf complex. *Estuaries*, **26**, 651–669, <https://doi.org/10.1007/BF02711977>.
- Zhou, J., M. T. Stacey, R. C. Holleman, E. Nuss, and D. B. Senn, 2020: Numerical investigation of baroclinic channel-shoal interaction in partially stratified estuaries. *J. Geophys. Res. Oceans*, **125**, e2020JC016135, <https://doi.org/10.1029/2020JC016135>.
- Zhu, C., D. S. van Maren, L. Guo, J. Lin, Q. He, and Z. B. Wang, 2021: Effects of sediment-induced density gradients on the estuarine turbidity maximum in the Yangtze estuary. *J. Geophys. Res. Oceans*, **126**, e2020JC016927, <https://doi.org/10.1029/2020JC016927>.